Measurement of Top-Quark Mass and Inclusive Top-Quark-Pair Production Cross Section in pp Collisions at $\sqrt{s} = 7/8$ TeV with CMS

Dissertation

zur Erlangung des Doktorgrades

des Department Physik

der Universität Hamburg

vorgelegt von

Eike Steffen Schlieckau

aus Hamburg

Hamburg

2014

Gutachter der Dissertation:	Prof. Dr. Peter Schleper PD Dr. Andreas Meyer
Gutachter der Disputation:	Prof. Dr. Peter Schleper Jun.-Prof. Dr. Christian Sander
Datum der Disputation:	21.08.2014
Vorsitzender des Prüfungsausschusses:	Dr. Georg Steinbrück
Vorsitzende des Promotionsausschusses:	Prof. Dr. Daniela Pfannkuche
Leiter des Fachbereichs Physik:	Prof. Dr. Peter Hauschildt
Dekan der Fakultät für Mathematik, Informatik und Naturwissenschaften:	Prof. Dr. Heinrich Graener

Abstract

One of the most intriguing particles in the Standard Model is the top quark, the heaviest fundamental particle known to date. In this thesis, the mass of the top quark and the production cross section for top-quark pairs are measured from events with a top-quark pair decaying only into hadrons. This challenging decay mode features a high rate but is drowned by multijet background events. The top quarks are produced at the Large Hadron Collider and the decay products are detected with the Compact Muon Solenoid experiment. Data collected at centre-of-mass energies of 7 and 8 TeV with integrated luminosities of $3.54\,\mathrm{fb}^{-1}$ and $18.2\,\mathrm{fb}^{-1}$ is used for the presented measurements.

In order to improve the reconstruction and identification of the desired events, constrained least-squares fitting is utilised, which exploits the kinematics of top-quark pair events. The top-quark mass and the production cross section for top-quark pairs are extracted using likelihoods from events with at least six jets created from the hadrons in the final state. In order to reduce systematic uncertainties on the result, their main sources are incorporated into the likelihoods and are estimated in parallel with the mass itself. Combining all these methods, the most precise measurement of the top-quark mass from all-jets events so far is achieved. The top-quark mass is measured to be $172.08 \pm 0.90\,\mathrm{GeV}$.

Zusammenfassung

Eines der faszinierendsten Teilchen des Standardmodells ist das Topquark, das schwerste, heute bekannte, fundamentale Teilchen. In dieser Arbeit werden die Masse des Topquarks und der Produktionswirkungsquerschnitt für Topquarkpaare aus Ereignissen gemessen, in welchen ein Topquarkpaar nur in Hadronen zerfällt. Diese herausfordernde Zerfallsweise bietet eine hohe Rate, wird aber von Mehrjetuntergrundereignissen ertränkt. Die Topquarks werden am "Large Hadron Collider" produziert und die Zerfallsprodukte werden mit Hilfe des "Compact Muon Solenoid"-Experimentes detektiert. Daten, welche bei Schwerpunktsenergien von 7 und 8 TeV mit integrierten Luminositäten von $3.54\,\mathrm{fb}^{-1}$ und $18.2\,\mathrm{fb}^{-1}$ genommen wurden, werden für die hier präsentierten Messungen verwendet.

Zur verbesserten Rekonstruktion und Identifikation der gewünschten Ereignisse wird eine Anpassung der kleinsten, quadratischen Abweichungen unter Zwangsbedingungen verwendet, welche die Kinematik von Topquarkpaarereignissen ausnutzt. Die Topquarkmasse und der Topquarkpaarproduktionswirkungsquerschnitt werden aus Ereignissen mit mindestens sechs Jets, welche von den Hadronen erzeugt wurden, mit Hilfe von Wahrscheinlichkeitsdichten extrahiert. Zur Reduzierung der systematischen Unsicherheiten des Ergebnisses werden ihre wichtigsten Quellen in den Wahrscheinlichkeitsdichten berücksichtigt und parallel mit der Masse selbst abgeschätzt. Durch die Kombination all dieser Methoden wird die bis jetzt genaueste Messung der Topquarkmasse aus reinen Jetereignissen erreicht. Die Topquarkmasse ist mit $172.08 \pm 0.90\,\mathrm{GeV}$ gemessen.

Contents

Chapter 1

Introduction

The desire to grasp nature's deepest secrets has been calling to us since the dawn of mankind. These ambitious efforts have resulted in two independent theories embracing the current knowledge of nature. The general theory of relativity describes gravity in great detail. The latest stage in unravelling the mysteries of nature in fundamental particle physics is the Standard Model (SM) describing all the remaining interactions.

One of the elementary particles predicted by the SM is the top quark, one of the most interesting particles in current fundamental particle physics. Most of its speciality stems from its huge mass. It is the fundamental particle with the highest mass observed so far. Hence, the top quark plays a special role in the context of electroweak symmetry breaking, needed to give mass to the weak gauge bosons, and the Higgs mechanism. In addition, the mass may be constrained by the SM without any direct observation or can be used to check the consistency of the SM in combination with all other observations. Usually, top-quark pair decays are classified by the decays of the W bosons. The W boson may either decay into a charged lepton and its corresponding neutrino or into a quark and an antiquark, which both form hadrons being detected as jets. The following three different decay modes are distinguished:

- dilepton decays,
- lepton+jets decays, and
- all-jets decays.

The advantage of the dilepton decay mode is the very clean signature, however, this decay mode suffers from a comparably low rate and two neutrinos in the final state escaping detection. Thus, the full process is not reconstructable unambiguously. The lepton+jets decay mode has a higher background contribution, in turn, this gives a higher rate and only one neutrino escapes detection giving a fully reconstructable process. Finally, the all-jets decay mode features the highest rate and there is no primary neutrino in the final state escaping the detection. This brings the possibility of a better reconstruction of the full process, as all decay products are measurable in the detector, in contrast to all other decay channels. This comes at the cost of being drowned by an enormous amount of background events from multijet processes.

The mass of the top quark (m_t) has already been measured at the CERN Large Hadron Collider (LHC) [1] and the Fermilab Tevatron [2,3] in different decay modes. The two latest results from the Compact Muon Solenoid (CMS) experiment [4,5] at the LHC and the D0 experiment [6] at the Tevatron yield masses of $m_\mathrm{t} = 172.04 \pm 0.77\,\mathrm{GeV}$[1] [7] and $m_\mathrm{t} = 174.98 \pm 0.76\,\mathrm{GeV}$ [8], respectively. Both measurements were carried out in the decay channels with one charged lepton in the final state. The most precise measurement of the top-quark mass in all-jets decays at the Tevatron was carried out by the Collider Detector at Fermilab (CDF) experiment [9] and yields $m_\mathrm{t} = 175.07 \pm 1.96\,\mathrm{GeV}$ [10]. In this thesis, three different measurements are conducted and presented:

1. the top-quark pair production cross section at $\sqrt{s} = 7$ TeV,
2. the top-quark mass at $\sqrt{s} = 7$ TeV, and
3. the top-quark mass at $\sqrt{s} = 8$ TeV.

The emphasis of this thesis will be on latest, most advanced and precise measurement of the top-quark mass determined from events with all-jets decays at a centre-of-mass energy of 8 TeV, whereas the other measurements are mentioned at the end of the thesis for completeness only, with the main focus on the results and the differences with respect to the newest analysis.

In order to cope with the huge amount of background, very stringent requirements on the presence of bottom-quark induced jets are made. For a further reduction of the number of background events and an improvement of the resolution for the top-quark mass, a kinematic fit is applied making use of the characteristic signature of this final state. In the end, only well reconstructed events are used to determine the top-quark mass. In parallel, a jet energy scale factor is determined, as this is the leading systematic uncertainty in previous measurements. Both parameters are extracted from data using an ideogram method with two-dimensional probability densities.

The measurement of the top-quark mass, which is achieved within this thesis project using $3.54\,\mathrm{fb}^{-1}$ of data collected at a centre-of-mass energy of 7 TeV, results in $m_\mathrm{t} = 173.49 \pm 1.39\,\mathrm{GeV}$ and is part of the combination of eleven individual results using data from four experiments at both particle colliders yielding $m_\mathrm{t} = 173.34 \pm 0.76\,\mathrm{GeV}$ [11]. Additionally, this result is included in the latest combination of results from the CMS experiment. This combination yields $m_\mathrm{t} = 172.22 \pm 0.73\,\mathrm{GeV}$ [7] and is the most precise determination of the top-quark mass to date.

The top-quark mass result that is obtained in this thesis using $18.2\,\mathrm{fb}^{-1}$ of data collected at a centre-of-mass energy of 8 TeV features an improved reconstruction of the event kinematics and involves a more refined mass extraction compared to the measurement at 7 TeV. Both effects lead to an improved precision of the top-quark mass determination. In combination with the much larger data set collected at the higher centre-of-mass energy this gives a much improved result of $172.08 \pm 0.90\,\mathrm{GeV}$.

[1] Natural units with $c = \hbar = 1$ are used in this thesis. Therefore, energy, momentum, and mass have the dimension of energy and are expressed in electronvolts (eV). The electric charge is expressed in units of the elementary charge e.

This thesis is structured as follows: Firstly, an introduction to the SM, especially emphasising the role of the top quark, is given in chapter 2. The LHC accelerator and the CMS detector are introduced in more detail in chapter 3. An overview of the simulation tools and data sets used in this thesis is given in chapter 4. The reconstruction of high-level objects from the bare detector output is discussed in chapter 5. Then, the selection of events and extraction of the top-quark mass is detailed in chapter 6. In the chapters 7 and 8, the earlier measurements in the same decay channel of the top-quark mass and the production cross section for top-quark pairs at a centre-of-mass energy of 7 TeV are briefly presented. Finally, in chapter 9, concluding remarks and an outlook are given.

Chapter 2

Theory

There are two basic theories describing nature in the current understanding. The general theory of relativity describes gravity in great detail. The remaining three fundamental forces, being the electromagnetic, weak, and strong forces, are described by the Standard Model of particle physics (SM). It is shortly introduced in section 2.1. Following the basic principles of the SM, the most important aspects of the SM in the context of this thesis are highlighted. Thus, the emphasis will be on the top quark and its special role in the SM in section 2.2.

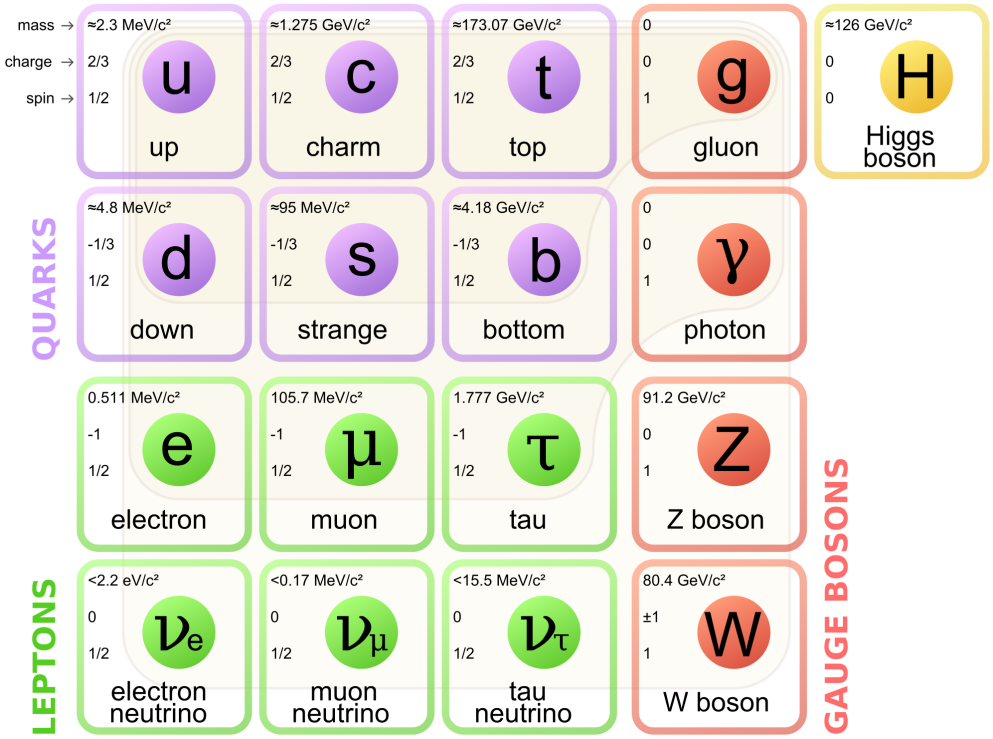

Figure 2.1: Overview of the particles from the Standard Model of particle physics. Figure taken from [12].

2.1 The Standard Model

The Standard Model of particle physics (SM) is based on the concept of indivisible elementary particles. The SM distinguishes two classes of particles:

- fermions with a spin of 1/2 making up matter and
- bosons with integral spin responsible for interactions.

An overview of all particles can be found in Figure 2.1. The fermions are grouped into three generations according to the masses. Ordinary matter is build from the first generation only. The heavier particles are usually short lived and decay into the lighter particles. A detailed review of the SM can be found in [13]. The most recent discovery in the context of the SM is the Higgs boson [14], completing it self-consistently.

2.1.1 Gauge Theory

The SM is a $U(1)_Y \times SU(2)_L \times SU(3)_C$ renormalisable, local gauge invariant theory, which can be summarised by its Lagrangian (after electroweak symmetry breaking):

$$\begin{aligned}
\mathfrak{L} = &-\tfrac{1}{4}B_{\mu\nu}B^{\mu\nu} - \tfrac{1}{4}W^a_{\mu\nu}W^{\mu\nu}_a - \tfrac{1}{4}G^b_{\mu\nu}G^{\mu\nu}_b && \text{(2.1a)}\\
&+ \bar{L}\gamma^\mu i D_\mu L + \bar{R}\gamma^\mu i D_\mu R && \text{(2.1b)}\\
&+ \left|D_\mu\phi\right|^2 - \tfrac{m_h^2}{v^2}\left(\bar{\phi}\phi - \tfrac{v^2}{2}\right)^2 && \text{(2.1c)}\\
&- \tfrac{\sqrt{2}}{v}\left(\bar{L}\phi M^f_- R + \bar{L}\phi M^f_+ R + \text{h.c.}\right) && \text{(2.1d)}
\end{aligned}$$

The kinetic energy and the self-interactions of the force fields are described by the first terms (2.1a). The second set of terms (2.1b) describes the kinetic energies of the left-handed L and right-handed R particles and their interactions with the force fields. The third and fourth set of terms describe the couplings and masses of the electroweak and Higgs bosons (2.1c) and the fermions (2.1d), respectively.

The factors $M^f_{+/-}$ shown in equation (2.2) are the four fermion mass matrices for charged and neutral leptons and for up- and down-type quarks.

$$\begin{aligned}
M^l_- &= U^{e\dagger}_L \begin{pmatrix} m_e & 0 & 0 \\ 0 & m_\mu & 0 \\ 0 & 0 & m_\tau \end{pmatrix} U^e_R, & M^l_+ &= U^{\nu\dagger}_L \begin{pmatrix} m_{\nu_e} & 0 & 0 \\ 0 & m_{\nu_\mu} & 0 \\ 0 & 0 & m_{\nu_\tau} \end{pmatrix} U^\nu_R,\\
M^q_- &= U^{d\dagger}_L \begin{pmatrix} m_d & 0 & 0 \\ 0 & m_s & 0 \\ 0 & 0 & m_b \end{pmatrix} U^d_R, & M^q_+ &= U^{u\dagger}_L \begin{pmatrix} m_u & 0 & 0 \\ 0 & m_c & 0 \\ 0 & 0 & m_t \end{pmatrix} U^u_R
\end{aligned} \qquad (2.2)$$

The U are unitary 3×3 matrices transforming between the mass and the flavour eigenstates of the fermions. They are defined via the so-called mixing matrices for quarks $V^q = U^u_L U^{d\dagger}_L$, the Cabbibo-Kobayashi-Maskawa (CKM) matrix, and leptons $V^l = U^\nu_L U^{e\dagger}_L$, the Pontecorvo-Maki-Nakagawa-Sakata (PMNS) matrix. When this definition is used for the U_L then all U_R matrices are identity matrices. Both mixing

matrices can be parametrised by four parameters, three real angles θ_{ij} and one complex phase δ being responsible for direct CP-violation in the SM. The general form of the mixing matrix is given in (2.3).

$$V = \begin{pmatrix} c_{12}c_{13} & s_{12}c_{13} & s_{13}e^{-i\delta} \\ -s_{12}c_{23} - c_{12}s_{23}s_{13}e^{i\delta} & +c_{12}c_{23} - s_{12}s_{23}s_{13}e^{i\delta} & s_{23}c_{13} \\ +s_{12}s_{23} - c_{12}c_{23}s_{13}e^{i\delta} & -c_{12}s_{23} - s_{12}c_{23}s_{13}e^{i\delta} & c_{23}c_{13} \end{pmatrix} \tag{2.3}$$

$$\text{with: } \delta^q = 0.932, \quad s^q_{12} = 0.2256, \quad s^q_{23} = 0.0415, \quad s^q_{13} = 0.035, \tag{2.4a}$$

$$\delta^l = 4.37, \quad s^l_{12} = 0.308, \quad s^l_{23} = 0.437, \quad s^l_{13} = 0.023 \tag{2.4b}$$

The abbreviations s_{ij} and c_{ij} stand for $\sin(\theta_{ij})$ and $\cos(\theta_{ij})$, respectively. The values given in (2.4a), marked with q, are the values of the CKM matrix [15], whereas in (2.4b) the value for the PMNS matrix [16] are given, marked with l. Both sets of values are best fit values from global analyses. The parameter δ^l is not yet significant.

The field tensors for the SM are defined as:

$$\begin{aligned} B_{\mu\nu} &= \partial_\mu B_\nu - \partial_\nu B_\mu \\ W^a_{\mu\nu} &= \partial_\mu W^a_\nu - \partial_\nu W^a_\mu - g_2 \epsilon_{abc} W^b_\mu W^c_\nu \\ G^a_{\mu\nu} &= \partial_\mu G^a_\nu - \partial_\nu G^a_\mu - g_s f_{abc} G^b_\mu G^c_\nu \end{aligned} \tag{2.5}$$

In the covariant gauge boson vector potentials B_μ, W^a_μ, and G^a_μ the Lorentz indices of space-time are represent by μ and ν. The a in the $W^a_{\mu\nu}$ ($G^a_{\mu\nu}$) labels the 3 (8) vector bosons of the $SU(2)_L$ ($SU(3)_C$) interaction. The coupling strength is given by g_2 (g_s) and the structure constants are denoted as ϵ_{abc} (f_{abc}) for the $SU(2)_L$ ($SU(3)_C$) interaction.

To arrive at the gauge boson mass eigenstates a rotation of the B_μ and W^a_μ fields needs to be done. The rotated fields then give the measured photon field A_μ, Z boson field Z_μ, and $W^\pm$ boson fields $W^\pm_\mu$ (2.6).

$$\begin{aligned} A_\mu &= B_\mu \cos\theta_W + W^3_\mu \sin\theta_W \\ Z_\mu &= -B_\mu \sin\theta_W + W^3_\mu \cos\theta_W \\ W^\pm_\mu &= \tfrac{1}{\sqrt{2}} \left(W^1_\mu \mp i W^2_\mu\right) \end{aligned} \tag{2.6}$$

The rotation angle θ_W is called the Weinberg angle. The value of $\sin^2\theta_W$ has been measured to be 0.23126 ± 0.00022 [15]. Using the coupling constants g_1 and g_2 of the $U(1)_Y$ and $SU(2)_L$, respectively, and the vacuum expectation value of the Higgs potential $v = 246\,\text{GeV}$ [15] the masses of the observable gauge bosons can be calculated:

$$m_A = 0, \quad m_Z = \tfrac{1}{2} v \sqrt{g_1^2 g_2^2}, \quad m_W = \tfrac{1}{2} v g_2 \tag{2.7}$$

The covariant derivative D_μ for left-handed L and right-handed particles R and the Higgs field ϕ are defined as:

$$\begin{aligned} D_\mu L &= (\partial_\mu + i g_1 \tfrac{Y}{2} B_\mu + i g_2 \tfrac{1}{2} \sigma_a W^a_\mu + i g_s c^f T_b G^b_\mu) L \\ D_\mu R &= (\partial_\mu + i g_1 \tfrac{Y}{2} B_\mu \phantom{+ i g_2 \tfrac{1}{2} \sigma_a W^a_\mu} + i g_s c^f T_b G^b_\mu) R \\ D_\mu \phi &= (\partial_\mu + i g_1 \tfrac{Y}{2} B_\mu + i g_2 \tfrac{1}{2} \sigma_a W^a_\mu) \phi \end{aligned} \tag{2.8}$$

The left-handed particles L are grouped as a doublet of Dirac spinors, whereas the right-handed particles R are singlets of Dirac spinors. All particles couple to the $U(1)_Y$ field with their hypercharge $Y = 2\,(Q - T_3)$ and the strength g_1, Q being the electromagnetic charge and T_3 being the third component of the electroweak isospin. All particles except for the right-handed ones couple to the W_μ^a fields of the $SU(2)_L$ with the strength g_2. The left- and right-handed particles couple via the strong interaction $SU(3)_C$ with the strength g_s. The factor c_f is one for quarks and vanishes for leptons. The eight generators T_b of the $SU(3)_C$ are the analogue of the Pauli matrices σ_a in the case of the $SU(2)_L$.

2.1.2 Local Gauge Invariance

The SM is based on the concept of local gauge invariance. As the phase of the fermion field has no physical meaning, it can be chosen arbitrarily. Thus, physics has to be invariant under a transformation of this phase which can differ in space-time.

$$\Psi(x) \to e^{i\alpha(x)}\Psi(x) \tag{2.9}$$

In the simplest case of quantum electrodynamics (QED) the needed covariant derivative looks like this:

$$D_\mu = \partial_\mu - ieA_\mu \quad \text{with} \quad A_\mu \to A_\mu + \tfrac{1}{e}\partial_\mu\alpha(x) \tag{2.10}$$

with ∂_μ being the plain derivative and with the vector field A_μ resembling the photon. As a mass term for the vector field is not invariant under a local gauge transformation, the field has to be massless.

The theory of the strong interaction, quantum chromodynamics (QCD), has eight generators T_a of the $SU(3)_C$ group and thus eight group parameters $\alpha^a(x)$ for the local phase transformation.

$$q(x) \to e^{i\alpha^a(x)T_a}q(x) \tag{2.11}$$

The covariant derivative D_μ and the eight gauge fields G_μ^a, resembling the gluons, with the transformation look like this:

$$D_\mu = \partial_\mu + ig_sT_aG_\mu^a \quad \text{with} \quad G_\mu^a \to G_\mu^a - \tfrac{1}{g_s}\partial_\mu\alpha^a(x) - f_{abc}\alpha^b(x)G_\mu^c \tag{2.12}$$

Here, it can be seen that gauge boson self-interaction is needed to achieve local gauge invariance. Similarly to QED, it is not possible to add a mass term for the vector field as this is not invariant under a local gauge transformation. The local gauge transformation for the weak interaction is very similar to the one of the QCD. They differ in the generators and the structure function, but the principles are the same as for the strong interaction.

As massive gauge bosons are observed for the weak interaction, the concept of spontaneous symmetry breaking is needed. In the SM this is accomplished by the Higgs mechanism [17–19]. The vacuum expectation value of the Higgs potential is $v = 246\,\text{GeV}$ [15]. While this value is unequal to zero, the SM is still a gauge invariant theory and the gauge bosons of the weak interaction gain their mass from the spontaneous symmetry breaking of the electroweak vacuum. A consequence of the Higgs mechanism is the existence of a Higgs particle, which was discovered recently [14].

2.1.3 Renormalisation

Any reasonable theory of physics should only predict finite measurable quantities. The SM is a so-called renormalisable theory meaning that predicted infinities of the theory can be absorbed into quantities that are not measurable. The renormalisation of the theory leads to energy scale dependent quantities. Thus, the so-called coupling constants are not constant anymore and become running coupling constants. For the electromagnetic interaction the coupling constant can be expressed to first order by:

$$\alpha\left(Q^2\right) = \frac{\alpha\left(\mu^2\right)}{1 - \frac{\alpha\left(\mu^2\right)}{3\pi}\log\left(\frac{Q^2}{\mu^2}\right)} \tag{2.13}$$

The strength of the electromagnetic interaction at the energy scale of interest Q is given by the strength at a reference energy scale μ. This also implies that the absolute value of the strength is not given by the SM itself, only the running of the coupling. Thus, a measurement of the coupling is needed. The commonly used scale is the mass of the Z boson where the strength of the electromagnetic interaction is given by $\alpha\left(m_Z\right)^{-1} = 127.944 \pm 0.014$ [15]. Similarly, the coupling of the strong interaction α_S can be described to first order by:

$$\alpha_s\left(Q^2\right) = \frac{\alpha_s\left(\mu^2\right)}{1 + \frac{\alpha_s\left(\mu^2\right)}{12\pi}\left(33 - 2n_f\right)\log\left(\frac{Q^2}{\mu^2}\right)} \tag{2.14}$$

Compared to the case of the electromagnetic interaction, an additional parameter for the number of quark flavours n_f available at the energy scale is needed. The strong coupling strength is given by $\alpha_s\left(m_Z\right) = 0.1184 \pm 0.0007$ [15].

Similarly to this coupling strength of the interactions, any observable of the SM can be renormalised and thus obeys an energy scale dependent running. One special example is the top-quark mass, as will be outlined in section 2.2.3.

2.1.4 Successes of the Standard Model

The SM is able to describe many observations in the electroweak and strong sector to great detail. One of the most outstanding successes of the SM is the determination of the anomalous magnetic moment of the electron. Due to extremely precise measurements and theoretical calculations, the relative difference is shown to be only 9×10^{-10} [20]. One of the most recent successes of the SM is the discovery of a Higgs boson in 2012 [14], while it was predicted back in 1964 [17–19]. Similarly, another important success, especially in the context of this thesis, is the prediction of the top quark. It was predicted back in 1973 [21] but was only discovered in 1995 [22, 23]. The top quark will be discussed in more detail in section 2.2.

2.1.5 Problems of the Standard Model

Despite its great success, there are also some phenomena that can not be explained by the SM. First of all, as already mentioned in the beginning, the SM can only describe three of the four fundamental forces. At the moment, the general theory of relativity describing gravity can not be unified with the SM as a quantisation of the field of gravity leads to non-renormalisable divergences [24]. In addition, two different aspects that are observed in our universe and can not be explained within the SM are dark matter and dark energy. Dark matter is matter that does not interact electromagnetically and is able to explain multiple observations. For example, through the effect of weak gravitational lensing, it is measured that 80% of the mass of galaxy clusters is made of dark matter and only 20% consists of ordinary matter [25]. Studies of type 1a supernovae [26, 27] hint to an expanding universe. This leads to the need of dark energy [28], which usually is used to explain this effect. A very prominent result comes from the Planck satellite [29, 30] observing the cosmic microwave background. Planck measures that our universe is only made out of 5% ordinary matter that can be described by the SM. The remaining part of the universe is made out of 27% dark matter and 68% dark energy [31]. Some further problems of the SM which have a special connection to the top quark are highlighted in section 2.2.4.

2.2 The Top Quark

The top quark is the heaviest known fundamental particle with a mass of approximately 173 GeV [11]. It was observed for the first time at the Tevatron in 1995 [22, 23]. The top quark, as the particle in the SM with the largest mass, fulfils a special role. In the following the production and the decay will be described. Afterwards, the mass definition for the top quark will be investigated and its special role in the SM is outlined.

2.2.1 Production

Through QCD processes, top quarks are mainly produced together with their antiparticles. The production of single (anti)top quarks is also possible, but has a much lower rate as it is realised via the weak interaction. In both cases, the production at a hadron collider, like the LHC, may be factorised into:

- partons[1] confined by the strong interaction, described in the following, and
- the calculation using perturbation theory in the strong or weak interaction, described afterwards for the production of top-quark pairs.

As the LHC is a proton-proton collider, the constituents of the protons play an important role in the production of any particle. Due to the nature of the strong interaction, the partons are confined and can only be determined with measurements. The content of hadrons is usually characterised by the parton distribution functions (PDFs) [32]. They determine the probability density at which a parton is found within a hadron at a certain hard scattering scale Q with a longitudinal momentum fraction x. The evolution of PDFs as function of Q and x is described using the DGLAP equations [33–35]. One example for one PDF set is illustrated in Figure 2.2.

In the following, the production of top-quark pairs is described in more detail. There are two different production mechanisms for top-quark pairs. One via the fusion of two gluons and one via the annihilation of a quark and an antiquark. An energy of at least two times the top-quark mass m_t is needed for the production of a real top-quark pair. At the LHC at a centre-of-mass energy of 8 TeV, this corresponds to an energy fraction of the proton energy of $x_1 x_2 = 0.04^2$. At this value of x the gluon density is completely dominant. Hence, the production via gluon-gluon fusion is dominant due to the PDFs.

With the knowledge which particles may induce the top-quark pair production, the hard scattering process can be described by perturbation theory. The cross section can be calculated to different orders of the strong coupling constant α_S. The precision and complexity of the calculation of the cross section increase with the order of the calculation. The most precise calculation available so far is a next-to-next-to-leading order (NNLO) calculation [36]. To get to the inclusive top-quark pair ($\mathrm{t\bar{t}}$) production cross section of

$$\sigma_{\mathrm{t\bar{t}}}(m_\mathrm{t} = 172.5\,\mathrm{GeV}) = 252.89 \pm 11.47\,\mathrm{pb} \tag{2.15}$$

the NNLO calculation has to be convolved with the PDFs and integrated over all momentum fractions and summed over all available partons for the interaction.

[1] Parton refers to quarks and gluons, collectively.

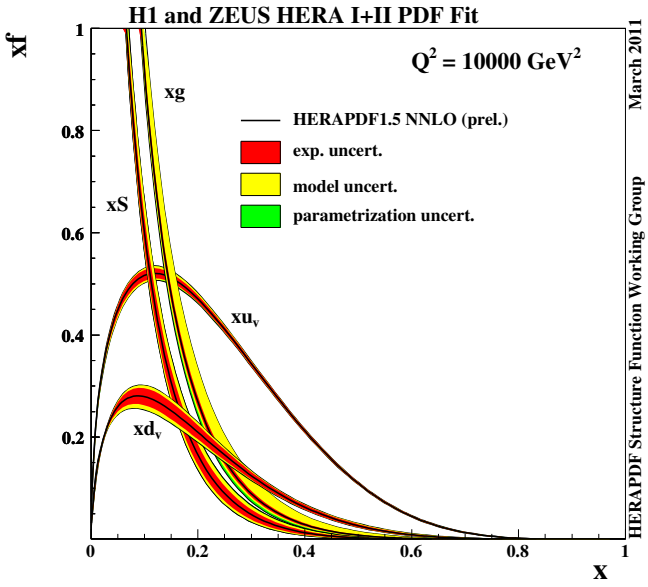

Figure 2.2: Parton distribution functions of the proton for a hard scattering scale of $Q = 100\,\text{GeV}$. The functions marked as xu_v, xd_v, xS, and xg are the probability densities for valence quarks, sea quarks, and gluons, respectively. For a usual momentum fraction transfer at the LHC gluons are dominating the proton composition. Figure taken from [32].

2.2.2 Decay

The top quark is the only particle that can decay via the weak interaction into a real W boson accompanied by a bottom quark. As this decay leads to real particles, the lifetime of the top quark is extremely short, $\tau_\text{t} \approx 5 \times 10^{-25}\,\text{s}$. This implies that the top quark decays before it is able to form a bound state as a hadron, as the hadronisation time is $\tau_\text{had} \approx 3 \times 10^{-24}\,\text{s}$. Therefore, it is possible to access the top quark as a bare quark, which, for example, makes it possible to directly evaluate the spin of the top quark.

As the CKM matrix element $|V_{tb}| \approx 1$, the top quark almost exclusively decays into a W boson and a bottom quark. Hence, the decay of a top-quark pair is characterised by the decay of the W boson. The W boson may decay into any lepton and its corresponding neutrino or into a pair of light[2] quarks. These make up nine different decay possibilities for the W boson, as there are three possible colour states for each pair of quarks. The quark then form hadrons which can be detected as jets (see section 5.3). For top-quark pairs, three main decay modes are distinguished by their experimental signature:

- All-jets decays: both W bosons decay into a pair of quarks (45.7%)
- Lepton+jets decays: one W boson decays into leptons, the other one into a pair of quarks (7.3% per lepton flavour)
- Dilepton decays: both W boson decay into leptons (1.2% per lepton combination)

[2]Here, light refers to quarks lighter than the bottom quark: up, down, charm, and strange.

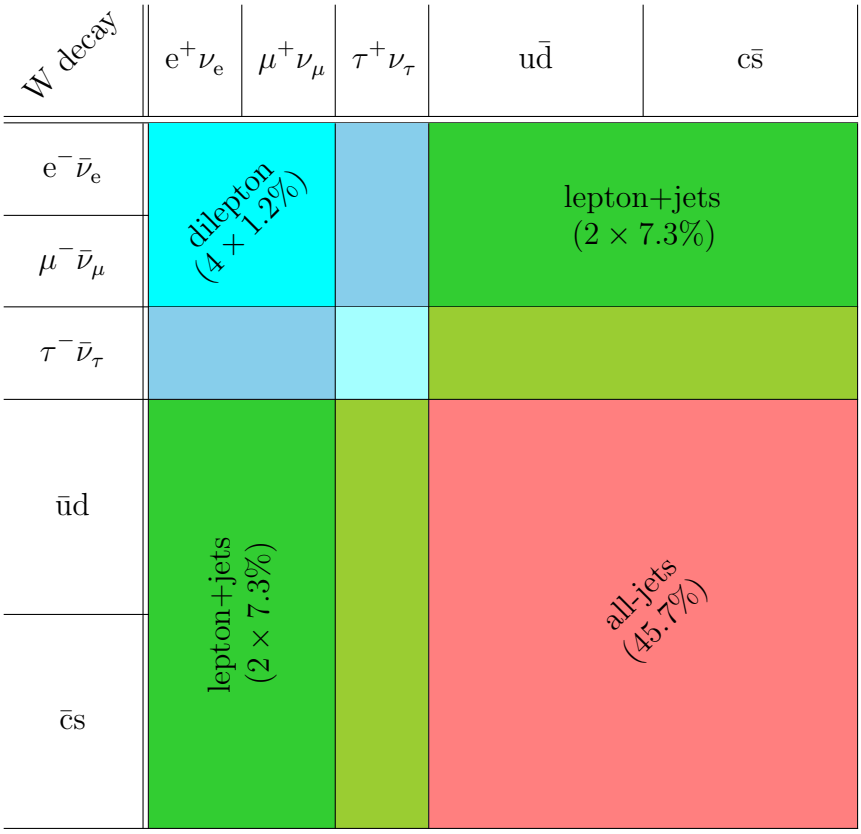

Table 2.1: Overview of the top-quark pair decay channels. On the x- and y-axis the physical decays of the W bosons are given. In the diagram the usual naming convention of the channels is given. The area of the rectangles corresponds to the branching fraction of the different channels. Usually, the decays with τ leptons are either ignored or treated separately from the dilepton or lepton+jets channels.

Usually, events with τ leptons are excluded from the lepton+jets and dilepton decays and are either treated separately or ignored completely. The described topologies are highlighted in Table 2.1. The dilepton channel has the advantage of the cleanest signature, but suffers from a comparably low rate of events. The lepton+jets channel has a higher rate, but suffers from a higher background contamination. The all-jets channel has the highest rate, but suffers from the highest background contamination by far.

2.2.3 Mass Definition

There are multiple concepts of the top-quark mass differing in several aspects. More details on the different concepts and their aspects can be found in [37]. The two most important groups of top-quark mass definitions are the theoretical well defined masses and the masses used in simulations. For all kinds of calculations within the context of the SM a well defined theoretical top-quark mass is needed. The two most important schemes are the pole mass and the $\overline{\text{MS}}$ mass, named after the renormalisation schemes.

Figure 2.3: The main Feynman diagrams for the production of a Higgs boson at the LHC (left) and radiative corrections for the Higgs-boson mass (right).

The pole mass can be interpreted as a long-distance mass, imagining taking the top quark to an infinite distance and measuring its classical mass in isolation. On the other hand, the $\overline{\text{MS}}$ mass is a short-distance mass. This has the advantage that divergences in the self-energy and the static interquark potential may cancel. Thus, the perturbative series with the $\overline{\text{MS}}$ mass converge faster than the ones with the pole mass. Both theoretical well defined masses can be extracted from the top-quark pair production cross section [38]. Unfortunately, the experimental precision of this extraction is far lower than the direct extraction of the top-quark mass from its decay products.

The top-quark mass usually measured with very high precision is the mass implemented as a parameter in an event generator. This makes it hard to directly connect this measured value with a theoretical well defined mass. Recent calculations indicate, that this parameter from an event generator is closely connected to the theoretical well defined pole mass at the order of $\sim 250 - 500\,\text{MeV}$ [39]. Thus, also these measurements with the highest possible precision reached so far can be used for theoretical interpretations.

2.2.4 Interplay

The top quark plays a key role in the SM making its study an important cornerstone in understanding the SM. The mass of the top quark is an important parameter for the electroweak symmetry breaking. For example, the mass of the top quark can be used in conjunction with the mass of the W and Higgs bosons, m_W and m_H, to check the self-consistency of the SM. The most important source is the radiative correction of the W boson mass $\Delta m_\text{W}^\text{rad}$ [40]:

$$\frac{\Delta m_\text{W}^\text{rad}}{\text{GeV}} \propto 1.7 \times 10^{-5} \left(\frac{m_\text{t}}{\text{GeV}}\right)^2 - 5.7 \times 10^{-2} \ln\left(\frac{m_\text{H}}{\text{GeV}}\right) - 9.0 \times 10^{-3} \ln^2\left(\frac{m_\text{H}}{\text{GeV}}\right) \quad (2.16)$$

This check of the self-consistency of the SM can be done, for example, with Gfitter [41,42]. This check gives a p-value for the SM to describe all measured data of 0.21.

As the coupling of the Higgs boson to fermions is proportional to the fermion mass, the top-quark mass is a crucial factor in Higgs physics being the particle with the highest mass in the SM. At the LHC, the main production mechanism for Higgs bosons is the gluon-gluon initial state followed by a top-quark triangle radiating the Higgs boson (see

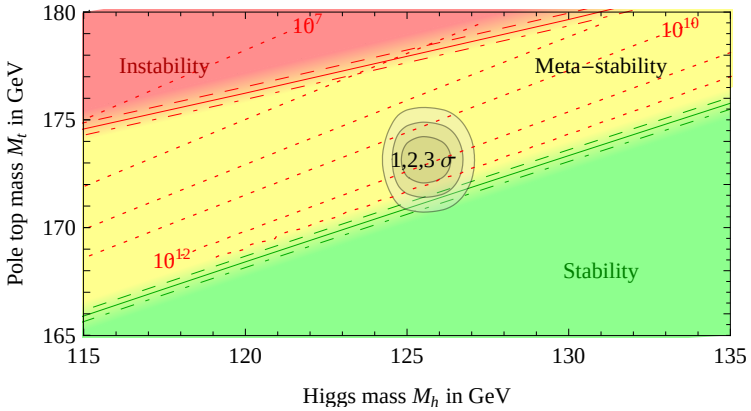

Figure 2.4: Illustration of the different stability regions of the electroweak vacuum as function of the Higgs-boson and top-quark masses. Figure taken from [44].

Figure 2.3 (left)). Similarly, one of the best measurable decays of the Higgs boson is the decay via a top-quark triangle into two photons. In addition, the top-quark mass is the most important parameter for driving the radiative corrections of the Higgs-boson mass (see Figure 2.3 (right)) [43]:

$$\Delta m_{\mathrm{H}}^2 \propto -\frac{|\lambda_f|^2}{8\pi^2}\Lambda_{\mathrm{UV}}^2 \tag{2.17}$$

They are proportional to the coupling (λ_f) of fermion f and to the scale until which the SM should be valid (Λ_{UV}). Every fermion contributes to this correction. Being the particle with the largest mass, the top quark has the strongest coupling $\lambda_t \approx 1$. Usually, the scale until the SM is valid is assumed to be the reduced Planck scale $M_{\mathrm{P}} = 2.4 \times 10^{18}\,\mathrm{GeV}$. At this point, gravity should start to play an important role. Thus, this leads to a radiative correction of the Higgs-boson mass 15 orders of magnitude larger than the mass itself. This is the so-called fine-tuning or hierarchy problem.

Another important aspect of the SM, where the top quark plays a special role, is usually summarised under the topic "stability of the universe" [44]. The stability of the electroweak vacuum is characterised by the minimum of the Higgs potential. If this minimum is global at all energies, the electroweak vacuum is stable. If the minimum is only local, but the lifetime of this local minimum, i.e. the time needed for quantum tunnelling from this local minimum to the global one, is longer than the lifetime of the universe, then this state is called meta-stable. If the lifetime of the local minimum is shorter than the lifetime of the universe the state is called unstable. The stability of the electroweak vacuum mainly depends on the masses of the Higgs boson and the top quark and is illustrated in Figure 2.4. An unstable electroweak vacuum is usually interpreted as a reason for new physics, as the existence of the universe would be a mystery or miracle in this case. Using the current measurements of the Higgs-boson and top-quark masses, a region of meta-stability is reached close to the border to the stable region. This leads to the conclusion that the SM could be a valid theory until gravity starts to play an important role close to the Planck scale.

Chapter 3

Experimental Setup

In this chapter, the two main ingredients of the experimental setup are described. Firstly, the Large Hadron Collider is described, accelerating beams of protons and bringing them to collision. Afterwards, the Compact Muon Solenoid experiment is introduced which is used for the detection of the particles produced in these collisions.

3.1 Large Hadron Collider

The Large Hadron Collider (LHC) [1] is located at the site of the European Organisation for Nuclear Research (CERN) near Geneva, Switzerland. In the LHC, two beams of protons are accelerated to an energy of up to 4 TeV. Later, the energy of the beams is supposed to be increased to the design value of 7 TeV. Each of the two beams consists of up to 2808 bunches of protons with up to 1.7×10^{11} particles per bunch. The two beams are flying in opposite directions and are collided at four points around the LHC. At these four interaction points, the four main experiments of the LHC, namely ALICE [45, 46], ATLAS [47, 48], CMS [4, 5], and LHCb [49], are located. The CMS experiment will be described in more detail in the next section.

The LHC is a superconducting synchrotron with a circumference of 27 km. The trajectory of the proton beams has to be bended on this ring. To achieve this trajectory with proton beams of an energy of up to 7 TeV, the magnets are operated at a temperature of 1.9 K, cooled by 37 million kilogrammes of superfluid helium, to achieve superconductivity for the Niobium-Titanium windings of the magnets.

Before collisions may start at the interaction points in the LHC, the protons have to undergo several steps. At the beginning, hydrogen gas is extracted from a gas bottle, the electrons are stripped off and the two atoms are split. Via a grid with constant negative charge, the protons are accelerated to the LINAC 2, which further accelerates the beam of protons to an energy of 50 MeV. Afterwards, the beams are accelerated via the BOOSTER, PS, and SPS synchrotrons and injected into the LHC with an energy of 450 GeV. In the LHC, the beams are then accelerated to the final energy of 4 TeV. An overview of the full LHC accelerator complex can be found in Figure 3.1.

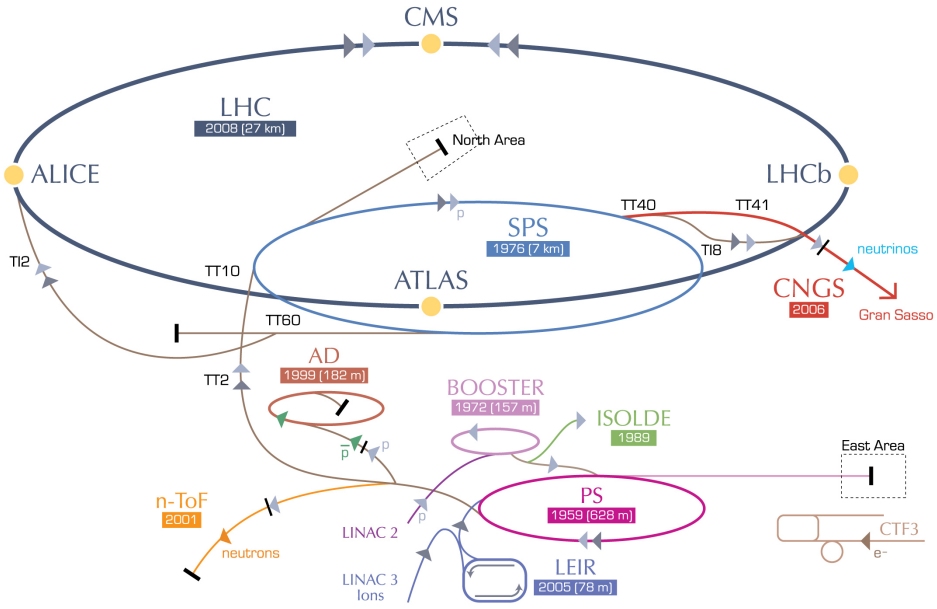

Figure 3.1: Overview of the CERN accelerator complex. Figure taken from [50].

As the LHC provides a unique performance in terms of beam and collision energy, beam intensity and event rate, several new effects appear, which did not play an important role ever before. The high beam energy requires a very strong magnetic field for the bending magnets to keep the beams on track. This leads to the fact, that the LHC is the first hadron collider where the energy loss due to synchrotron radiation of the protons plays an important role. In addition, the very high beam intensities lead to multiple proton-proton interactions per bunch crossing, so-called pileup. The experiments had to find ways to identify and account for these additional interaction. The high bunch crossing rate leads to an enormous amount of data, which the experiments must deal with by selecting the most interesting processes. An overview of the most important parameters of the LHC can be found in Table 3.1.

parameter	achieved in 2012	design value
proton energy	4 TeV	7 TeV
number of bunches	1374	2808
particles per bunch	1.7×10^{11}	1.15×10^{11}
bunch spacing	50 ns	25 ns
peak luminosity [$\mathrm{cm}^{-2}s^{-1}$]	$7.7{\times}10^{33}$	$1{\times}10^{34}$
bunch crossing rate	20 MHz	40 MHz
maximum of mean events per crossing	40	19
energy loss per turn	715 eV	6.71 keV
maximum field of bending magnets	4.76 T	8.33 T

Table 3.1: Overview of the most important parameters of the LHC comparing achieved values from 2012 with design values. Values taken from [51].

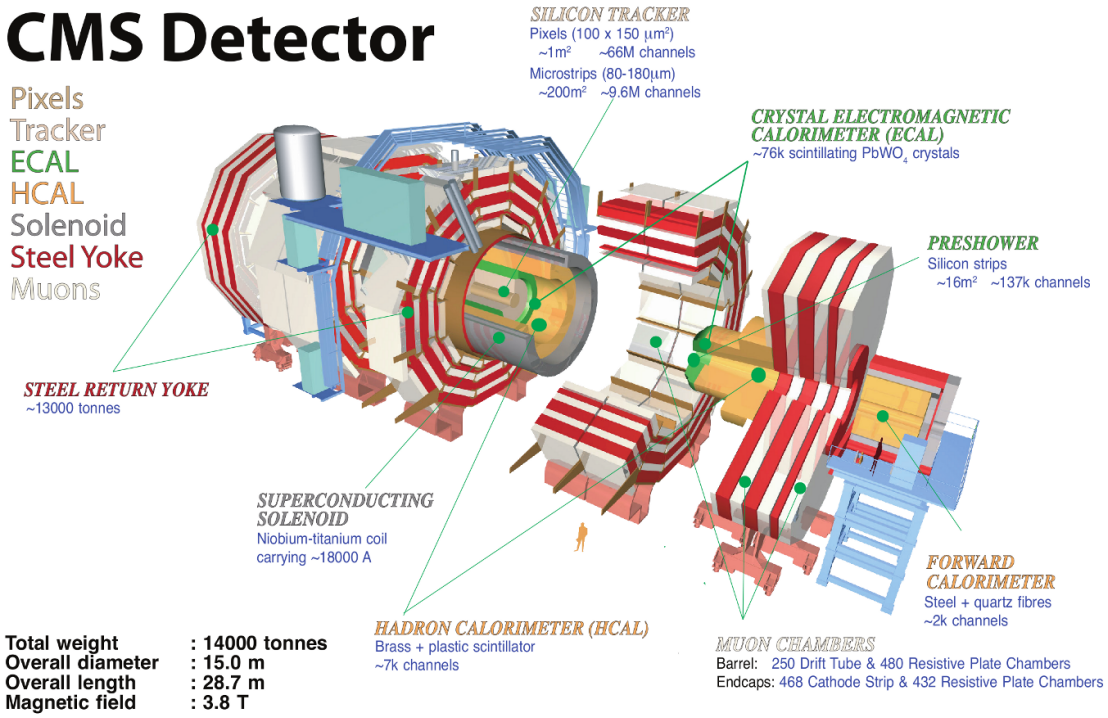

Figure 3.2: Overview of the CMS detector. Figure taken from [52].

3.2 Compact Muon Solenoid

The Compact Muon Solenoid (CMS) experiment [4, 5] is a general purpose detector at the LHC. An overview of the detector and the most important components is shown in Figure 3.2. In total, CMS weighs 14 000 t and has a length of 28.7 m and diameter of 15.0 m. The inner-most layers of CMS are the pixel sensors followed by the strip tracker, both being silicon sensors. The following two layers are the calorimeters, first the electromagnetic scintillating crystal calorimeter and second the hadronic brass-plastic sampling calorimeter. The calorimeters are succeeded by the superconducting solenoid coil magnet and the muon systems, which are crisscrossed by the steel return yoke for the magnet.

The origin of the right-handed coordinate system is the nominal interaction point. The x, y, and z axes are pointing to the centre of the LHC ring, upwards, and along the anticlockwise-beam direction, respectively. From the positive z axis, the polar angle θ and in the x-y plane the azimuthal angle ϕ are measured. The pseudorapidity is defined by $\eta = -\ln\tan(\theta/2)$. Transverse momenta p_{T} are computed from their x and y components. Transverse energies E_{T} are energies scaled by the ratio of p_{T}/p.

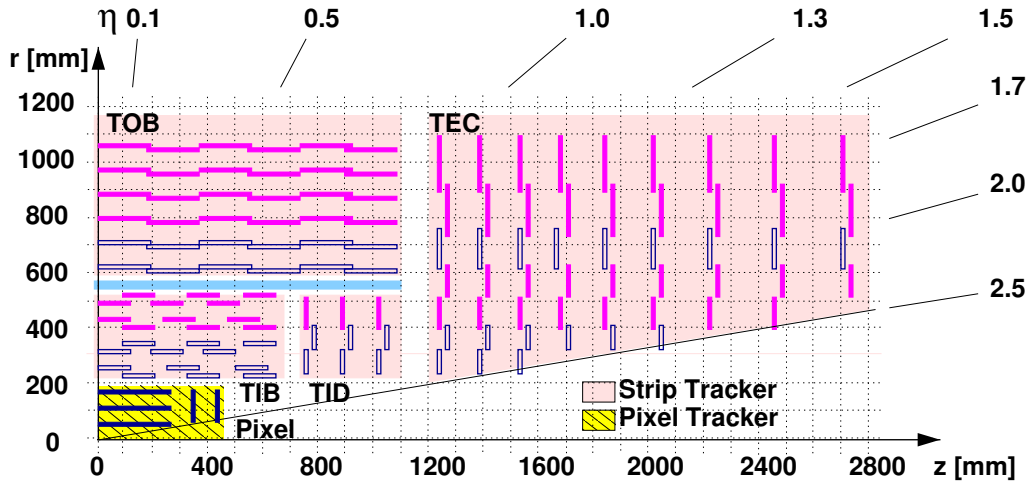

Figure 3.3: One quarter of the CMS tracker in the r-z view. The modules indicated by open (blue) lines are stereo modules. Figure taken from [53] and modified.

3.2.1 Tracking System

The pixel detector consists of three barrel layers at radii of 4.4 cm, 7.3 cm, and 10.2 cm with a length of 53 cm along z and two pairs of endcap discs reaching from a radius of 6 cm to 15 cm at $|z| = 34.5$ cm and 46.5 cm. In total, this sums up to 66 million pixels, each in size of $100 \times 150\,\mu\text{m}^2$ yielding an active area of $1\,\text{m}^2$. The resolution is about $10\,\mu$m in $r - \phi$ and about $20\,\mu$m in z.

The strip detector consists of ten barrel layers and and twelve disc layers. The barrel layers are divided into two parts, the Tracker Inner Barrel (TIB) consisting of four layers with $|z| < 65$ cm and the Tracker Outer Barrel (TOB) consisting of six layers with a length of 2.2 m. The inner two layers of both barrel parts are stereo modules, each consisting out of two layers mounted back-to-back under an angle of 100 mrad to provide a measurement of the hit position along the strip direction. Like the barrel layers, the endcaps are divided into two parts, the Tracker Endcap (TEC) with nine discs ranging from 120 cm to 280 cm in $|z|$ and the Tracker Inner Discs (TID) with three discs filling the space between TIB, TOB, and TEC. Combining all modules, the strip detector provides 9.6 million channels and covers an area of $200\,\text{m}^2$.

The tracking system is contained in a temperature controlled support tube, held by a carbon-fibre structure.

3.2.2 Calorimeter System

The electromagnetic calorimeter is a homogeneous crystal calorimeter, built from 75 848 lead tungstate ($PbWO_4$) crystals. This has the advantage of a short radiation length X_0 of 0.89 cm, a low Molière radius R_M of 2.2 cm, a fast response (80% of light emitted

within 25 ns), and radiation hardness. The barrel part (EB) is built from 61 200 crystals, covers a range from $|\eta| < 1.479$ and has a thickness of $25.8\,X_0$. The crystals are quasi-projective, meaning that they are tilted by 3° in ϕ and η with respect to the nominal interaction point. The two endcap parts (EE) are built from 7 324 crystals each, covering $1.479 < |\eta| < 3.0$ and $24.7\,X_0$ in thickness. The energy resolution σ of the electromagnetic calorimeter for an electron or photon with energy E is given by:

$$\left(\frac{\sigma}{E}\right)^2 = \left(\frac{2.83\%\sqrt{\text{MeV}}}{\sqrt{E}}\right)^2 + \left(\frac{124\,\text{MeV}}{E}\right)^2 + (0.26\%)^2 \tag{3.1}$$

The terms are describing stochastic effects in the showers, noise effects, and non-uniformities and non-linearities in the detector response, respectively.

The hadronic calorimeter is a sampling calorimeter built with brass as absorber and plastic scintillator as active material connected via wavelength-shifting fibres to the read out with photodiodes. The three main parts are the barrel (HB), endcap (HE), and forward (HF) calorimeters covering $0 < |\eta| < 1.4$, $1.3 < |\eta| < 3.0$, and $3.0 < |\eta| < 5.0$ and consisting of 2 304, 2×1 152, and 2×900 towers, respectively. The energy resolution was simulated for a particle with a transverse energy E_T^MC:

$$\frac{\sigma\left(\frac{E_\text{T}^\text{rec}}{E_\text{T}^\text{MC}}\right)}{\left\langle\frac{E_\text{T}^\text{rec}}{E_\text{T}^\text{MC}}\right\rangle} = \frac{5.6\,\text{GeV}}{E_\text{T}^\text{MC}} + \frac{1.25\sqrt{\text{GeV}}}{\sqrt{E_\text{T}^\text{MC}}} + 0.033 \tag{3.2}$$

3.2.3 Magnet System

The prerequisite of an unambiguous muon charge determination up to a momentum of 1 TeV dictates the requirements for the magnet system. At CMS, a superconducting solenoid, 12.9 m long and 5.9 m in diameter, was chosen. A current of 18 kA generates a magnetic field of 3.8 T in the superconducting coil with 2 168 windings. The Niobium-Titanium cable has a total length of 53 km and an overall conductor cross section of $64 \times 22\,\text{mm}^2$. The magnetic field stores an energy of 2 GJ and the hoop stress of the conductor is 64 atm.

3.2.4 Muon System

The muon system facilitates the identification of muons, as (almost) all charged particles passing trough the calorimeters are muons. In addition, the momentum resolution for large momenta is improved with respect to the inner tracker due to the larger lever arm. The muon system consists of drift tubes, cathode strip chambers, and resistive plate chambers covering $0 < |\eta| < 1.2$, $0.9 < |\eta| < 2.4$, and $0 < |\eta| < 1.6$, respectively.

The 70 drift tubes make up four barrel layers at radii of 4.0 m, 4.9 m, 5.9 m, and 7.0 m and have a single point precision of about 200 μm. The two inner layers of drift tubes are covered on the inside and outside with resistive plate chambers, whereas the outer two layers are equipped with only one resistive plate chamber on the inside.

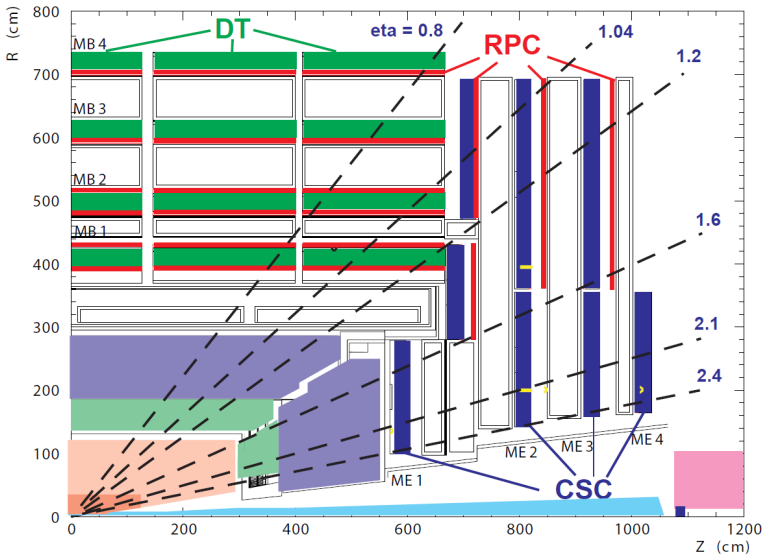

Figure 3.4: One quarter of the CMS muon system in the r-z view. The steel return yoke for the magnetic field is indicated as hollow area between the muon systems. The pixel and strip trackers, the electromagnetic and hadronic calorimeters, and the magnet system are indicated inside the muon system. Figure taken from [5].

Each endcap consists of 234 cathode strip chambers grouped in four discs, providing both a faster and more precise signal. The spacial precision is about 200 μm. The inner three layers are covered with resistive plate chambers on the outside up to $|\eta| = 1.6$.

3.2.5 Trigger System

The LHC ran with bunch crossing rates of up to 20 MHz, the maximum design value is 40 MHz. The data of only a few hundred bunch crossings may be saved per second. This necessitates an online rejection factor of several tens of thousands. The CMS trigger system does this in two steps. First, a very fast Level-1 trigger (L1T) keeps only about one out of one thousand events. Then, the High-Level trigger (HLT) reduces the rate to only a few hundred events per second.

Custom hardware processors make up the Level-1 trigger. They reconstruct very coarse, primitive objects and keep only events where these simple objects fulfil basic transverse energy or momentum thresholds. The time to take the decision of keeping or rejecting the event is 3.2 μs, which is equal to the time needed for data to be transmitted from the detector electronics to the trigger logic and back.

All events passing the Level-1 trigger are processed by the High-Level trigger, a huge processor farm. The High-Level trigger code may also contain very sophisticated algorithms for the object reconstruction and identification. The strategy is to discard an event as early as possible in order to save processing time. Thus, a partial reconstruction is done first for interesting regions marked by the Level-1 trigger. Later, additional information from calorimeters and the muon systems are used. In the end, information from the strip and pixel detectors is added. All events that pass the High-Level trigger are written to mass storage for analysis.

Chapter 4

Simulation

For this analysis, simulated samples from the "Summer12" CMS production campaign are used. The first step is the simulation of the hard scattering process. It factorises into two parts, the determination which particles can initiate the process defined by PDFs, and the matrix element generation. For the generation, the CTEQ 6.6L PDFs [54] are used. For the nominal samples of the top-quark pair production, MadGraph 5.1.5.11 [55] is used for the matrix element generation and MadSpin [56] is used for the decay of heavy resonances like the top quark or the W boson. One example Feynman diagram of this process is shown in Figure 4.1 (left) in the all-jets decay mode. Afterwards, the parton shower (fragmentation and hadronisation) is done by pythia 6.426 [57] using the Z2* tune [58]. Finally, all stable[1] particles are passed to the full detector simulation using geant4 [59]. All involved steps require the use of Monte-Carlo methods utilising pseudo-random numbers for the generation, interaction, and decay of particles. An overview of the simulated samples used from the central CMS production campaign can be found in Appendix A. The simulated samples are stored in the same format as the data taken with the detector, with the addition of supplementary information on the generation itself. One sample used for the validation of the background estimation method (see section 6.3) is privately produced. In this sample the matrix element generation and parton shower is done by pythia 6.426. One example Feynman diagram is shown in Figure 4.1 (right). The detector simulation is skipped for this sample, as this saves a lot of time and is not necessary for the validation procedure.

4.1 Matrix Element

The MadGraph matrix-element generator is a multi-leg leading-order generator, thus, it supports the radiation of additional particles with respect to pure top-quark pair final state. In the CMS production, MadGraph is configured to produce top-quark pair decays with up to three additional particles. These radiations may occur in the initial state and from the top quarks, but not from the decay products. Samples with

[1] Here, stable means the lifetime is long enough to reach the detector.

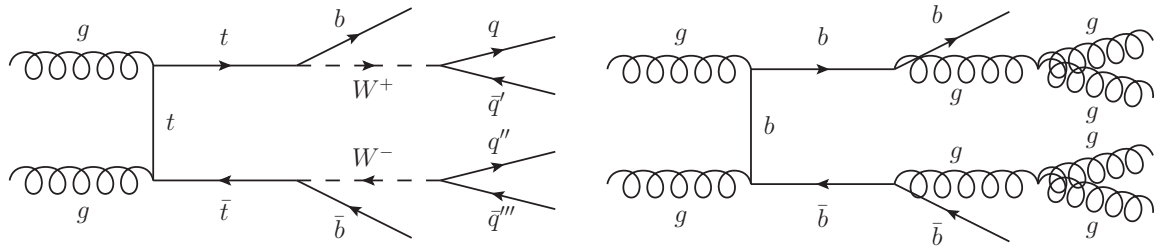

Figure 4.1: One example Feynman diagram for the production of a top-quark pair with an all-jets decay (left) and one example background process (right).

top-quark masses in the range from 166.5 GeV to 178.5 GeV were generated with a default central value of 172.5 GeV.

The two next-to-leading-order (NLO) generators POWHEG [60–63] and MC@NLO [64, 65] are used for systematic variations. They yield the advantage of having more precise NLO calculations. On the other hand, unfortunately, they do not support the radiation of additional particles except for one possible radiation. All top-quark pairs samples will be normalised such that the total event yield corresponds to the NNLO cross section $\sigma_{\mathrm{t\bar{t}}}(m_{\mathrm{t}} = 173.3\,\mathrm{GeV}) = 245.79\,\mathrm{pb}$ [36]. The nominal sample contains about 14 times the number of events expected from $18.2\,\mathrm{fb}^{-1}$, while the alternative samples for systematic variations contain about five to nine times the expected number of events.

For the background validation, PYTHIA is used for the matrix element generation featuring initial and final states with two particles at leading-order. Here, it is restricted to generate matrix elements with two gluons in the initial state producing a pair of bottom quarks. The calculation of the cross section for generic multijet final states is extremely difficult, thus no calculations are available. The cross section for the production of a bottom-quark pair in association with at least four more jets is expected about one order of magnitude above the production cross section for top-quark pairs.

4.2 Parton Showering

The PYTHIA parton shower may overcome limitation due to the order of perturbation theory used by the matrix-element generators. Thus, PYTHIA can generate soft, collinear radiation based on splitting functions in regions where the matrix-element calculation diverges. To avoid overlap between radiation calculated by the matrix-element generator and later on in the parton showering, a matching has to be done. This is done with the MLM prescription [66]. Radiated particles from partons must have transverse momenta of at least 1 GeV to avoid diverging calculations. The parton shower models the evolution of partons until $\alpha_S \approx 1$ using the DGLAP equations [33–35].

Afterwards, the non-perturbative hadronisation starts. In this part of the process, the partons are transformed into colourless hadrons. In the Lund string model used in PYTHIA, the colour potential between two partons increases linearly with the distance.

When it becomes energetically advantageous to create a $q\bar{q}$ pair from the energy within the string field, the string is broken into two separate colour singlets. This step may be repeated multiple times. In the end, the colour-connected partons form on-shell hadrons.

An alternative model for the parton shower is provided by HERWIG [67, 68]. It uses cluster fragmentation instead of the string model from PYTHIA. In this model, all gluons are split into $q\bar{q}$ pairs and then close-by quarks are merged to colourless clusters. These clusters then may split and finally decay into hadrons. In this thesis, HERWIG is used in combination with the MC@NLO matrix element generator.

4.3 Underlying Event

As the colliding protons consist of more partons than just the two interacting in the hard process, the other partons will also hadronise and produce additional particles. In addition, these partons can interact with each other. These effects are summarised in the underlying event description, using the Z2* tune [58] at CMS.

4.4 Pileup

Furthermore, multiple interactions can happen during one bunch crossing at the LHC, due to the high instantaneous luminosities. They are called pileup and are described by PYTHIA in the simulation. In the simulation, there is no connection between the different interactions.

4.5 Detector Simulation

As the final step, all generated stable particles are passed to the detector simulation with GEANT4 [59]. This simulation includes the full geometry of the CMS detector and its materials, the magnetic field, and an approximation to the electronic readout. This way, a direct comparison to the data taken with the detector can be done.

Chapter 5

Reconstruction

In this chapter, the reconstruction of high-level objects from the output of the detector, described in chapter 3, is outlined. Firstly, the software will be introduced, then the particle flow concept is presented and details of the jet reconstruction are discussed, and finally kinematic fitting will be explained.

5.1 Software

The software used for the reconstruction by CMS is called `CMSSW` [69]. The software version used for this analysis is `5.3.14 patch2`. Several important parameters needed for the reconstruction of objects are stored in a central database. For processing data and simulated samples the parameter sets `FT53_V21A_AN6` and `START53_V27` are used, respectively. The differences for data and simulated samples originate from slightly different detector geometries and readout.

5.2 Particle Flow

In the particle flow concept [70], an event is interpreted in its entirety, as all detector components are combined to improve the event reconstruction. In the beginning, tracks are reconstructed and calorimeter entries are clustered. Then these are combined to particle candidates, which are classified. The different kinds of particles that can be reliably resolved in the detector and therefore are distinguished by the particle flow algorithm are muons[1], electrons[1], photons, and charged and neutral hadrons. An overview of these particle types and their signatures can be found in Figure 5.1.

[1] Refers to the respective antiparticle as well

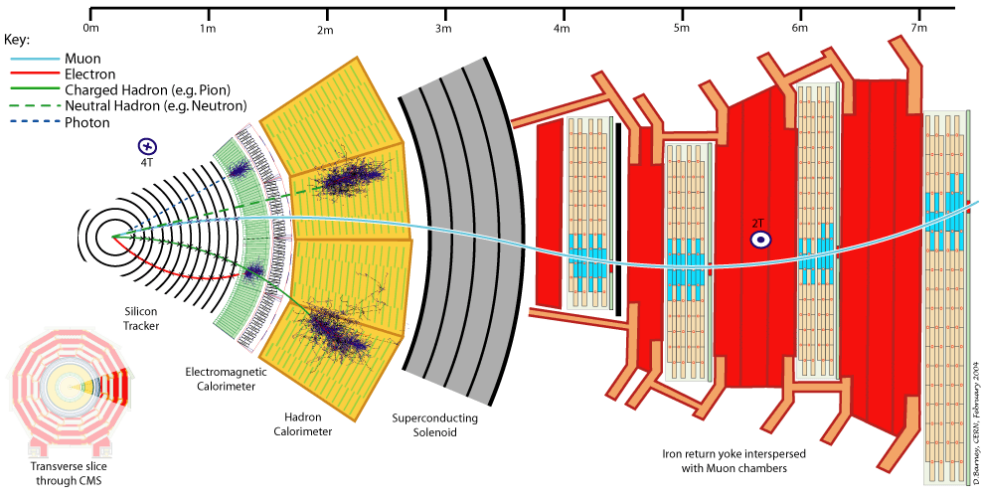

Figure 5.1: Slice through the CMS detector with particle signatures shown. Figure taken from [71].

5.2.1 Reconstruction of Tracks and Calorimeter Clusters

Tracks of charged particles are reconstructed for transverse momenta of at least 150 MeV. Iteratively, tracks are reconstructed, their hits in the tracker are removed, and the requirements on any further tracks are loosened, yielding an efficiency of above 99.5% for muons and still more than 90% for charged hadrons with a fake rate in the order of 1%. The energy resolution of the tracker is superior to the energy resolution of the calorimeters over most of the energy range. For example, the average constituents transverse momentum for a jet with a transverse momentum of 500 GeV is still in the order of 10 GeV. Here, the energy resolution of the tracker is ∼2% compared to ∼10% for the whole jet in the hadronic calorimeter.

In the calorimeters, the energy deposits are clustered separately in each subcomponent (EB, EE, HB, HE, HF, see section 3.2.2). From seeds, which are clusters with an energy deposition of at least two standard deviations above the electronics noise, the clustering of energy deposits is started.

5.2.2 Linking of Energy Deposits

When track reconstruction and energy clustering in the calorimeters are done, the two collections have to be linked in order to avoid double counting. As a first step, each track is extrapolated from its last hit in the tracker one interaction length deep into the hadronic calorimeter. Then, all penetrated clusters are associated to the track. To take into account gaps between cells, cracks between modules, the uncertainty of the position of the shower maximum, and multiple scattering of low momentum particles, the cluster boundaries can be extended by up to one cell width. In order to account for possible Bremsstrahlung photons, tangents into the electromagnetic calorimeter are interpolated from the intersection points of the track with the tracker layers. Clusters on these tangents are linked as possible Bremsstrahlung. In a last linking step, the tracks from the tracker and the muon system are matched using a χ^2-fit.

5.2.3 Identification of Particles

As first step in the identification of the particles, tracks with a successful matching in the last linking step are considered as muons and all their energy deposits are removed from further processing. This step is followed by the electron reconstruction. Here, tracks with their associated entries in the electromagnetic calorimeter and possible Bremsstrahlung photons are identified as electrons and again, all their identified components are removed from the processing.

For the next step, tracks are considered if their relative energy resolution is smaller than the relative calorimetric energy resolution for charged hadrons, rejecting 0.2% of the tracks, 90% being fakes and 10% being measured more precisely in the calorimeters. If one track has several matches in the calorimeter, only the closest one is kept. The energies of tracks pointing to a cluster in the hadronic calorimeter are subtracted from the clusters energy. If the track energies exceed the energy of the cluster in the hadronic calorimeter, clusters in the electromagnetic calorimeter are added. The quality criteria for the tracks are relaxed further if the track energies are still larger by more than three standard deviations. In such a case, a search for muons and fake tracks is done and imprecisely measured tracks are removed. These tracks for one cluster are identified as charged hadrons with the mass of a charged pion. If track and cluster energies are compatible within measurement uncertainties, the charged hadrons are redefined by a global fit of both track and cluster energy. This is especially relevant for high energies and pseudorapidities. If the cluster energy surpasses associated track energies, the excess is interpreted as a photon or a neutral hadron. If this superabundance is smaller than the total energy in the electromagnetic calorimeter, only one photon will be reconstructed. Otherwise, a photon with energy measured in the electromagnetic calorimeter and a neutral hadron with an energy measurement in the hadronic calorimeter are reconstructed. All remaining energy deposits in the calorimeters, not associated to any track, are reconstructed as photons and neutral hadrons, respectively.

The missing transverse energy $E_{\mathrm{T}}^{\mathrm{miss}}$ is calculated from the complementary sum of the four-vectors of all components with its pseudorapidity set to zero. Typically, jets consist of ∼65% charged hadrons, ∼25% photon, and only ∼10% neutral hadrons and thus particle flow gives a good handle on improving the jet energy resolution compared to using only the calorimeter for the jet reconstruction.

5.2.4 Charged Hadron Subtraction

The particle flow concept gives an improved handle on the mitigation of pileup effects. Every track that can be associated to a vertex other than the one of the most energetic interaction and its secondary vertices is discarded. This way, most charged particles out of pileup interactions can be identified and ignored in the further event reconstruction.

5.3 Jet Reconstruction

As jets are the most important objects in this thesis a detailed introduction is given. Firstly, the algorithm to create the jets is described. Afterwards, corrections of the jet energies and their uncertainties are presented and resolutions are derived. Finally, the concept of identifying jets originating from bottom quarks is introduced.

5.3.1 Jet Reconstruction Algorithm

The jets are clustered from particle flow objects. To unambiguously assign the particles to jets, a jet algorithm is used. At the CMS experiment, the default algorithm is the so-called anti-k_{T} algorithm [72] with a radius parameter of $R = 0.5$. This algorithm effectively clusters particles around the highest p_{T} objects, until the maximally allowed distance is reached. For the clustering procedure the following equations are used:

$$d_{ij} = \min\left(p_{t,i}^{-2}, p_{t,j}^{-2}\right) \frac{\left(y_i - y_j\right)^2 + \left(\varphi_i - \varphi_j\right)^2}{R^2} \tag{5.1}$$

$$d_i = p_{t,i}^{-2} \tag{5.2}$$

Here, y denotes the rapidity of the object defined as:

$$y = \frac{1}{2} \ln\left(\frac{E + p_z}{E - p_z}\right) \tag{5.3}$$

As first step, all d_{ij} and d_i are searched for the minimum. If the minimal value is a d_{ij}, the corresponding two objects i and j are fused to a single object and the first step is repeated. If a d_i is the smallest value, the corresponding object i is declared as final-state jet and is removed from further processing. When no more particles remain, the process is finished.

5.3.2 Jet Energy Corrections

The CMS experiment uses a factorised approach to derive and apply corrections to the jet energy (JEC). The JEC scheme is illustrated in Figure 5.2.

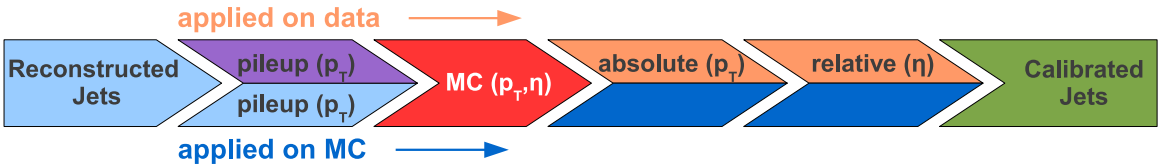

Figure 5.2: Overview of all steps in the CMS jet energy correction scheme. Figure kindly provided by [73].

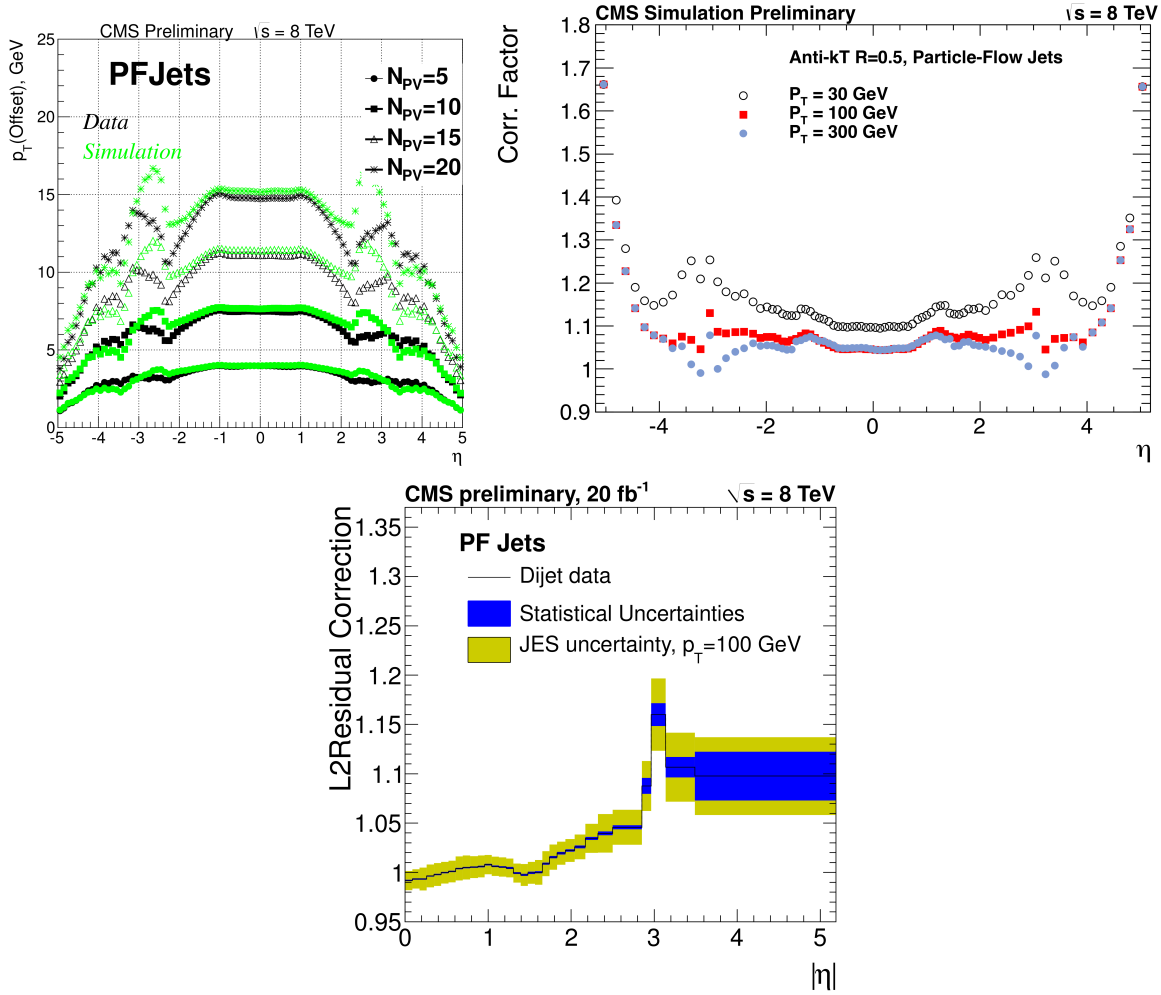

Figure 5.3: The correction factors for the pileup correction for different number of primary vertices N_{PV} (top left), the simulation based correction for different jet transverse momenta p_{T} (top right), and the residual correction for data (bottom) are shown. Figures taken from [75].

As a first step, a correction for the remaining pileup effects not accounted for by the charged hadron subtraction is applied with separate corrections for data and simulation. Next, a correction based on the p_{T} and η of the jets derived from the simulation is applied. Afterwards, a residual correction is applied on data only, which takes into account differences of the simulation compared to the data using Z+jet, γ+jet, and dijet events. In Figure 5.3 the corresponding correction factors are shown. Details on the jet energy corrections used in CMS can be found in [74, 75].

5.3.3 Jet Energy Uncertainties

There are several sources contributing to the uncertainty of the jet energies. Some originate from the methods used to derive the corrections and others take into account differences in the modelling of jets in different simulations. For an easier combination of top-quark mass measurements between different experiments, it was decided to group the jet energy uncertainties corresponding to their correlation among the different experiments. The different groups are: MPFInSitu, Flavour, and InterCalibration, all being partially correlated between the experiments. The remaining uncorrelated uncertainty sources make up the last group. The MPFInSitu uncertainty covers differences observed in the $E_{\mathrm{T}}^{\mathrm{miss}}$ projection on a jet versus a final-state radiation indicator in data and simulation. The Flavour uncertainty is taken from the difference in modelling of jets in PYTHIA and HERWIG++. The η-dependent InterCalibration uncertainty stems from the modelling of final-state radiation. The uncertainties for jets from the different correlation groups and for jets originating from different flavours are shown in Figure 5.4.

One additional source of a systematic uncertainty is the difference between a p_{T}-dependent and a flat residual correction for data only. This source is listed separately and is treated as uncorrelated.

5.3.4 Jet Resolutions

The resolutions of a jet with respect to its generating partons are derived as functions of the transverse energy and the pseudorapidity for the transverse energy, the pseudorapidity, and the azimuthal angle. For this purpose, the jets are matched to the generated partons. The angular distance between jet and parton is defined as:

$$\Delta R = \sqrt{(\varphi_1 - \varphi_2)^2 + (\eta_1 - \eta_2)^2} \tag{5.4}$$

If a parton is found within $\Delta R < 0.4$ of the jet axis, the jet is considered as matched to that parton. If there are multiple matched partons for one jet, the closest match is used. The resolution is derived in simulation only. The resolutions in data are found to be worse by 7-20%, depending on the pseudorapidity of the jet, compared to the simulation [74]. The simulated data sets and the resolutions determined here, are corrected for this observed differences.

The resolutions $\sigma\left(E_{\mathrm{T}}^{\mathrm{rec}}/E_{\mathrm{T}}^{\mathrm{gen}}\right)$, $\sigma\left(\eta^{\mathrm{rec}}\right)$, and $\sigma\left(\varphi^{\mathrm{rec}}\right)$ are determined for each ring in η of the calorimeter. Examples of the resolutions are shown in Figures 5.5 and 5.6.

5.3.5 B Tagging

As bottom quarks play a crucial role in the top-quark decay, it is useful to identify jets originating from bottom quarks. Mesons containing bottom quarks have a comparably long lifetime and therefore usually travel up to a few hundreds of micrometres in the detector before they decay. This gives the possibility to tag the jet with the help

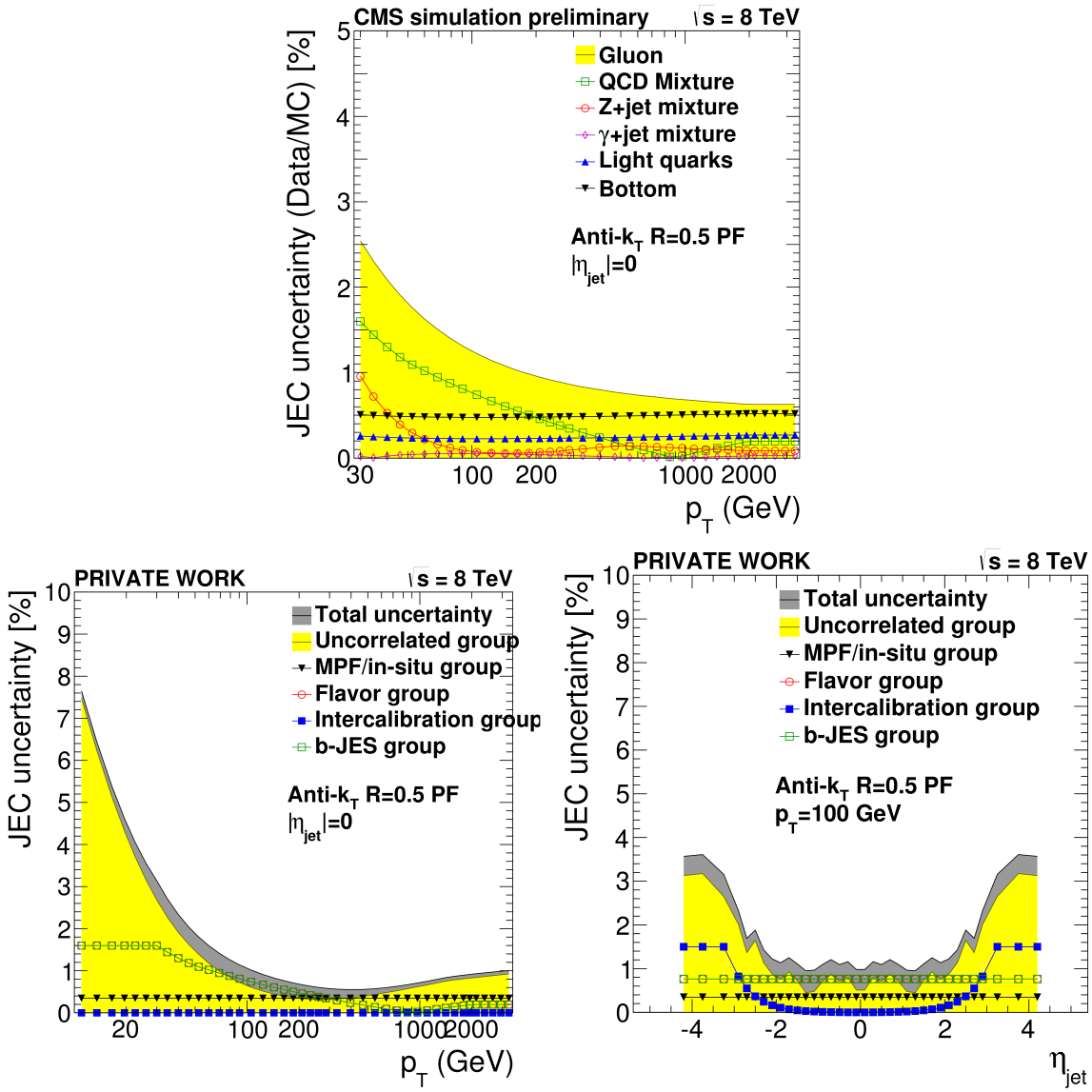

Figure 5.4: On the top, the jet energy uncertainties for jet originating from different flavours is shown. Figure taken from [75]. On the bottom, the jet energy uncertainties for the different correlation groups are shown. On the left as function of p_{T} on the right as function of η. Figures kindly provided by [73].

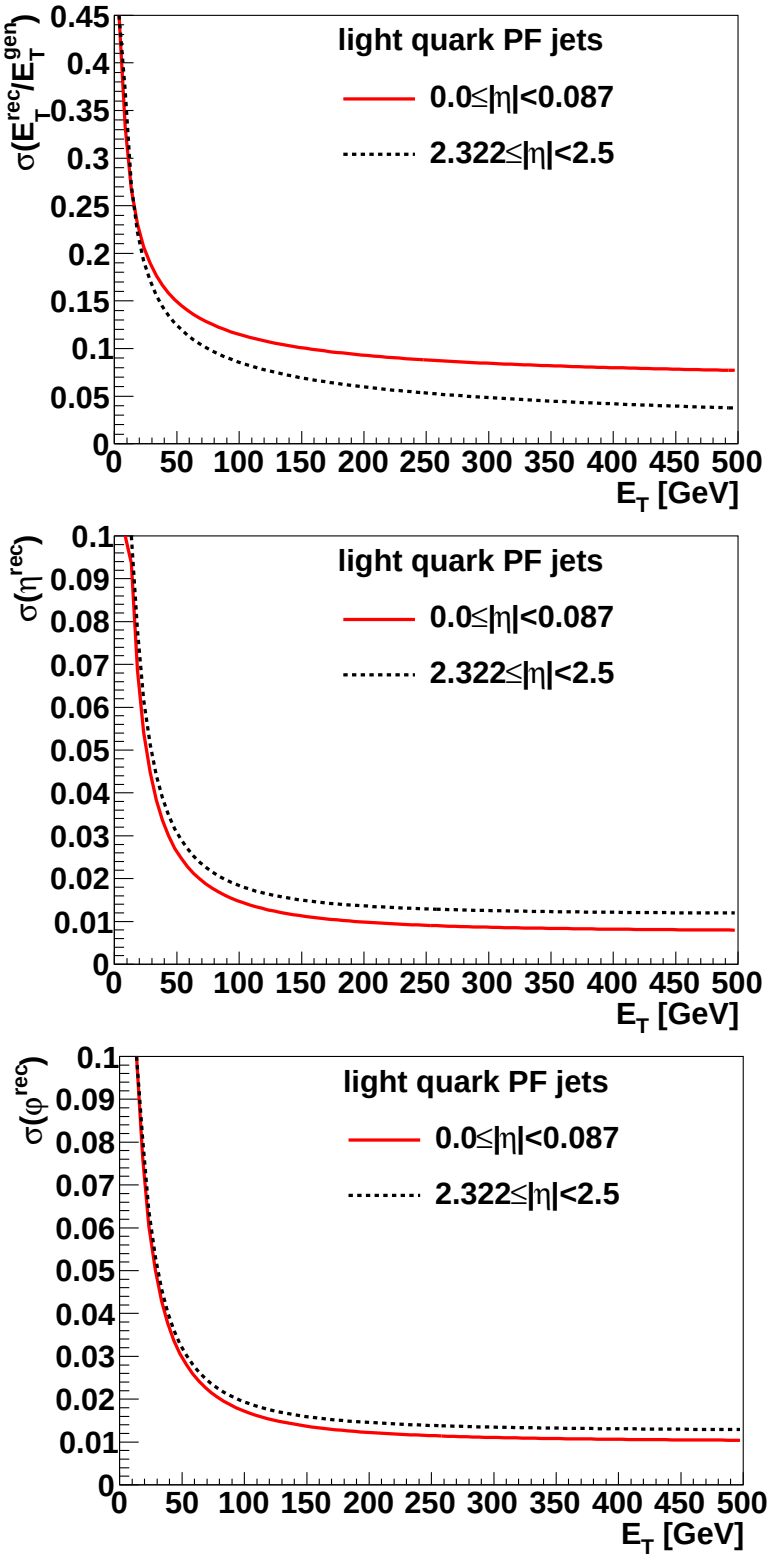

Figure 5.5: Resolutions of reconstructed light quark jets in simulation with respect to their generated particles for E_{T} (top), η (middle), and φ (bottom). They are shown for two slices in η of the calorimeter. The solid red line corresponds to the central region of the detector and the dashed black line to the most forward region used in this analysis, being in the endcaps of the calorimeters. Figures kindly provided by [76].

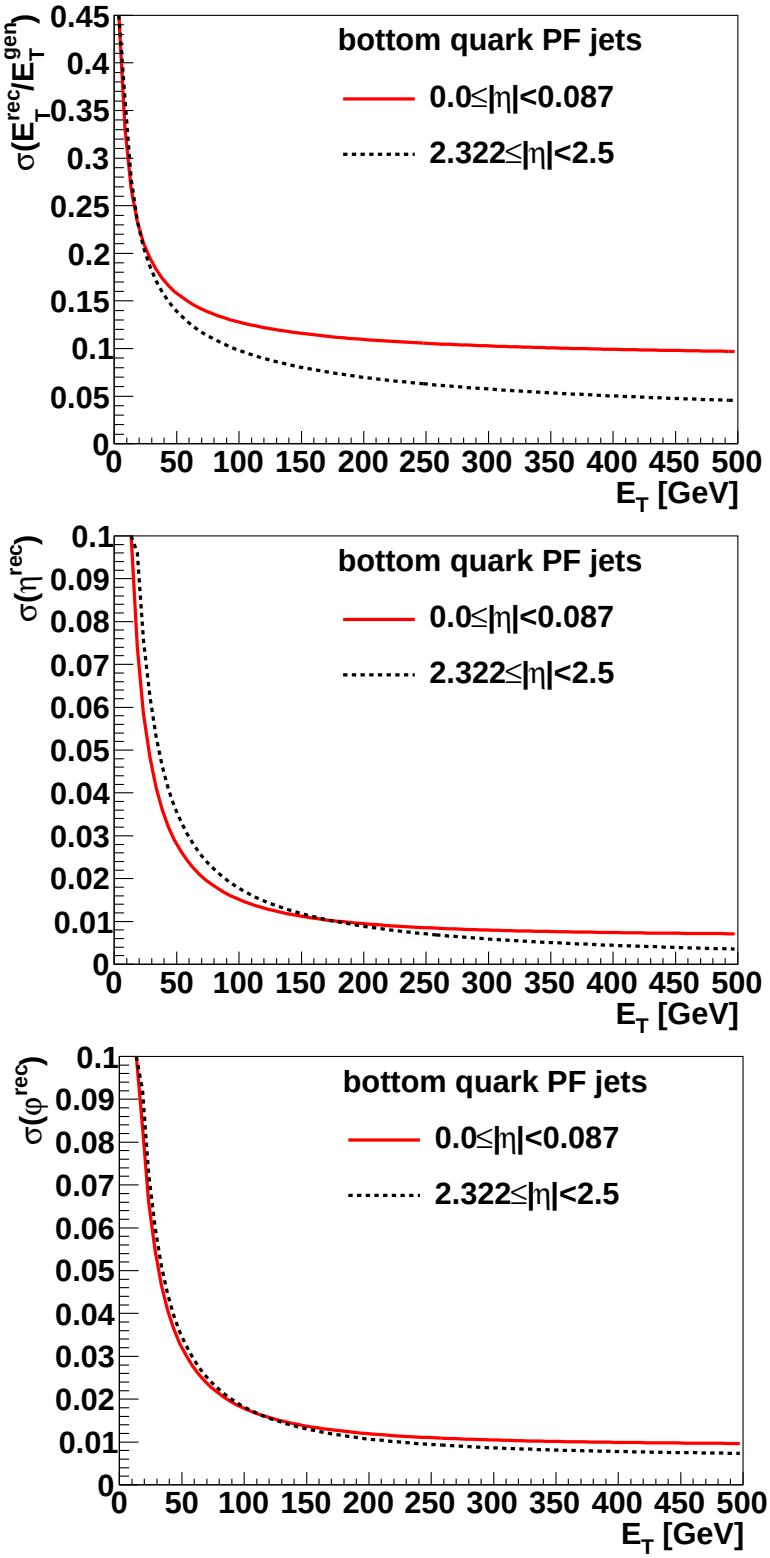

Figure 5.6: Resolutions of reconstructed bottom quark jets in simulation with respect to their generated particles for E_{T} (top), η (middle), and φ (bottom) . They are shown for two slices in η of the calorimeter. The solid red line corresponds to the central region of the detector and the dashed black line to the most forward region used in this analysis, being in the endcaps of the calorimeters. Figures kindly provided by [76].

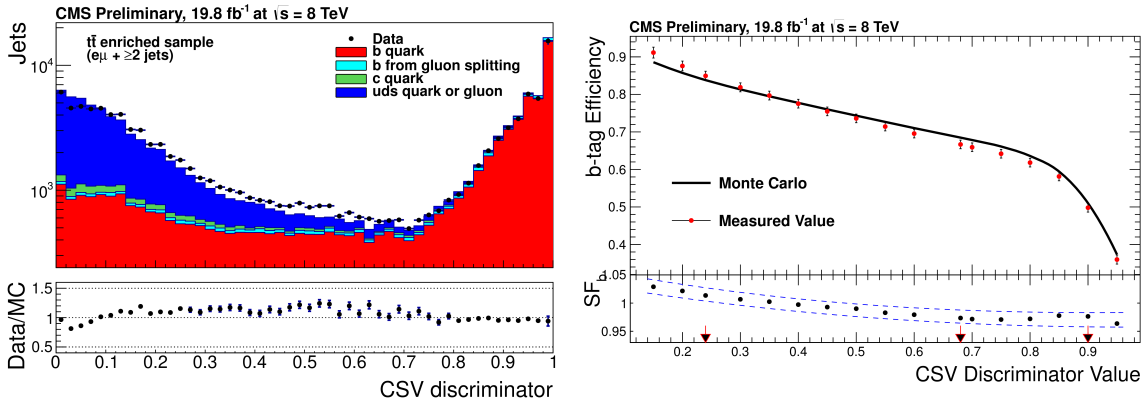

Figure 5.7: The distribution of the b-tag discriminator (left) taken from $t\bar{t}$ events in the eμ-channel. Scale factor (right) that has to be applied to simulated samples to account for differences to data. The small arrows on the x-axis indicate the three officially provided working points for this b-tagging algorithm. Figures taken from [78].

of their secondary vertices, created by the delayed decay of the bottom meson. The Combined Secondary Vertex algorithm [77], which is used for this, makes use of several quantities to give the best possible discrimination between jets containing bottom mesons and all other jets. Some examples of quantities used in this algorithm are: the flight distance significance in the transverse plane, the secondary vertex mass, and the number of tracks at the secondary vertex. Several working points are defined for this algorithm. The working point used in this analysis is the most stringent one, featuring the lowest available misidentification rate of approximately 0.1%. In Figure 5.7 the b-tag discriminator and the b-tag efficiency scale factor that has to be applied to simulated samples to account for differences compared to data are shown. This scale factor is derived as simple ratio of the b-tag (misidentification) efficiency determined in data and in simulated samples for dedicated event selections. Details on b tagging in 8 TeV data and the determination of the scale factor can be found in [78].

5.4 Kinematic Fit

A very important ingredient of this analysis is the kinematic fit [79, 80]. This is a least-squares fit of the jets in the event under certain constraints. The constraints arise out of the event topology of the desired final state. As in the all-jets top-quark pair final state the four non-bottom-quark jets are expected from two W bosons, the first natural choice for a constraint is to combine these jets in such a way that they add up to the W-boson mass of 80.4 GeV [15]. The next natural choice is to require that the masses of the two reconstructed top quarks should be equal. The top-quark mass is not fixed to avoid any bias for the top-quark mass measurement.

During the kinematic fitting process, the kinematic quantities (the transverse energy E_{T}, the pseudorapidity η, and the azimuthal angle ϕ) of the jets are optimised to find

parameter	value
$N_{\text{max}}^{\text{iter}}$	500
ϵ_{thresh}	$1 \cdot 10^{-4}\,\text{GeV}$
$\Delta\chi^2_{\text{min}}$	$5 \cdot 10^{-5}$

Table 5.1: Parameters used for the kinematic fit of the events.

the solutions with the minimal χ^2:

$$\chi^2 = \sum_i \sum_j \frac{\left(i_{j,rec} - i_{j,fit}\right)^2}{\sigma_{i_j}^2} + \sum_c \lambda_c d_c \qquad (5.5)$$
$$\text{with } i = E_{\text{T}}, \eta, \phi,\ j = \text{jets and } c = \text{constraints}$$

The masses of the jets are set to zero in the fitting procedure. The fit is done under the assumption of Gaussian resolutions σ_{i_j} of these kinematic quantities, while the constraints d:

$$\begin{aligned} d_{m_{\text{W}}} &= m_{\text{W}}^{\text{fit}} - m_{\text{W}} \\ d_{m_{\text{t}}} &= m_{\text{t}}^{\text{fit,1}} - m_{\text{t}}^{\text{fit,2}} \end{aligned} \qquad (5.6)$$

have to be fulfilled within a certain accuracy margin ϵ_{thresh}:

$$|d_{m_{\text{W}}^1}| + |d_{m_{\text{W}}^2}| + |d_{m_{\text{t}}}| < \epsilon_{\text{thresh}} \qquad (5.7)$$

More details on least-squares fits can be found in [79, 80].

The process of minimisation is stopped and it is assumed to have reached the minimum once the χ^2 is changing by less than $\Delta\chi^2_{\text{min}}$. The minimisation is aborted if a maximum number of iterations $N_{\text{max}}^{\text{iter}}$ is reached. The parameters are listed in Table 5.1.

The resolutions used in the kinematic fitting process are assumed to be Gaussian. They are derived as functions of transverse energy and the pseudorapidity for jets originating from bottom quarks and lighter quarks, separately. Details on the derivation of the resolutions can be found in section 5.3.4.

To find the correct association of jets to partons, the minimisation procedure is repeated for every distinguishable jet permutation (720 in total). The number of distinguishable permutations is reduced by a factor of two for each W boson and another factor of two for the two decay branches because it is not possible to distinguish quarks from antiquarks. The information that two b-tagged jets are required in this analysis is used to aid the kinematic fitting procedure. Therefore, b-tagged jets are only assigned to bottom quarks and untagged jets are only assigned to light quarks from the W-boson decay. This leaves six distinguishable permutations for an event with two b-tagged jets and four untagged jets. If the fit converges for multiple permutations in one event, the permutation with the lowest χ^2 is taken. The probability of the kinematic

fit for n degrees of freedom is defined by $P\left(\chi^2\right)$:

$$P\left(\chi^2\right) = \left[2^{n/2}\Gamma\left(\tfrac{n}{2}\right)\right]^{-1} \int_{\chi^2}^{\infty} t^{n/2-1} e^{-t/2} dt \tag{5.8}$$

$$\Gamma(x) = \int_0^{\infty} t^{x-1} e^{-t} dt$$

The probability should be flat for correct permutations if the assumed constraints are fulfilled and if the object resolutions are correct.

The kinematic fit for this signature is evaluated in great detail in [81]. The summarised findings are that choosing the permutation with the lowest χ^2 biases the probability distribution to higher values (instead of the expected flat distribution). In addition, small non-Gaussian tails in the jets resolutions lead to a bias of the χ^2 to smaller values. In combination, these effects lead to a probability distribution that is almost flat again, as originally expected, but with an additional sharp peak at zero from the non-Gaussian parts of the resolutions. After introducing some further ingredients of the analysis like the selection of the events (see section 6.1) and estimation of the background (see section 6.3), the validity of the fit results is shown in section 6.4. The shifts of the kinematic fit are shown in Figure 6.8 and the probability is shown in Figure 6.11 (top left).

Chapter 6

Measurement of the Top-Quark Mass

Using the objects and techniques described in chapter 5, the selection of events of interest is outlined in section 6.1. The ideogram method for extracting the top-quark mass is introduced in section 6.2. The background is estimated from data as described in section 6.3. In section 6.4, a set of control distributions is shown. Templates are created from the simulated samples (see chapter 4) and the data-driven background. They are illustrated in section 6.5. The analysis code used for this analysis as technical basis is presented in section 6.6. Afterwards, the calibration of the measurement is detailed in section 6.7. In the end, the systematic uncertainties are evaluated in section 6.8 and the results are presented in section 6.9.

The framework used in this thesis has been developed, tested, and used in collaboration with the measurement of the top-quark mass from lepton+jets events [7, 82].

6.1 Selection of Events

The data used in this analysis was collected at a centre-of-mass energy of 8 TeV in 2012. The very first step of the selection procedure is the requirement of a specific trigger. The trigger used for this analysis is the HLT_QuadJet50, requiring at least four jets on trigger level with a transverse momentum above 50 GeV. Only calorimeter information is used for the triggering in multijet signatures leading to the need of an additional selection criterion later in the selection procedure. There are three different types of L1Ts being used as seeds for the HLT_QuadJet50: four jet triggers, two jet triggers, and triggers requiring a minimal total energy in the calorimeters. In total up to nine different L1Ts are used as seeds ensuring full efficiency at this stage.

This trigger necessitates the use of the so-called parked primary data sets for multijet signatures from CMS, named "MultiJet1Parked". The parking of data sets was introduced during the 2012 run of the LHC. Here, parking means that data were recorded during the taking of data, but unlike the standard data sets they were not

reconstructed with the CMS software until after the 2012 LHC run was finished and the LHC was shut down for an upgrade. This way, huge amounts of additional data could be saved (about 160 TB for the multijet signatures) at the expense of computing time, which was available during the upgrade time. The parking of data sets was started after the first running period of 2012 (called Run2012A) was finished, so that only the later periods (called Run2012B-D) are available. Even in the beginning of the second running period, filters on the triggers in the parked data sets were set to record only a limited number of events, so-called prescales. After it became clear that the parking of data sets worked as expected, the prescales were removed. This leads to a collected integrated luminosity of $18.2\,\mathrm{fb}^{-1}$ stored for the HLT_QuadJet50. Compared to the total luminosity of $19.7\,\mathrm{fb}^{-1}$ that has been delivered, this results in a loss of $1.5\,\mathrm{fb}^{-1}$ corresponding to about 8% of the total data set. The list of data sets can be found in Appendix A.

For an unbiased determination of the trigger efficiency an independent data set is needed. Therefore, the trigger efficiency is determined requiring an isolated muon with a transverse momentum above 25 GeV and an absolute value of η below 2.1 in the trigger (HLT_IsoMu25Eta2p1). In this data set, the turn-on behaviour of the jet trigger as function of the fourth highest transverse momentum of the jets in the offline reconstruction is evaluated. As this turn-on behaviour for particle flow jets is not satisfying, the trigger efficiency is determined for calorimeter-based jets. Due to a reduced granularity of the calorimeter reconstruction, not fully optimised detector read-out calibration, and the usage of simplified and preliminary jet energy corrections, the calorimeter-based jets at trigger level still differ slightly from the fully reconstructed offline calorimeter-based jets. The resulting turn-on curve is shown in Figure 6.1. In order to be in the plateau region of the trigger efficiency, the next selection step requires that the fourth highest transverse momentum of the calorimeter-based jets in the offline reconstruction is above 60 GeV and that it is found in the central region of the detector with an absolute value of η below 2.4. The resulting trigger efficiency can be seen in Figure 6.1.

In Figure 6.2, the efficiency of selecting an event versus the transverse momentum of the fourth particle flow jet is shown after the selection on the fourth calorimeter-based jet is done. A good agreement of data and simulated samples is found. As can be seen in Figure 6.2 reaching the plateau of the efficiency as function of the transverse momentum of the fourth particle flow jet would have needed a much more stringent requirement. Thus, the criterion on the transverse momentum of the fourth calorimeter-based jet is preferred. The differences of offline calorimeter-based and particle flow jets is assumed to be described by simulation. In order to account for possible remaining differences, a systematic uncertainty will be applied on this later on (see section 6.8.6).

As six jets are expected in the final state of the all-jets top-quark pair process, the next step is to require at least six jets, reconstructed with the particle flow algorithm (see section 5.2). The four jets with the largest transverse momentum are required to have at least 60 GeV, two more jets are required to have a transverse momentum of at least 30 GeV. For all jets, the absolute value of η should be below 2.4, where the fiducial volume of the tracker ends. For larger values of $|\eta|$, the performances of the

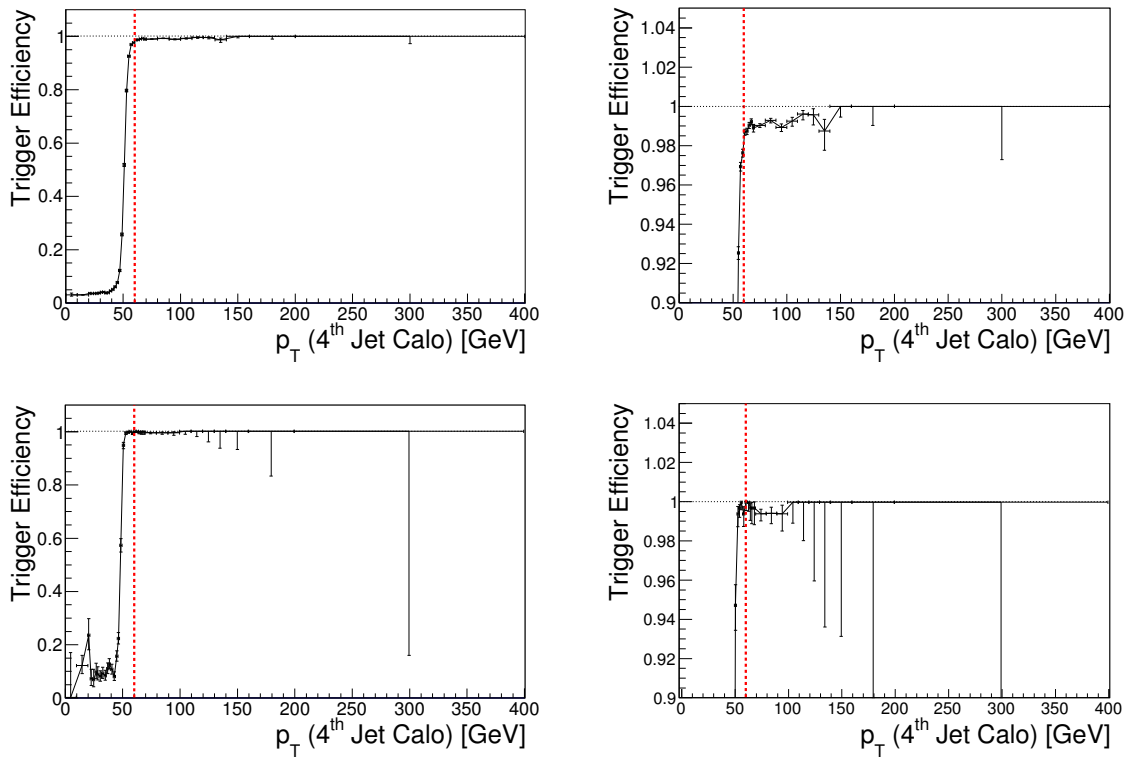

Figure 6.1: Turn-on curves for the trigger efficiency versus the fourth highest transverse momentum of the calorimeter-based offline jets. The events are selected with an independent trigger (HLT_IsoMu25Eta2p1). At the top (bottom) the data (simulated sample) is shown. On the right, a zoom around an efficiency of one is shown. In order to reach the plateau of the trigger efficiency, only events with a transverse momentum of the fourth jet above 60 GeV are used as indicated by the dashed, red line.

particle flow algorithm and the b-tagging, required as next selection step, degrade.[1]

As two of the quarks in the top-quark decay are expected to be bottom quarks, b tagging (see section 5.3.5) is applied. Two of the first six selected jets are required to be b tagged. From the events selected at this step, the background is estimated. Details on the background estimation technique can be found in section 6.3. Afterwards, the kinematic fit (see section 5.4) is applied. On the kinematic fit result, two more criteria are imposed, namely that the goodness of fit probability $P\left(\chi^2\right)$ has to be larger than 0.1 and the distance in $\eta - \phi-$space (5.4) between the two bottom-quark candidates $\Delta R_{\mathrm{b\bar{b}}}$ must be larger than 2.0. The first criterion on the goodness of fit probability ensures that signal events are reconstructed well and the background is reduced largely

[1] At this point of the analysis, n-tuples are written for all later steps of the analysis. These n-tuples are based on `ROOT` [83] and are technically implemented as `TTrees` [84]. They are a slim data structure to save only the relevant information while keeping the advantage of having all correlations preserved. This enables a fast turn-around time for producing control distributions or to make small changes in the analysis. These n-tuples use less than 5 kB per event compared to about 400 kB for the standard CMS event format, called Analysis Object Data (AOD).

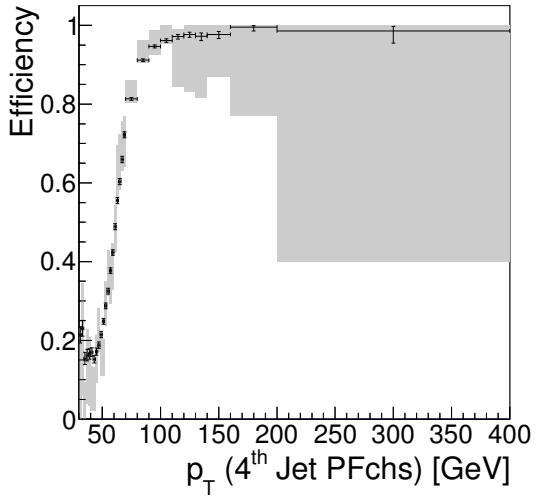

Figure 6.2: Turn-on curve of the particle flow jet with the fourth highest transverse momentum after selecting at least four calorimeter-based jets with a transverse momentum above 60 GeV. The grey shaded band shows the simulated sample and its statistical uncertainty, while the black line shows data with its statistical uncertainty.

Selection step	N_{data}	N_{MC}	f_{sig}
6 jets	11624823	205974	2%
2 b tags	271139	44666	16%
$P\left(\chi^2\right) > 0.1$ & $\Delta R_{\text{b}\bar{\text{b}}} > 2.0$	4356	3385	78%

Table 6.1: Number of selected events in data N_{data}, the expected number of events from the simulated sample N_{MC}, and estimated signal fraction f_{sig} in data after each selection step. The expected number of events from the simulated sample and the estimated signal fraction are derived assuming a cross section for the top-quark pair production of $\sigma_{\text{t}\bar{\text{t}}}(m_{\text{t}} = 173.3\,\text{GeV}) = 245.79\,\text{pb}$ [36].

as it does not fulfil the constraints imposed by the kinematic fit. The second criterion on the distance between the two bottom quarks helps to easily distinguish the two top quarks for the signal by requiring a more back-to-back like structure and further reduces the background from gluon splitting to bottom-quark pairs, which are usually rather collimated. These two selection criteria increase the fraction of signal events (correctly reconstructed top-quark pair events) from 16% to 78% (11% to 45%). The correctness of the reconstruction is found via jet-parton matching in the simulated sample and is detailed in section 6.2. In Table 6.1, an overview of the number of selected events in data, the number of expected events from the simulated sample, and the estimated fraction of signal events are given. After the introduction of the background estimation technique in the section 6.3 several control distributions are shown in section 6.4.

6.2 Ideogram Method

An ideogram method is used to extract the top-quark mass from the selected events [85, 86]. As the uncertainty on the knowledge of the jet energy scale (JES) is the leading systematic uncertainty in most previous measurements of the top-quark mass, an in-situ measurement using a jet energy scale factor (JSF) is done. This factor describes the deviation of the observed JES in this measurement from the default CMS JES.

According to the Bayes' theorem, the likelihood for a top-quark mass (m_t) and a JSF given a data sample is proportional to the likelihood for observing this sample given a top-quark mass and a JSF. This likelihood is the product of the individual likelihoods of the events. The individual event likelihoods use the top-quark mass from the kinematic fit ($m_\mathrm{t}^\mathrm{fit}$) and the reconstructed average W-boson mass before the kinematic fit ($m_\mathrm{W}^\mathrm{reco}$) as estimators for the top-quark mass and the JSF, respectively. The average of the two reconstructed W-boson masses is used, as it is less sensitive to fluctuations than the two individual masses giving a more stable distribution. The distributions are shown in Figure 6.11 and explained correspondingly in section 6.4.

$$\begin{aligned}\mathcal{L}\left(m_\mathrm{t}, \mathrm{JSF}|\mathrm{sample}\right) &\sim \mathcal{L}\left(\mathrm{sample}|m_\mathrm{t}, \mathrm{JSF}\right) = \prod_\mathrm{events} \mathcal{L}\left(\mathrm{event}|m_\mathrm{t}, \mathrm{JSF}\right) \\ &= \prod_\mathrm{events} P\left(m_\mathrm{t}^\mathrm{fit}, m_\mathrm{W}^\mathrm{reco}|m_\mathrm{t}, \mathrm{JSF}\right)\end{aligned}$$

The individual event likelihoods can be split into two parts, corresponding to the signal with a fraction of f_sig and the background component making up the remaining part. As the background does not contain any top-quark events and is derived from data directly, it does not depend on either m_t or JSF.

$$\begin{aligned}P\left(m_\mathrm{t}^\mathrm{fit}, m_\mathrm{W}^\mathrm{reco}|m_\mathrm{t}, \mathrm{JSF}\right) &= f_\mathrm{sig} \cdot P_\mathrm{sig}\left(m_\mathrm{t}^\mathrm{fit}, m_\mathrm{W}^\mathrm{reco}|m_\mathrm{t}, \mathrm{JSF}\right) \\ &+ \left(1 - f_\mathrm{sig}\right) \cdot P_\mathrm{bkg}\left(m_\mathrm{t}^\mathrm{fit}, m_\mathrm{W}^\mathrm{reco}\right)\end{aligned}$$

Two different types of permutations are distinguished via a matching of jets to partons: correct assignment of the jets to the originating partons (CP) and all other cases (OP), that include wrong and unmatchable permutations. This matching of jets to partons is done in the same way as for the determination of the jet resolutions (see section 5.3.4). The originating parton has to be found within $\Delta R < 0.3$ of the jet. The matching has to be unambiguous, meaning that only one originating parton may be found within each jet. The fraction of correct permutations in the simulated sample is 45%, while 54% of the events are not matched and 1% are reconstructed wrongly by the kinematic fit. The latter two cases of not matched and wrong permutations make up the category of other permutations.

Correspondingly, the signal component is split into the two different permutation types. The correlation of $m_\mathrm{t}^\mathrm{fit}$ and $m_\mathrm{W}^\mathrm{reco}$ after the kinematic fitting is 7.9% for correct

permutations and 3.3% for other permutations and thus is regarded as negligible. Hence, the signal probability density can be factorised into two components, depending only on either $m_{\mathrm{t}}^{\mathrm{fit}}$ or $m_{\mathrm{W}}^{\mathrm{reco}}$, respectively. Likewise, the background probability density can be factorised into two components depending only on either $m_{\mathrm{t}}^{\mathrm{fit}}$ or $m_{\mathrm{W}}^{\mathrm{reco}}$.

$$\begin{aligned} P_{\mathrm{sig}}\left(m_{\mathrm{t}}^{\mathrm{fit}}, m_{\mathrm{W}}^{\mathrm{reco}} | m_{\mathrm{t}}, \mathrm{JSF}\right) &= f_{\mathrm{CP}} \cdot P_{\mathrm{CP}}\left(m_{\mathrm{t}}^{\mathrm{fit}} | m_{\mathrm{t}}, \mathrm{JSF}\right) \cdot P_{\mathrm{CP}}\left(m_{\mathrm{W}}^{\mathrm{reco}} | m_{\mathrm{t}}, \mathrm{JSF}\right) \\ &+ (1 - f_{\mathrm{CP}}) \cdot P_{\mathrm{OP}}\left(m_{\mathrm{t}}^{\mathrm{fit}} | m_{\mathrm{t}}, \mathrm{JSF}\right) \cdot P_{\mathrm{OP}}\left(m_{\mathrm{W}}^{\mathrm{reco}} | m_{\mathrm{t}}, \mathrm{JSF}\right) \\ P_{\mathrm{bkg}}\left(m_{\mathrm{t}}^{\mathrm{fit}}, m_{\mathrm{W}}^{\mathrm{reco}}\right) &= P_{\mathrm{bkg}}\left(m_{\mathrm{t}}^{\mathrm{fit}}\right) \cdot P_{\mathrm{bkg}}\left(m_{\mathrm{W}}^{\mathrm{reco}}\right) \end{aligned}$$

In the end, the free parameters m_{t}, JSF, f_{sig}, and f_{CP} can be extracted by minimising $-2 \ln \mathcal{L}$. All variables can also be fixed to a specific value, so that for example also m_{t} can be extracted for the nominal JSF = 1 and the expected values of f_{sig} and f_{CP}. The shapes of these individual distributions composing the likelihood are described in section 6.5.

6.3 Data-Driven Multijet Background Estimation

Physical background processes that satisfy the full signal topology imposed by the kinematic fit via the W-boson and top-quark mass constraints (see section 5.4) do not exist. Even processes satisfying only two constraints are extremely rare. The background signature most similar to the top-quark pair signal is the production of a W-boson pair in association with a bottom-quark pair without intermediate top quarks. The cross section for this process is below 1% of the top-quark pair production cross section, thus it is negligible. Processes satisfying only one of the constraints imposed for the signal region have cross sections about one order of magnitude smaller than the top-quark pair production cross section. One good example here is the production of a W boson in association with a bottom-quark pair and a light-quark pair. However, as two constraints are not fulfilled, most of the events will be filtered out by the quality requirements of the kinematic fit selection (see section 6.1). All these background processes are found to be negligible after the full event selection.

The only remaining source of background events is multijet production in QCD, due to its enormous production cross section. One example Feynman diagram is illustrated in Figure 4.1 (right). Although none of the constraints is fulfilled by this processes directly, the huge production cross section leads to a sizable amount of background events. These events fulfil the expected event topology either due to mismeasurements of the jets or by chance almost directly. As the simulation of multijet processes in QCD is extremely difficult, the background is estimated using a data-driven event mixing technique. This technique offers the possibility to generate a very generic background distribution from data itself, which is not statistically limited.

The basic idea for the event mixing technique is that the specific event topology for signal events is only fulfilled by chance for the background. This implies that randomly

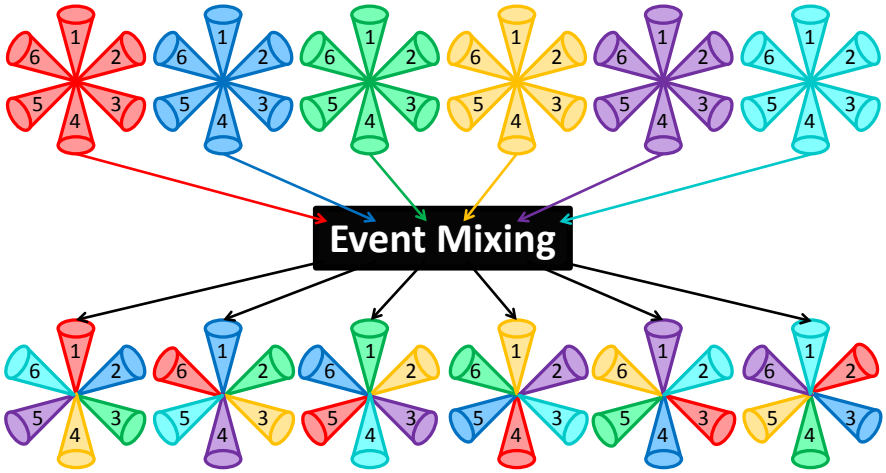

Figure 6.3: Illustration of the event mixing used for the background estimation.

chosen jets from different events give the same results for the kinematic fit as the background directly. This argumentation is supported by [87] that inspired the method developed in this thesis.

The ATLAS collaboration uses a similar, but much simplified, approach for the determination of the background for their top-quark mass measurement in all-jets final states [88]. Events with five jets are selected and additional jets with lower transverse momenta than the fifth jet are added from events with at least six jets. The CDF collaboration uses a weighting technique to derive a background distribution for their top-quark mass measurement in all-jets final states [10]. They derive a weight for b tagging any jet in a background dominated control region and apply this weight to the jets of events in the signal region.

Within this thesis, the events used for the mixing procedure are the selected events containing at least two b-tagged jets. Here, jets originating from different events are used to create a purely combinatorial background for the kinematic fitting procedure. The jet with the highest transverse momentum from one event is used, then the jet with the second highest transverse momentum from another event is added and so on. A simplified illustration of this technique can be found in Figure 6.3. Using this mixing technique, it is achieved that in the newly generated events no pair of two jets originates from the same original event. Hence, the background estimate contains no real W-boson or top-quark candidates, as it is expected from pure multijet background.[2]

Firstly, a list of jet permutations is created, one permutation for each of the new, to be generated events. Afterwards, the mixing itself is started. The particle flow jets with their constituents and the calorimeter-based jets are copied into the new event and the references of the particle flow jet constituents in the copied particle flow jets are set to the copied constituents. For each permutation in the list, a new event is

[2] Technically, the mixed events are produced in `CMSSW` using a secondary input source (`edm::VectorInputSource` [89]). This is done in a similar way as the mixing of pileup events in the standard CMS simulated samples. As a first step, a new, empty event (`edm::Event` [90]) is created (with the help of an `edm::EmptySource` [91]), then n_{mix} events (technically limited between zero and ten) are loaded into memory with the help of the secondary input source.

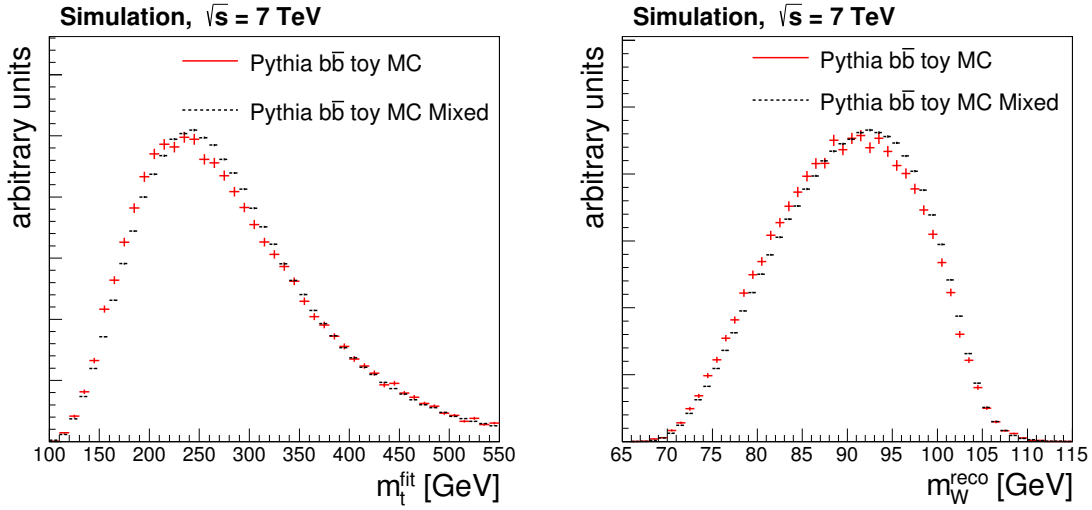

Figure 6.4: Validation of the background estimation using the event mixing technique at $\sqrt{s} = 7$ TeV. On the left, the top-quark mass from the kinematic fit and, on the right, the reconstructed average W-boson mass are shown.

created and the copying and resetting of jets and their constituents is repeated. Once all permutations are created, the events in memory are cleared, n_{mix} new events are read into memory, and the process is repeated until less than n_{mix} events remain. In this analysis, groups of $n_{\text{mix}} = 8$ events are used, keeping the computing time needed for the mixing at a reasonable level.

Albeit being very versatile, there are also some drawbacks of this method. Unfortunately, properties of the whole event, like the missing transverse energy or the transverse momentum of the top-quark pair system (see Figure 6.9 (bottom left)), are not reproduced well. Nevertheless, the event mixing method is able to properly predict invariant masses as well as kinematic distributions of constituents of the top-quark pair system, as will be shown throughout the next section.

To ensure a proper prediction of the relevant distributions for this measurement, a special simulated sample is produced. To validate this method, a large amount of multijet background events is needed. Due to the tight b-tagging requirements, it is expected that the main background originates from events containing real bottom quarks. Therefore, a sample containing $gg \to \text{b}\bar{\text{b}}$ events is chosen to validate the background estimation method. This sample is produced with PYTHIA and without a detector simulation due to CPU time limitation. This validation is done at $\sqrt{s} = 7$ TeV. It is found that the mixing technique can reproduce the shape of the relevant distributions of $m_{\text{t}}^{\text{fit}}$ and $m_{\text{W}}^{\text{reco}}$ well. The results can be seen in Figure 6.4. The small residual differences observed are covered by the systematic uncertainty assigned to the shape of these distributions. Details on the systematic uncertainty are explained in section 6.8.7.

The event mixing technique provides only the shapes of the distributions. Therefore, the multijet background is scaled such that it makes up the difference in the number of events between data and the simulated top-quark pair sample. This simulated top-quark pair sample itself is scaled such that the complete sample gives the expected number of events from NNLO calculations [36]. This yields a fraction of 22% of background events.

6.4 Control Distributions After the Event Selection

For all control distributions found in this section, "$\mathrm{t\bar{t}}$ correct" refers to a correct match of jets to generated partons by the kinematic fitting procedure and "$\mathrm{t\bar{t}}$ other" refers to the remaining cases. More details on this are given in section 6.2. The top-quark pair component is taken from the simulated sample and is normalised to the inclusive top-quark pair production cross section at NNLO. The background is taken from data as described in section 6.3 and is normalised such that the integral of background and the simulated sample gives the number of events in data. In the following, prediction always refers to the combination of the simulated top-quark pair sample and the data-driven background. All distributions are shown after applying the event selection.

In the beginning, a very basic set of control distributions is presented. In Figure 6.5, the transverse momenta of the six leading jets are displayed. Some small slopes are visible in the data over prediction ratios. They are a result of a slight mismodelling of the top-quark transverse momentum distribution, which is observed by several analyses within CMS [92–95] and will be discussed later in the context of Figure 6.9 (middle left). When the top-quark transverse momentum distribution in the simulated sample is weighted to reproduce the data as described in [92], these ratios become flat. A systematic uncertainty is assigned for this effect as discussed in section 6.8.13. In Figure 6.6, the pseudorapidities and, in Figure 6.7, the azimuthal angles of the six leading jets are shown. They are all well described by the prediction. As expected, the pseudorapidities of the jets are peaking at a value of zero and are falling off symmetrically to both sides, whereas the azimuthal angles are completely flat.

In Figure 6.8, the shifts that are performed by the kinematic fit ($x^{\mathrm{fit}} - x^{\mathrm{reco}}$) are depicted. The shifts are separated for light (left) and bottom (right) quarks, as well as for the transverse momentum (top), the pseudorapidity (middle), and the azimuthal angle (bottom). For all the shifts, a good agreement between data and prediction is given indicating that the kinematic fit works as expected.

In Figure 6.9, the transverse momenta (left) and rapidities (right) (see Equation (5.3)) of the composed objects from the kinematic fit are presented. In Figure 6.9 (top left), the transverse momenta of the W bosons from the kinematic fit are shown. The agreement of data and prediction is good, although a very slight slope is visible in the data over prediction ratio. This is directly connected to the transverse momenta of the top quarks from the kinematic fit that are displayed in Figure 6.9 (middle left).

Two interesting effects are visible for transverse momenta of the top quarks from the kinematic fit. Firstly, there is a clear slope in the ratio of data over prediction. This slope is observed by several other analyses [92–95], as well. One reason for this might be a slight mismodelling of radiation in the simulated samples leading to higher transverse momenta of the top quarks. This effect is currently under investigation, one possible solution might be effects from NNLO, as an approximate NNLO calculation [96] yields exactly this difference. Full NNLO calculations of the top-quark pair production cross section as a function of the top-quark transverse momentum might prove or rule out this possible explanation. In the end, a systematic uncertainty is assigned for this effect (see section 6.8.13).

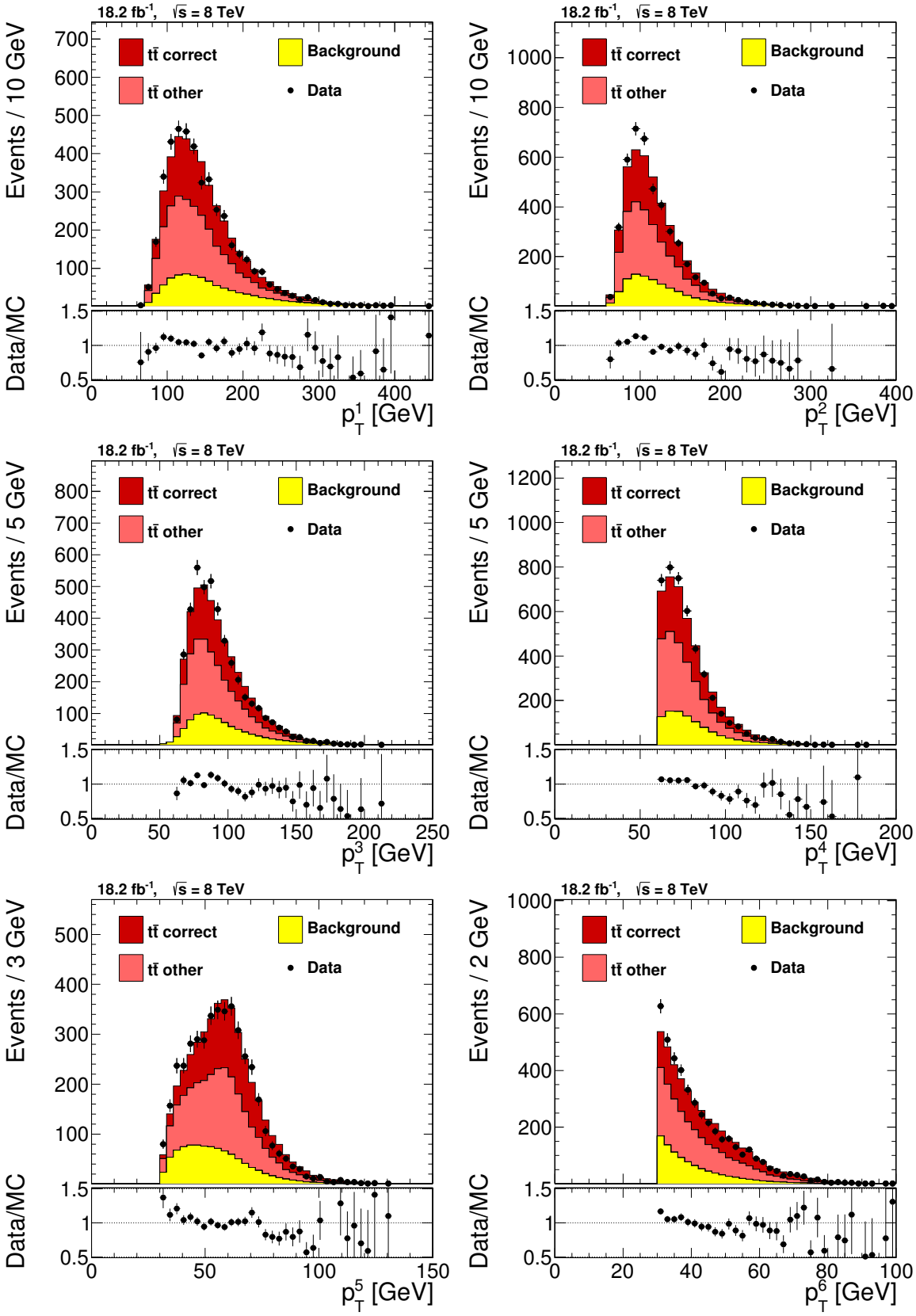

Figure 6.5: The transverse momenta of the six leading jets.

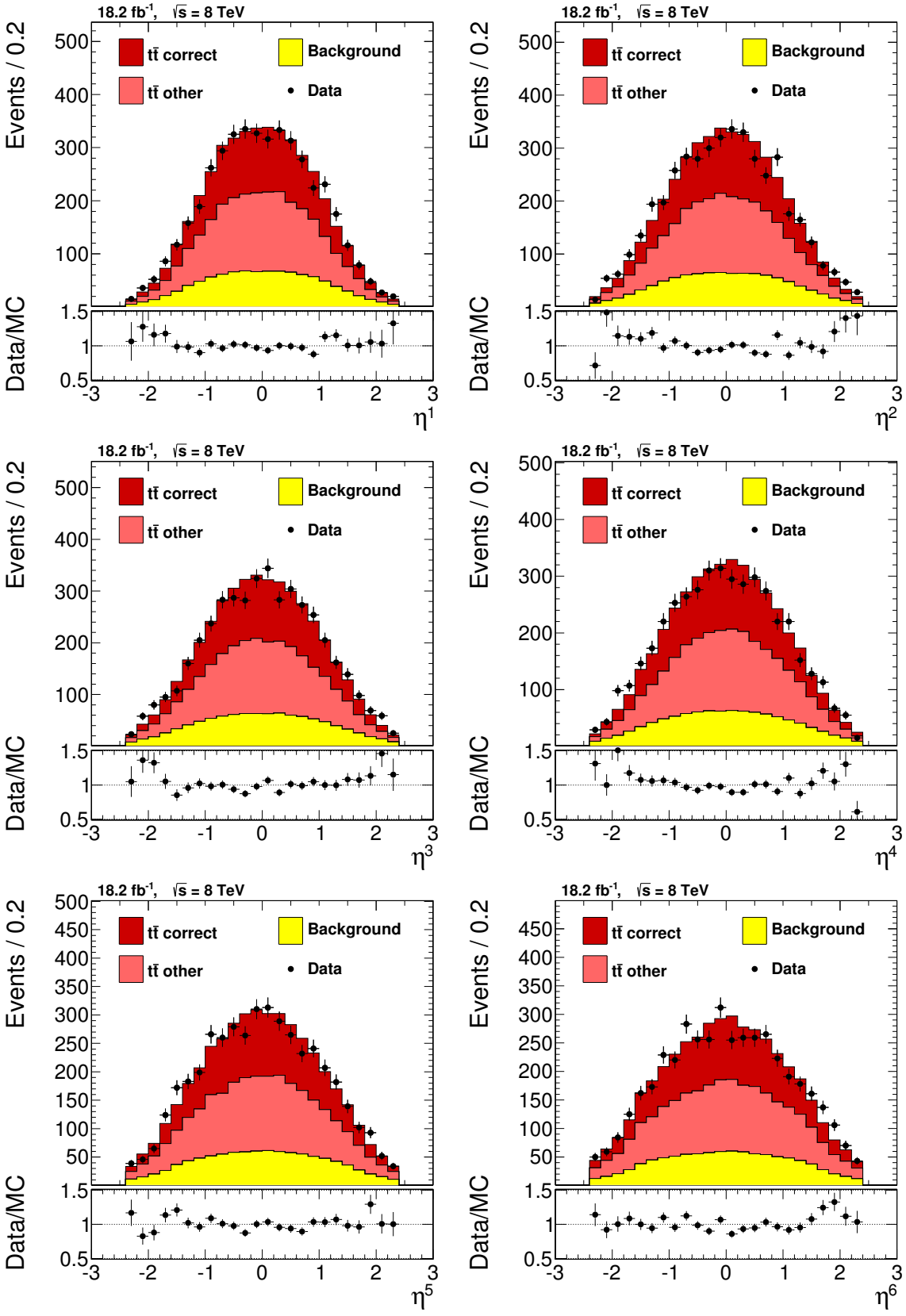

Figure 6.6: The pseudorapidities of the six leading jets.

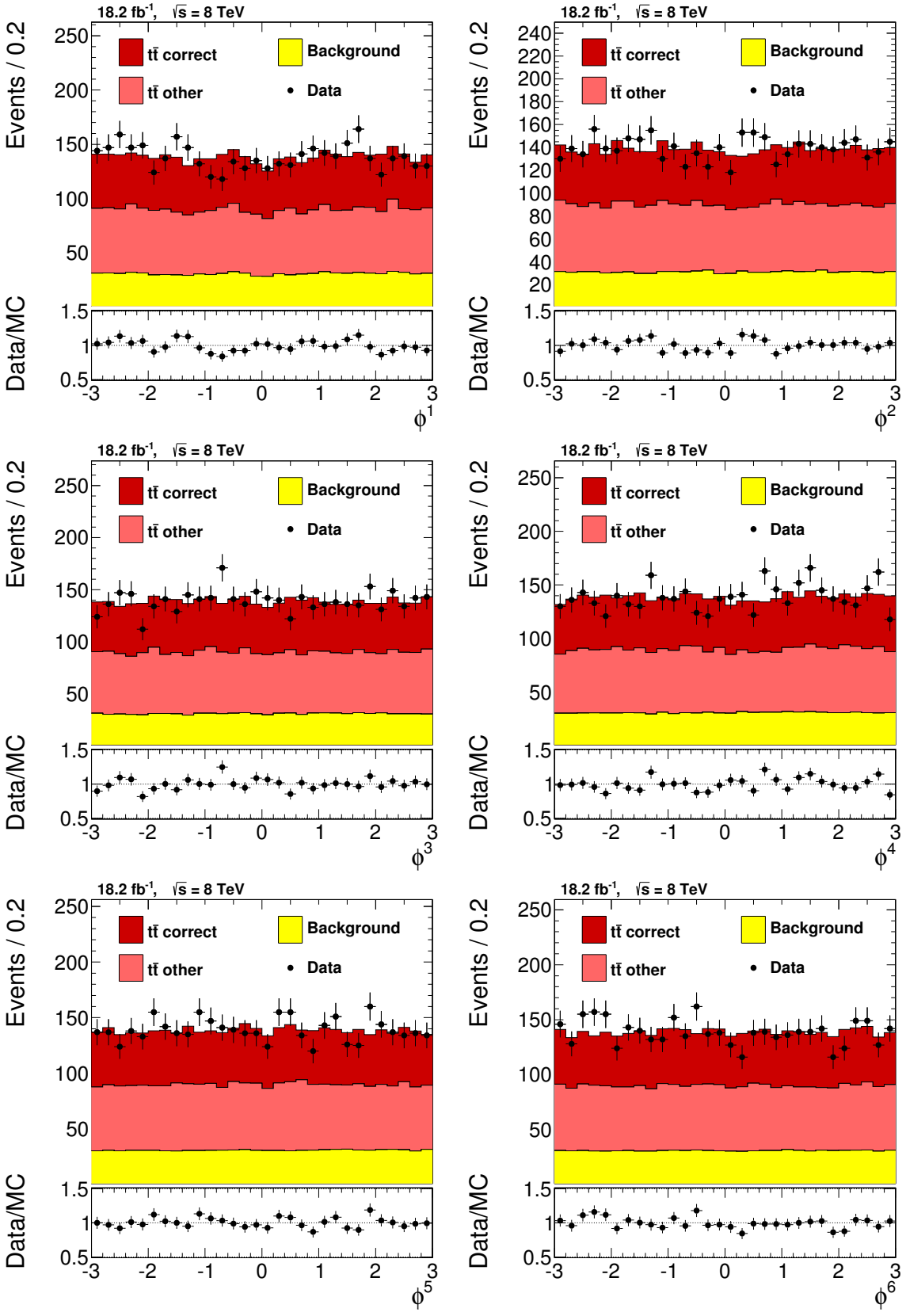

Figure 6.7: The azimuthal angles of the six leading jets.

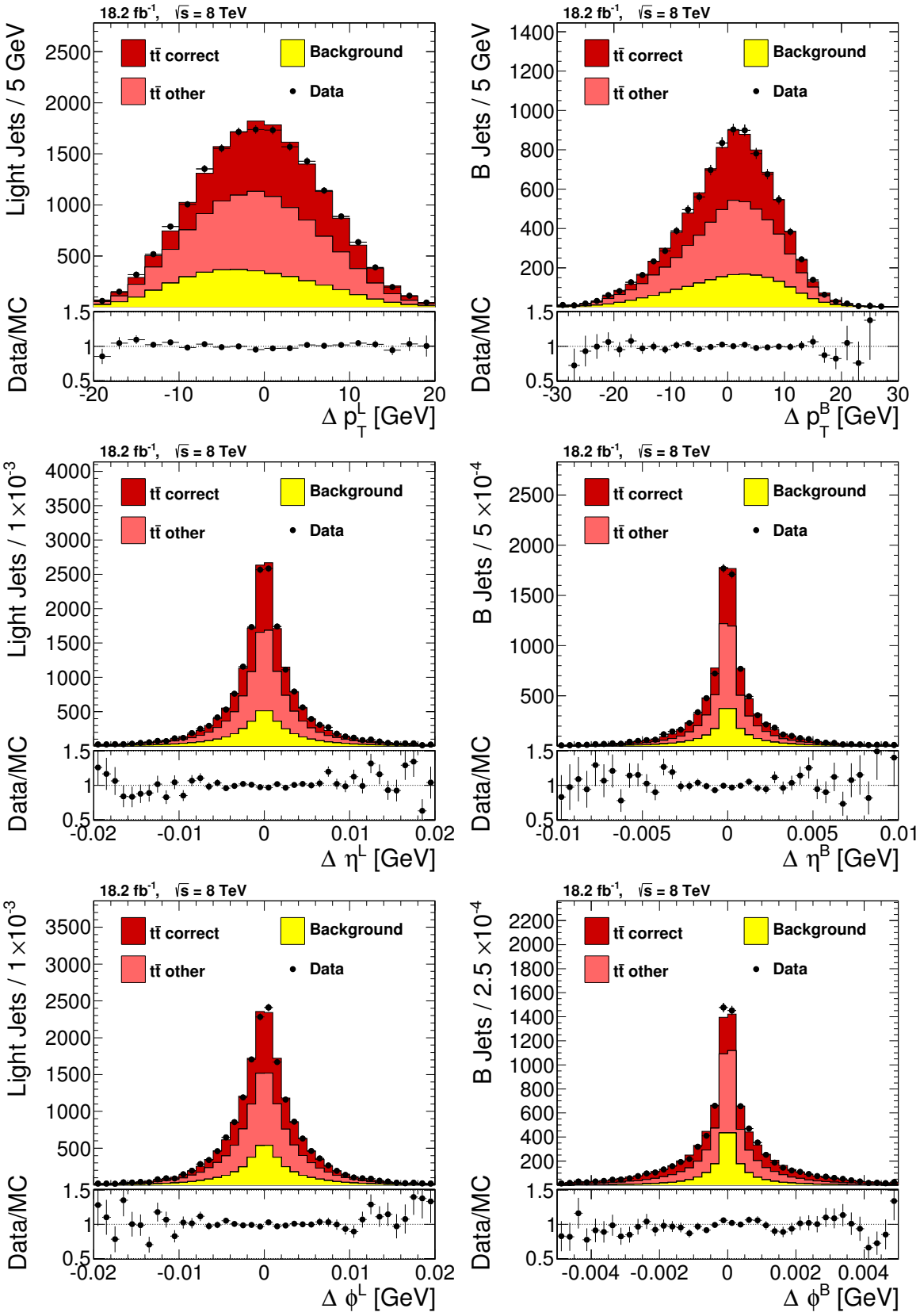

Figure 6.8: Shifts of the kinematic fit ($x^{\text{fit}} - x^{\text{reco}}$) for the light quark candidates (left) and bottom quark candidates (right). At the top, the shift in the transverse momentum, in the middle, the shift in the pseudorapidity, and at the bottom, the shifts in the azimuthal angle are shown, respectively.

The second interesting effect seen in this distribution is the fact that almost no correct permutations are found below a transverse momentum of 100 GeV for the top quarks from the kinematic fit. The reason for this effect is found in the selection criterion on the transverse momentum of the four leading jets to be above 60 GeV. This criterion mainly vetoes events with low transverse momenta for the top quarks. Nevertheless, in all studied selection scenarios the transverse momenta for correct permutations are on average higher compared to the other cases. At some point, this could be used to further increase the signal and correct permutation purities. In Figure 6.9 (bottom left), the transverse momentum of the top-quark pair system is depicted. This distribution is a good example of where the background estimation via event mixing, as described in section 6.3, fails completely. More details on the advantages and disadvantages of the event mixing technique are discussed in section 6.3. The rapidities of W bosons, top quarks, and the top-quark pair system are described well. At leading order, the rapidity of the top-quark pair system is given by:

$$y = \frac{1}{2} \ln \left(\frac{x_1}{x_2} \right) \tag{6.1}$$

Here, $x_{1/2}$ are the fraction of the proton energy of initial state partons. Thus, the rapidity of the top-quark pair system is sensitive to the PDFs (see section 2.2.1). As gluon-gluon fusion is the dominating production process for top-quark pairs at a centre-of-mass energy of 8 TeV, most of the sensitivity is found for the gluon distribution within the proton. The rapidity of the top quarks, as direct decay products of the top-quark pair system, are sensitive to the PDFs, too, but to a lesser extent. A good agreement of both distributions implies that the gluon distribution is modelled well in the simulated samples.

In Figure 6.10 (top), the top-quark masses before (left) and after (right) the kinematic fit are presented. The masses of both reconstructed top quarks are shown before the kinematic fitting, whereas only one mass per event is displayed after the kinematic fit, as one of the constraints in the kinematic fitting is the equality of the two top-quark masses. It is clearly visible that the width of the top-quark mass peak is decreasing with the kinematic fitting procedure. For correct permutations, the resolution on the top-quark mass improves from 14 GeV before to 7.9 GeV after the kinematic fit and, thus, almost doubles the precision. For both top-quark masses, before and after the kinematic fit, it can be seen that peak in data seems to be a bit broader compared to the prediction. This effect might originate in a worse jet energy resolution in data compared to the simulated sample. The possible effects of this are discussed later in section 6.9.

For the top-quark mass after the kinematic fit, the correct permutations are nicely peaking close to the expected top-quark mass, whereas the other permutations have only a small peak in this region. This peaking part of the other permutations might stem from correct assignments of ambiguous events, which therefore cannot be assigned to the correct permutations. The other permutations have an additional long tail to high top-quark masses. This tail originates from permutations that are missing at least one jet for the reconstruction (e.g. due to being out of acceptance, merging with another jet, or splitting into multiple jets) or being reconstructed wrongly. This latter fraction

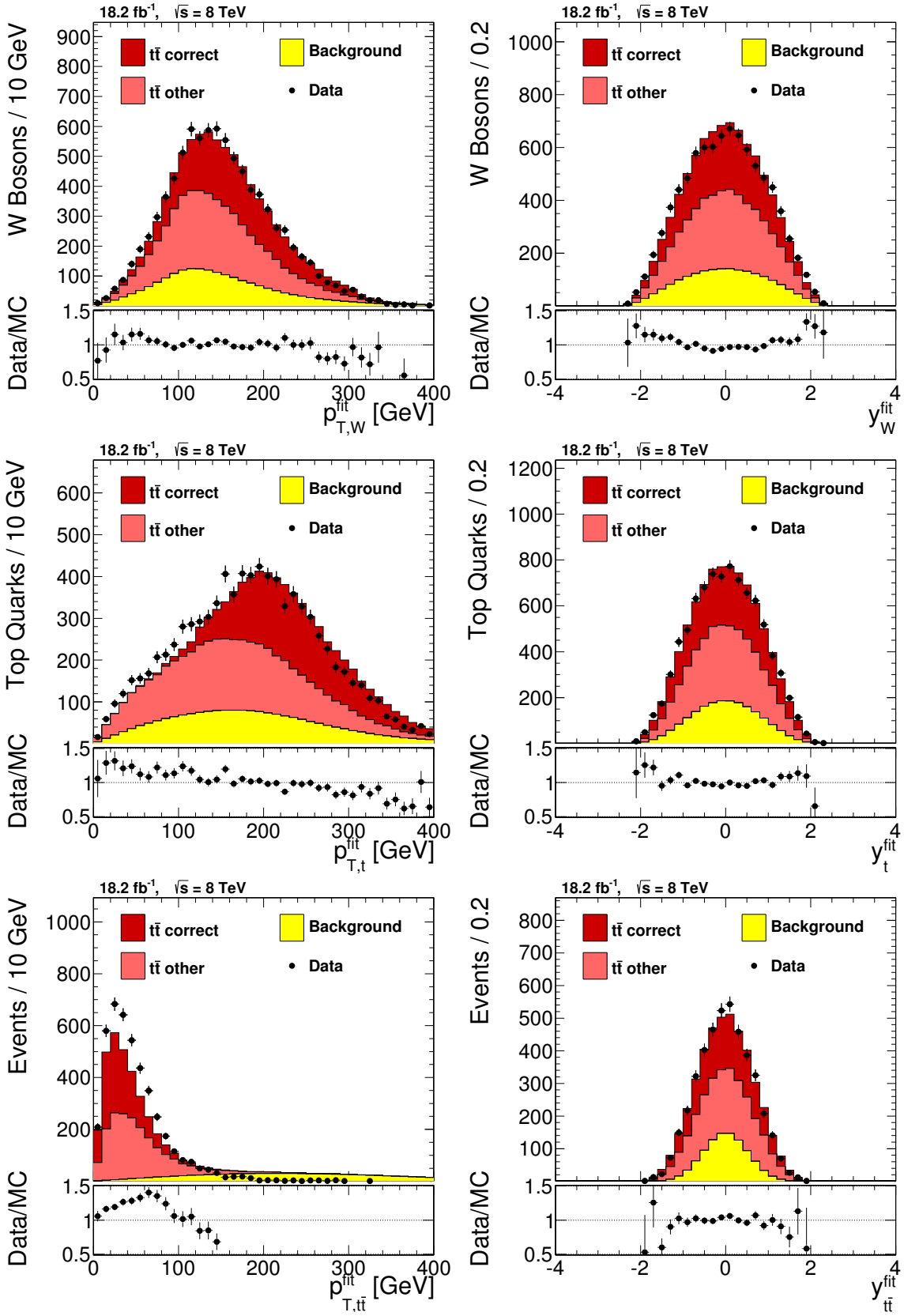

Figure 6.9: The transverse momenta (left) and rapidities (right) are shown for the fitted W-boson candidates (top), top-quark candidates (middle), and the top-quark pair system (bottom).

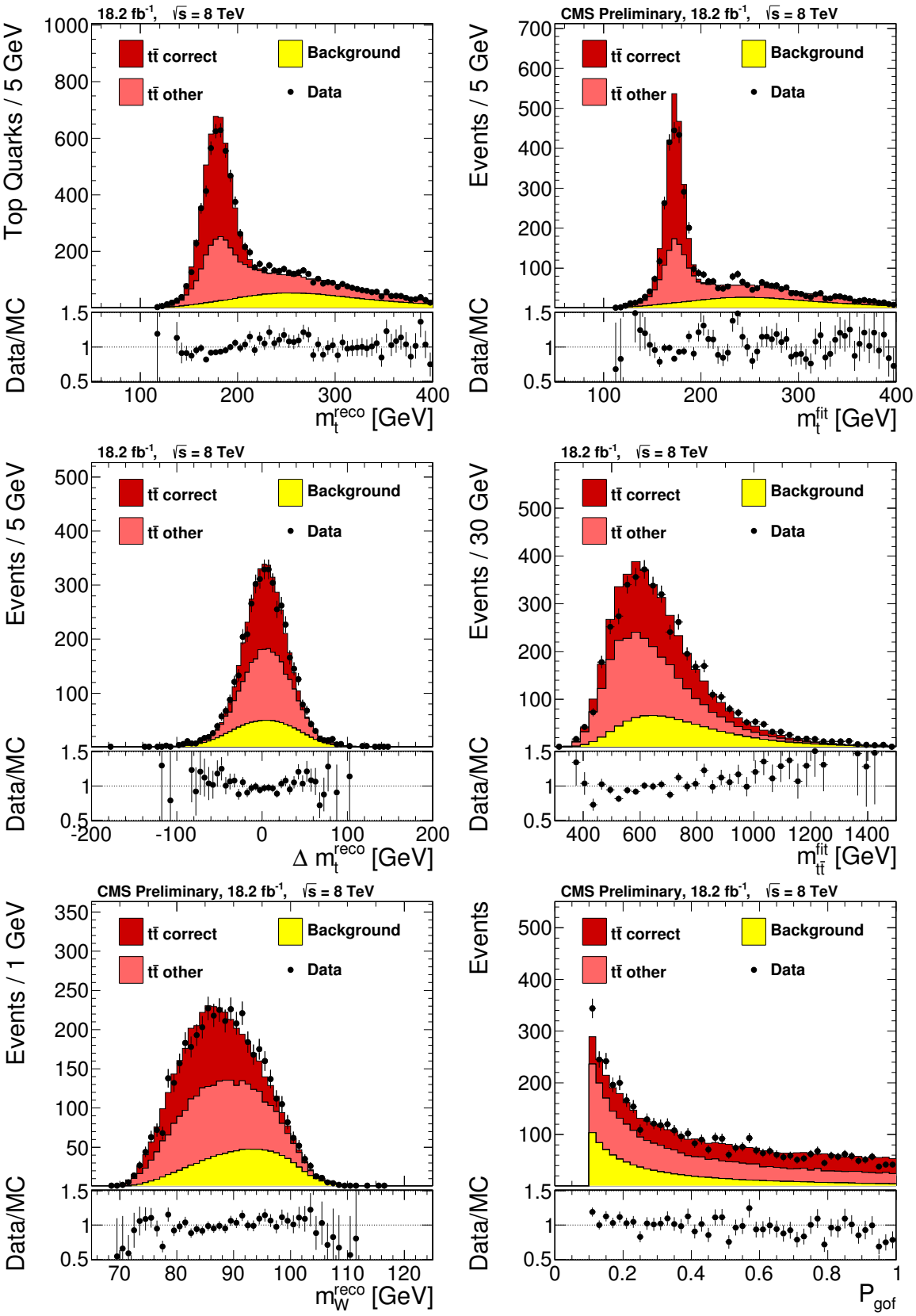

Figure 6.10: At the top, the top-quark masses before (left) and after (right) the kinematic fit are shown. At the middle left, one can see the difference of the two top-quark masses before the kinematic fit, while at the middle right, the invariant mass of the top-quark pair system is presented. At the bottom left, the reconstructed average W-boson mass and at the bottom right, the probability of the kinematic fit are displayed.

is low as mentioned in section 6.2. The background in the top-quark mass peak region is almost negligible and the 22% of background events after the selection are mainly found at higher masses.

In order to evaluate the kinematic fit constraint of the equality of the two top-quark masses, the difference of the two top-quark masses before the kinematic fit is depicted in Figure 6.10 (middle left). For correct permutations, the distribution has a width of 18 GeV, whereas for the other permutations a width of 28 GeV and for the background a width of 39 GeV are measured. This shows that the constraint of the equality of the two top-quark masses helps to distinguish correctly reconstructed top-quark pairs from all other cases and such improves the event reconstruction. In Figure 6.10 (middle right), the invariant mass of the top-quark pair system is presented. It is also well modelled by the prediction.

In Figure 6.10 (bottom left), the reconstructed average W-boson mass is shown. The peak position, even for correct permutations, is obviously shifted above the expected value of 80.4 GeV. There are two effects contributing to this shift. Firstly, the requirement of a minimal transverse momentum for the jets vetoes more events on the low side of the peak than on the high side. Secondly, the jet energy corrections used by CMS (see section 5.3.2) are derived from a sample of events with jets mainly originating from gluons. The response for jets originating from light quarks is slightly higher, thus these jets are overcorrected by about 1%. This distribution is directly sensitive to the jet energy scale, while not being sensitive to the top-quark mass giving the possibility for an in-situ measurement of the jet energy scale together with the top-quark mass. In the data over prediction ratio, a slight slope is visible, which will later on translate into the measurement of the jet energy scale factor.

In Figure 6.10 (bottom right), the probability of the kinematic fit is displayed. The correct permutations of the top-quark pair events are flat, as one would expect it if the investigated topology fulfils the constraints of the kinematic fit (as described in section 5.4). In contrast to the correct permutations, the remaining other permutations are falling with higher probabilities and the background is falling even steeper as the constraints from the kinematic fitting are not fulfilled. In order to increase the signal purity and the fraction of correctly reconstructed events, it would be possible to tighten the selection criterion on the probability even further at the cost of a decreased statistical precision.

In Figure 6.11, the distance between the two bottom-quark candidates from the kinematic fit is shown. It can be seen that it is flat for the background indicating that the background is purely combinatorial. For values above π, the distribution is steeply falling as a back-to-back like topology is reached. Larger distances can only be achieved by top-quark pair systems that are almost completely at rest when one top quark is detected in the positive and the other one in the negative pseudorapidity region of the detector.

All in all, a good agreement of the prediction with data is observed with some expected exceptions discussed throughout this section.

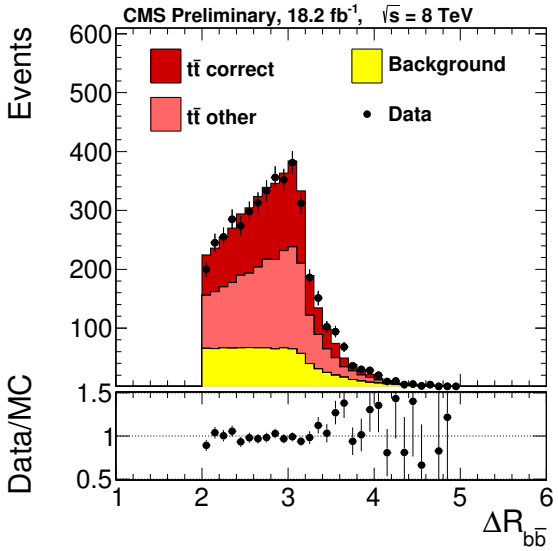

Figure 6.11: Distance between the two bottom-quark candidates from the kinematic fit.

6.5 Template Derivation

The templates for the signal likelihoods used in the ideogram are derived from simulated samples with generated top-quark masses of 166.5, 169.5, 171.5, 172.5, 173.5, 175.5, and 178.5 GeV. The jet energies in all these samples are scaled by factors of 0.96, 0.98, 1.00, 1.02, 1.04, respectively, to observe the effects of a shifted jet energy scale.

Each free parameter of the template distributions is parametrised by

$$C_0 + C_1 \times (m_\mathrm{t}/\,\mathrm{GeV} - 172.5) + C_2 \times (\mathrm{JSF} - 1) + \mathrm{C}_3 \times (\mathrm{m_t}/\,\mathrm{GeV} - 172.5) \times (\mathrm{JSF} - 1) \quad (6.2)$$

depending linearly on m_t, JSF, and the product of the two. The parameter C_0 is the mean value, C_1 and C_2 give the slope with respect to m_t and JSF, respectively, and C_3 denotes the correlation strength between m_t and JSF. In the following, the parameters will be labelled such that in the bracket:

1. the function type (Voigtian = V, Gaussian = G, or Landau = L),
2. the variable they are used as parametrisation for ($m_\mathrm{t}^\mathrm{fit}$ or $m_\mathrm{W}^\mathrm{reco}$),
3. the permutation type they are parametrising, and
4. an optional further distinction are given.

The template for the top-quark mass distribution for the correct permutation $P_\mathrm{CP}\left(m_\mathrm{t}^\mathrm{fit}|m_\mathrm{t}, \mathrm{JSF}\right)$ is assumed to be described by a Voigtian distribution. This is a convolution of a Gaussian with a Lorentz distribution. The mean $\mu(\mathrm{V}, m_\mathrm{t}^\mathrm{fit}, \mathrm{CP})$ and the width $\sigma(\mathrm{V}, m_\mathrm{t}^\mathrm{fit}, \mathrm{CP})$ of the Gaussian part are free parameters of the fit, while the width of the Lorentz part of the distribution is fixed to 2 GeV.

The top-quark mass distribution for the other permutations $P_\mathrm{OP}\left(m_\mathrm{t}^\mathrm{fit}|m_\mathrm{t}, \mathrm{JSF}\right)$ is fitted by the sum of a Gaussian and a Landau distribution. The free parameters of the fit are the mean $\mu(\mathrm{G}, m_\mathrm{t}^\mathrm{fit}, \mathrm{OP})$ and the width $\sigma(\mathrm{G}, m_\mathrm{t}^\mathrm{fit}, \mathrm{OP})$ of the Gaussian,

the most probable value $\mathrm{MPV}(\mathrm{L}, m_\mathrm{t}^\mathrm{fit}, \mathrm{OP})$ and the width $\sigma(\mathrm{L}, m_\mathrm{t}^\mathrm{fit}, \mathrm{OP})$ of the Landau distribution, and the relative normalisation of the two distributions. This normalisation is fitted by one common scale factor for all samples, without any dependence on m_t or JSF. It is found to be 70.1% for the Landau contribution, while the Gaussian makes up the remaining part.

The distributions for the reconstructed W-boson masses for correct permutations $P_\mathrm{CP}\left(m_\mathrm{W}^\mathrm{reco}|m_\mathrm{t}, \mathrm{JSF}\right)$ are fitted by asymmetric Gaussians. These asymmetric Gaussians have two different widths below and above, $\sigma(\mathrm{G}, m_\mathrm{W}^\mathrm{reco}, \mathrm{CP}, \mathrm{below})$ and $\sigma(\mathrm{G}, m_\mathrm{W}^\mathrm{reco}, \mathrm{CP}, \mathrm{above})$, respectively, the common mean $\mu(\mathrm{G}, m_\mathrm{W}^\mathrm{reco}, \mathrm{CP})$. All three parameters are free parameters to the fit.

The reconstructed W-boson masses for the other permutations $P_\mathrm{OP}\left(m_\mathrm{W}^\mathrm{reco}|m_\mathrm{t}, \mathrm{JSF}\right)$ are fitted with the sum of three Gaussians. Their mean values are separated by 7.5 GeV, the left and right Gaussians each make up 25% of the integral, the remaining 50% are taken by the central Gaussian. One mean value $\mu(\mathrm{G}, m_\mathrm{W}^\mathrm{reco}, \mathrm{OP})$ and three independent widths $\sigma(\mathrm{G}, m_\mathrm{W}^\mathrm{reco}, \mathrm{OP}, \mathrm{below})$, $\sigma(\mathrm{G}, m_\mathrm{W}^\mathrm{reco}, \mathrm{OP}, \mathrm{central})$, and $\sigma(\mathrm{G}, m_\mathrm{W}^\mathrm{reco}, \mathrm{OP}, \mathrm{above})$ are free parameters of the fit. An overview of the parameters for the signal templates can be found in Table 6.2. The templates for the signals are shown in Figures 6.12 and 6.13.

Parameter	C_0	C_1	C_2	C_3
$\mu(\mathrm{V}, m_\mathrm{t}^\mathrm{fit}, \mathrm{CP})$	172.399	0.989846	81.2246	0.758309
$\sigma(\mathrm{V}, m_\mathrm{t}^\mathrm{fit}, \mathrm{CP})$	7.92649	0.0730215	5.03184	0.0240931
$\mu(\mathrm{G}, m_\mathrm{t}^\mathrm{fit}, \mathrm{OP})$	173.325	1.11062	80.0103	1.32946
$\sigma(\mathrm{G}, m_\mathrm{t}^\mathrm{fit}, \mathrm{OP})$	10.0153	0.0656919	−4.72943	−0.108363
$\mathrm{MPV}(\mathrm{L}, m_\mathrm{t}^\mathrm{fit}, \mathrm{OP})$	190.009	0.231141	123.727	−2.40988
$\sigma(\mathrm{L}, m_\mathrm{t}^\mathrm{fit}, \mathrm{OP})$	26.2830	−0.0172414	35.011	−0.441827
$\mu(\mathrm{G}, m_\mathrm{W}^\mathrm{reco}, \mathrm{CP})$	84.4536	−0.015491	91.1498	−0.0091983
$\sigma(\mathrm{G}, m_\mathrm{W}^\mathrm{reco}, \mathrm{CP}, \mathrm{below})$	5.20735	−0.0115874	23.4645	−0.0248959
$\sigma(\mathrm{G}, m_\mathrm{W}^\mathrm{reco}, \mathrm{CP}, \mathrm{above})$	6.75627	0.00193015	−19.8346	0.0722259
$\mu(\mathrm{G}, m_\mathrm{W}^\mathrm{reco}, \mathrm{OP})$	87.8575	−0.00612002	23.2629	−0.0796552
$\sigma(\mathrm{G}, m_\mathrm{W}^\mathrm{reco}, \mathrm{OP}, \mathrm{below})$	3.97727	0.00218234	3.87521	−0.126504
$\sigma(\mathrm{G}, m_\mathrm{W}^\mathrm{reco}, \mathrm{OP}, \mathrm{central})$	4.91878	0.000522822	−12.4336	−0.0848389
$\sigma(\mathrm{G}, m_\mathrm{W}^\mathrm{reco}, \mathrm{OP}, \mathrm{above})$	4.68122	0.0118212	−13.8506	0.145685

Table 6.2: Overview of the parameters used for the signal templates. The parameter C_0 is the mean value, C_1 and C_2 give the slope with respect to m_t and JSF, respectively, and C_3 denotes the correlation strength between m_t and JSF.

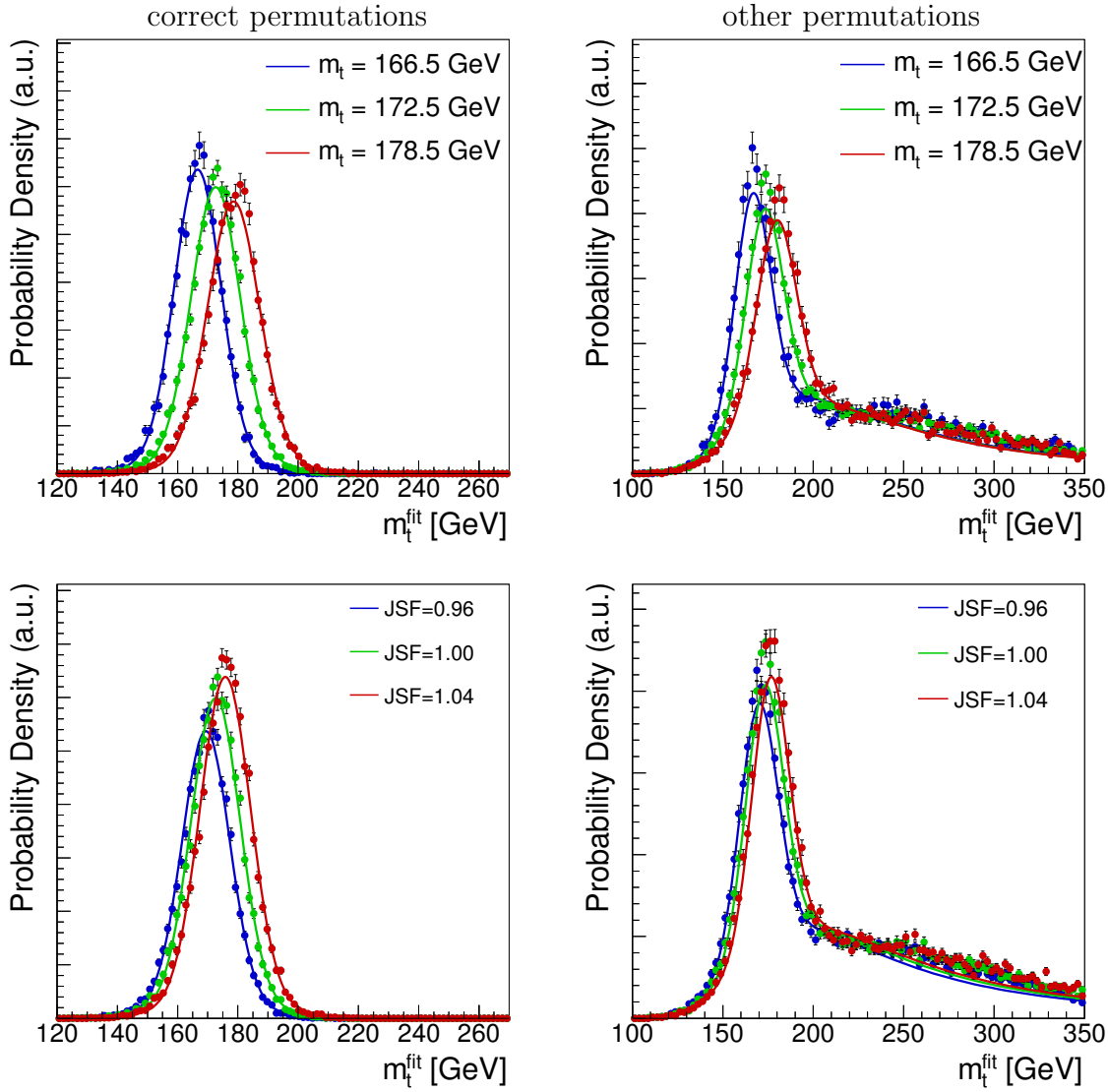

Figure 6.12: Templates for top-quark mass distributions. On the left (right), the correct (other) permutations are shown.

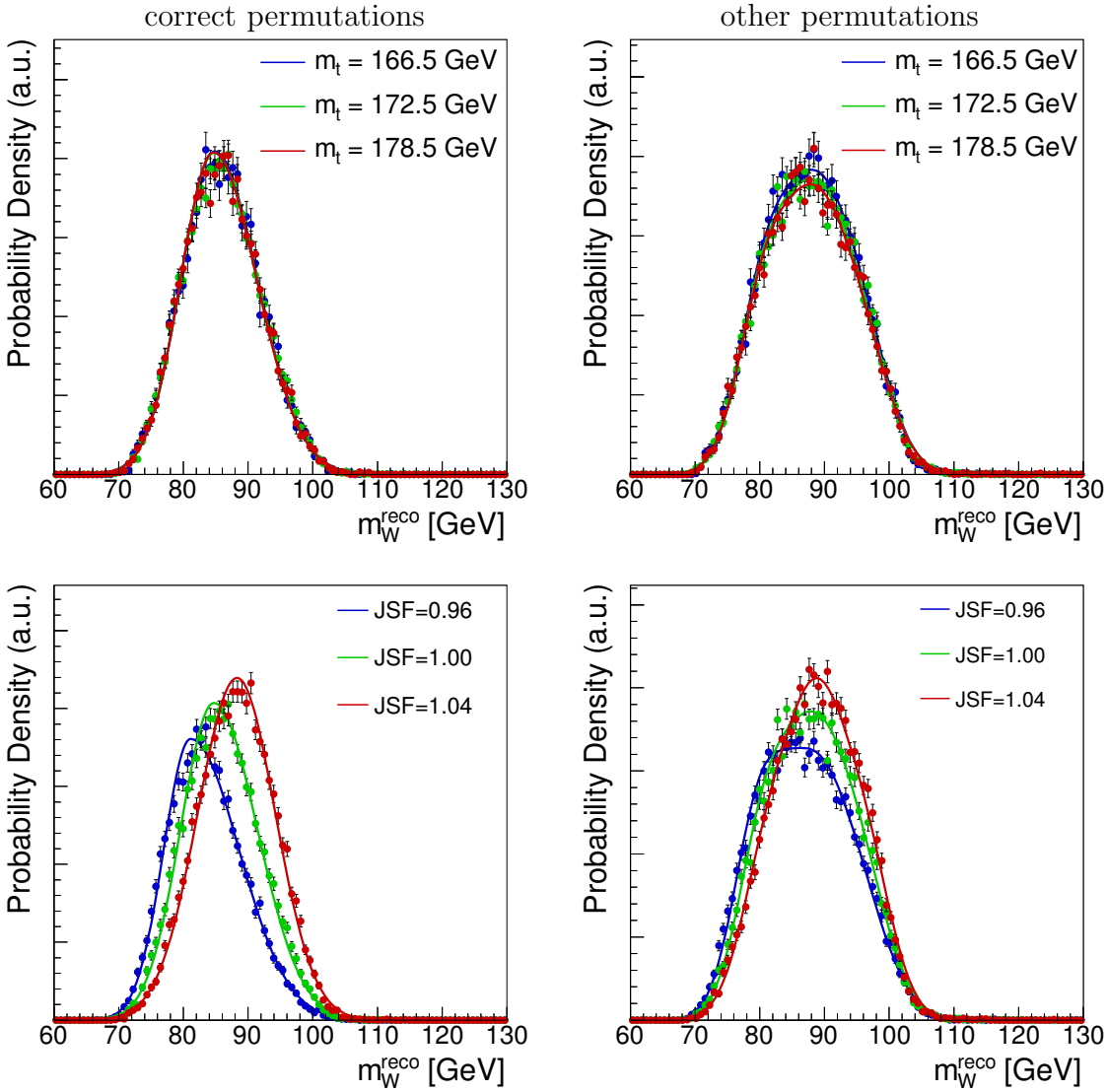

Figure 6.13: Templates for W-boson mass distributions. On the left (right), the correct (other) permutations are shown.

For the background in the top-quark mass distribution $P_{\text{bkg}}\left(m_{\text{t}}^{\text{fit}}\right)$, the sum of a Gamma distribution:

$$f(m_{\text{t}}^{\text{fit}}) = \frac{\left(\frac{m_{\text{t}}^{\text{fit}}-\mu}{\beta}\right)^{\gamma-1} \exp\left(-\frac{m_{\text{t}}^{\text{fit}}-\mu}{\beta}\right)}{\beta\Gamma(\gamma)} \quad \text{with} \quad \Gamma(a) = \int_0^\infty t^{a-1}e^{-t}\,dt \tag{6.3}$$

and a Landau is used. The parameter μ defines the starting point, β defines the width of the distribution, and γ the shape of the distribution. The two distributions are normalised such that the Gamma distribution makes up 60.6% of the integral, while the Landau part makes up the remaining part. The reconstructed W-boson mass $P_{\text{bkg}}\left(m_{\text{W}}^{\text{reco}}\right)$ is fitted with an asymmetric Gaussian, like for the correct permutations in the signal. An overview of the parameters for the background can be found in Table 6.3 and a visualisation in Figure 6.14. For parametrisation of the reconstructed W-boson mass from the background a slight discrepancy is observed. This effect is corrected for in the calibration (see section 6.7).

Function	Parameters		
Gamma	$\gamma = 5.79618$	$\mu = 120$	$\beta = 27.8151$
Landau	MPV $= 199.835$	$\sigma = 37.6189$	
Gaussian	$\mu = 92.1358$	$\sigma(\text{below}) = 8.04982$	$\sigma(\text{above}) = 7.0838$

Table 6.3: Overview of the parameters used for the background templates.

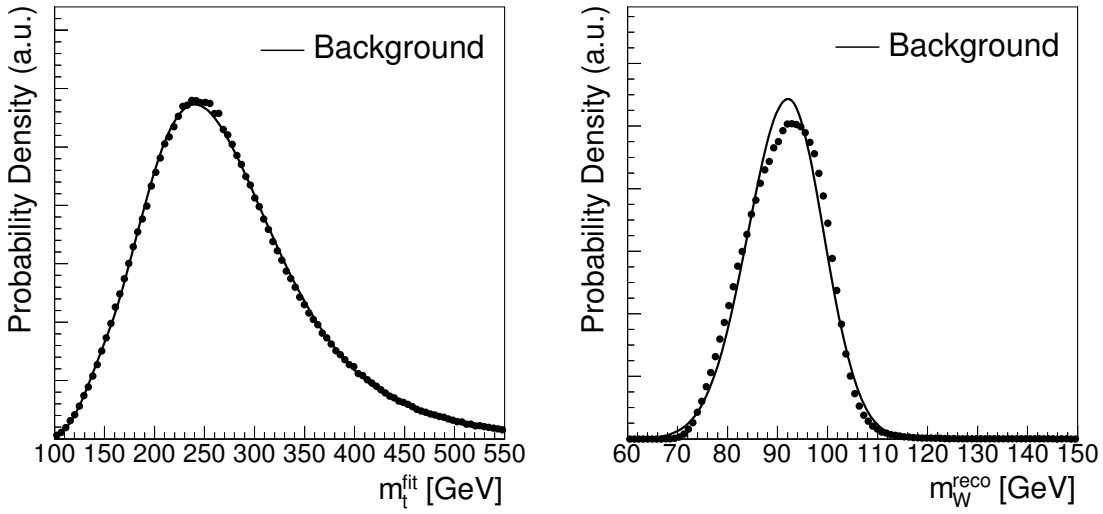

Figure 6.14: Templates for the background distributions. On the left, the template for the top-quark mass and, on the right, the template for the W-boson mass are shown.

6.6 Analysis Code

The analysis code used for this analysis is based on `ROOT`. It is optimised for flexibility and processing time. Thus, the analysis code is divided into three main parts:

- Reading data from disc and putting it into memory
- Selecting events for the later full analysis
- Calculating the top-quark mass from a set of events

The first step, reading data from disc, is implemented using `TTreeFormulas` [97]. Via this very flexible method, it is possible to put any kind of `TTree` into the analysis. All required variables are saved in memory as plain `double` or `int`. This ensures a very fast access, as the file on disc is not needed anymore after initial reading of all information.

As second step, the events that should be analysed are selected. This has to be as fast as possible as many pseudo experiments need to be done for the calibration of the measurement (see section 6.7) and the derivation of the systematic uncertainties (see section 6.8). As all relevant objects were copied to memory in the previous step, this is extremely fast (below one second).

In the last step, the top-quark mass and possible further parameters are extracted from this set of events. Therefore, the negative logarithmic likelihood functions for all events are given to the `ROOT::Math::Minimizer` [98] to find the optimal value of the free parameters. These likelihood parametrisations (see section 6.5) are hard-coded into the analysis code to reach a reasonable calculation speed. However, the parameters of the likelihoods are once read from a configuration file at the beginning of the execution to be flexible in changing them. In order to speed up the calculations, all integrals needed during the minimisation process are calculated only once and are cached. The optimal values are derived for all free parameters individually and for any combination of them. Currently, there are four possible free parameters (m_{t}, JSF, f_{sig}, and f_{CP}) making up in total 32 minimisations taking about four seconds.

After having read all data once, the program needs less than five seconds to derive a full set of parameters including eight different calculations of the top-quark mass.

6.7 Calibration

In order to account for possible biases in the measurement, it has to be calibrated. This calibration is performed using pseudo experiments. At each point in a plane spanned by m_{t} and JSF, at least 10 000 pseudo experiments are conducted, corresponding to the integrated luminosity in data of $18.2\,\mathrm{fb}^{-1}$. A small bias due to a non-perfect description of the distributions by the template functions is expected. Biases for m_{t} and JSF are defined as:

$$\begin{aligned} \text{mass bias} &= \left\langle m_{\mathrm{t,ext}} - m_{\mathrm{t,gen}} \right\rangle \\ \text{JSF bias} &= \left\langle \mathrm{JSF}_{\mathrm{ext}} - \mathrm{JSF} \right\rangle \end{aligned}$$

The extracted top-quark mass for one set of pseudo experiments in shown in Figure 6.15. This set of pseudo experiments is conducted for the central calibration point ($m_{\mathrm{t,gen}} = 172.5\,\mathrm{GeV}$ and JSF = 1). Like for this example, all extracted quantities are approximated very well by a Gaussian, thus it is well justified to extract the bias by fitting a Gaussian to the results of the pseudo experiments. The mean value of the Gaussian is used as extracted value for this sample of pseudo experiments and the width of the Gaussian is used as its uncertainty.

The results of the calibration can be found in Figure 6.16. Small biases are observed for both m_{t} and JSF. The main reason for this bias is the non-perfect description of the W-boson mass template for the multijet background (see Figure 6.14 (right)). A better description of this distribution would probability reduce the biases in the calibration, but would not change the result after the calibration. For each generated JSF value, the biases are fitted with a linear function. From these fits, calibration constants are derived as functions depending linearly on m_{t}, JSF, and the product of the two, like the template parameters (6.2). They can be found in Table 6.4. After applying this calibration, all biases in the measured values of m_{t} and JSF vanish.

Afterwards, the pull width is checked to see whether the estimated statistical uncertainties are correct. The pull is defined as:

$$\text{pull} = \frac{m_{\mathrm{t,cal}} - m_{\mathrm{t,gen}}}{\sigma\left(m_{\mathrm{t,cal}}\right)} \tag{6.4}$$

The statistical uncertainty for the top-quark mass is slightly underestimated by 2.2%, as visible in Figure 6.17 (left). This effect is corrected for in the measurement by dividing $-2\ln\mathcal{L}$ by the square of the pull width found for m_{t}. The pull width of JSF is slightly overcorrected, yet being compatible with unity with its uncertainties, as can be seen in Figure 6.17 (right).

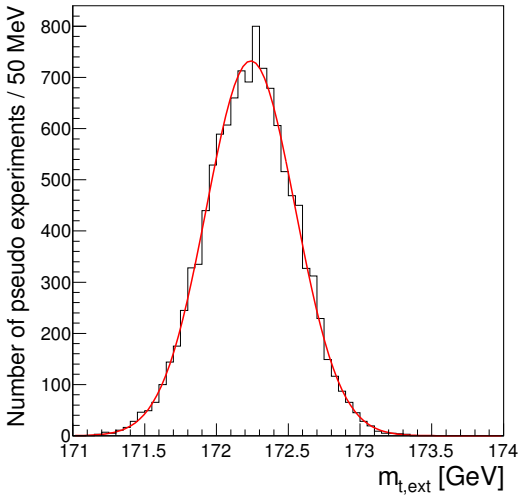

Figure 6.15: One example set of pseudo experiments shown for the central calibration point ($m_{\mathrm{t,gen}} = 172.5\,\mathrm{GeV}$ and JSF = 1) used in the calibration. A Gaussian is fitted to set of pseudo experiments. The mean value of the Gaussian is used as extracted mass of this set of pseudo experiments while the width is used as uncertainty.

Parameter	C_0	C_1	C_2	C_3
m_{t}	1.15932×10^{1}	-4.31538×10^{-3}	-3.70669	-1.52610×10^{-2}
JSF	-4.48210×10^{-4}	4.57904×10^{-5}	3.96438×10^{-2}	-1.75466×10^{-4}

Table 6.4: Overview of the calibration constants. The parameter C_0 is the offset, C_1 and C_2 give the slope with respect to m_{t} and JSF, respectively, and C_3 denotes the correlation strength between top-quark mass and JSF.

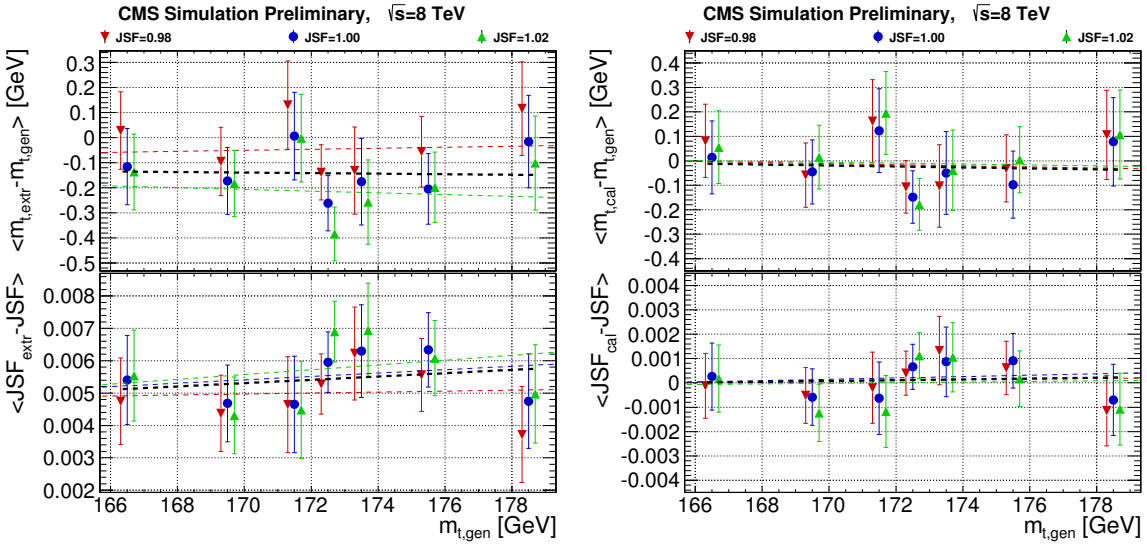

Figure 6.16: On the left, the biases in measured m_t and JSF are shown. After applying the calibration the bias in both measurements is gone as can be seen on the right.

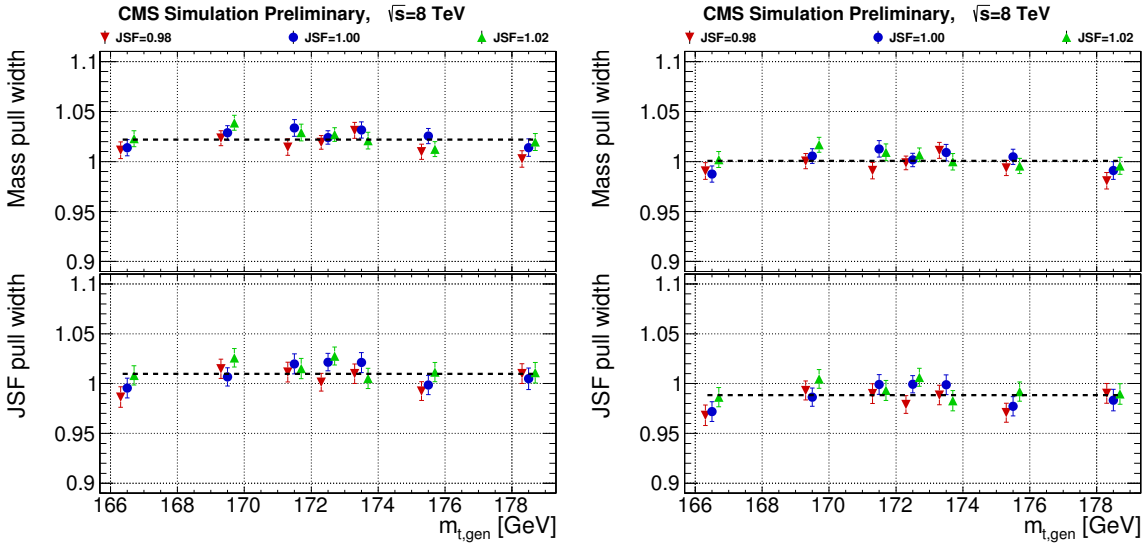

Figure 6.17: The pull widths for top-quark mass and JSF are shown. On the left, it can be seen that the pull width for the top-quark mass is 2.2% above unity. The statistical uncertainty is corrected for this effect. On the right, one can see that this correction works as expected for m_t. The pull width for JSF seems slightly overcorrected, but is compatible with unity within its uncertainties.

6.8 Systematic Uncertainties

Systematic uncertainties are derived using pseudo experiments. For each systematic variation, at least 10 000 pseudo experiments are conducted, each corresponding to the integrated luminosity in data of $18.2\,\mathrm{fb}^{-1}$. In the case of multiple variations (e.g. up and down) for one systematic uncertainty source, the largest observed shift is taken as uncertainty. If the statistical precision on a systematic uncertainty is worse than the observed shift itself, the statistical precision is taken as uncertainty. Two different evaluation of the top-quark mass are taken into account here:

- The jet energy scale factor JSF as free parameter in the minimisation
- The jet energy scale factor JSF fixed to one, i.e. using the default CMS JES

Henceforth, these approaches are called 2D and 1D results, respectively. The parameters for the fraction of signal events and correct permutations, f_{sig} and f_{CP}, respectively, are free in both minimisation processes. In the following, the sources of possible systematic uncertainties on the measurement that are taken into account for this measurement are listed. In Table 6.5, the overview of all systematic uncertainties can be found.

6.8.1 Calibration

The statistical uncertainty on the calibration is propagated to the measured variables. In addition, the maximum difference of the calibrations at different JSF is added in quadrature to take into account non-linear effects of the calibration.

6.8.2 Jet Energy Scale

All jets are shifted up and down by their uncertainties [74, 75]. The uncertainty is split into multiple categories to facilitate the combination with other top-quark mass measurements. Details on the splitting of the uncertainty on the jet energy scale are described in section 5.3.3.

6.8.3 Jet Energy Resolution

As described in section 5.3.4, the jet energy resolution in the simulated sample is worsened, depending on the pseudorapidity of the jet, by 7-20% to match the resolutions found in data [74]. To account for its uncertainties, it is varied within its measured uncertainties up and down by one standard deviation.

6.8.4 B Tagging

The p_{T}-dependent b-tag efficiencies and misidentification rates are scaled up and down by their uncertainties [78].

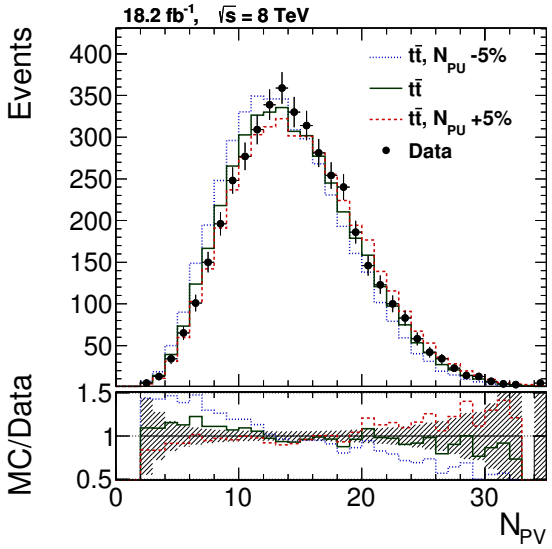

Figure 6.18: The number of primary vertices is shown. The solid green line is the simulated sample. As dotted blue (dashed red) line the systematic variation of the number of pileup interactions by -5% (+5%) is shown. The hatched band in the ratio visualises the statistical uncertainty from data. The simulated top-quark pair sample is normalised to data.

6.8.5 Pileup

The average number of pileup events is varied to account for the uncertainties associated with the determination of the number of pileup events and the weighting procedure, which weights the simulated sample according to the expected distribution from data. This variation is done by increasing (decreasing) the total pp cross section for the extraction of the average number of pileup events by $\pm 5\%$ [99]. In Figure 6.18, the distribution of primary vertices is shown for the simulated signal sample and the systematic variations. A good agreement within the uncertainties is observed.

In addition, as pileup affects the measured jet energies, too, the jet energies are scaled by an uncertainty covering the difference between a flat and a p_{T}-dependent jet energy correction for pileup. These two uncertainties are added in quadrature.

6.8.6 Trigger

In order to account for possible biases due to the requirement on the transverse momentum of the fourth calorimeter-based jet for reaching the plateau of the trigger efficiency, the transverse momenta of the calorimeter-based jets are varied. The requirement that the fourth jet should be above 60 GeV is shifted by the full jet energy scale uncertainty for calorimeter-based jets [74, 75]. These uncertainties are of the order of 12-15% around 60 GeV.

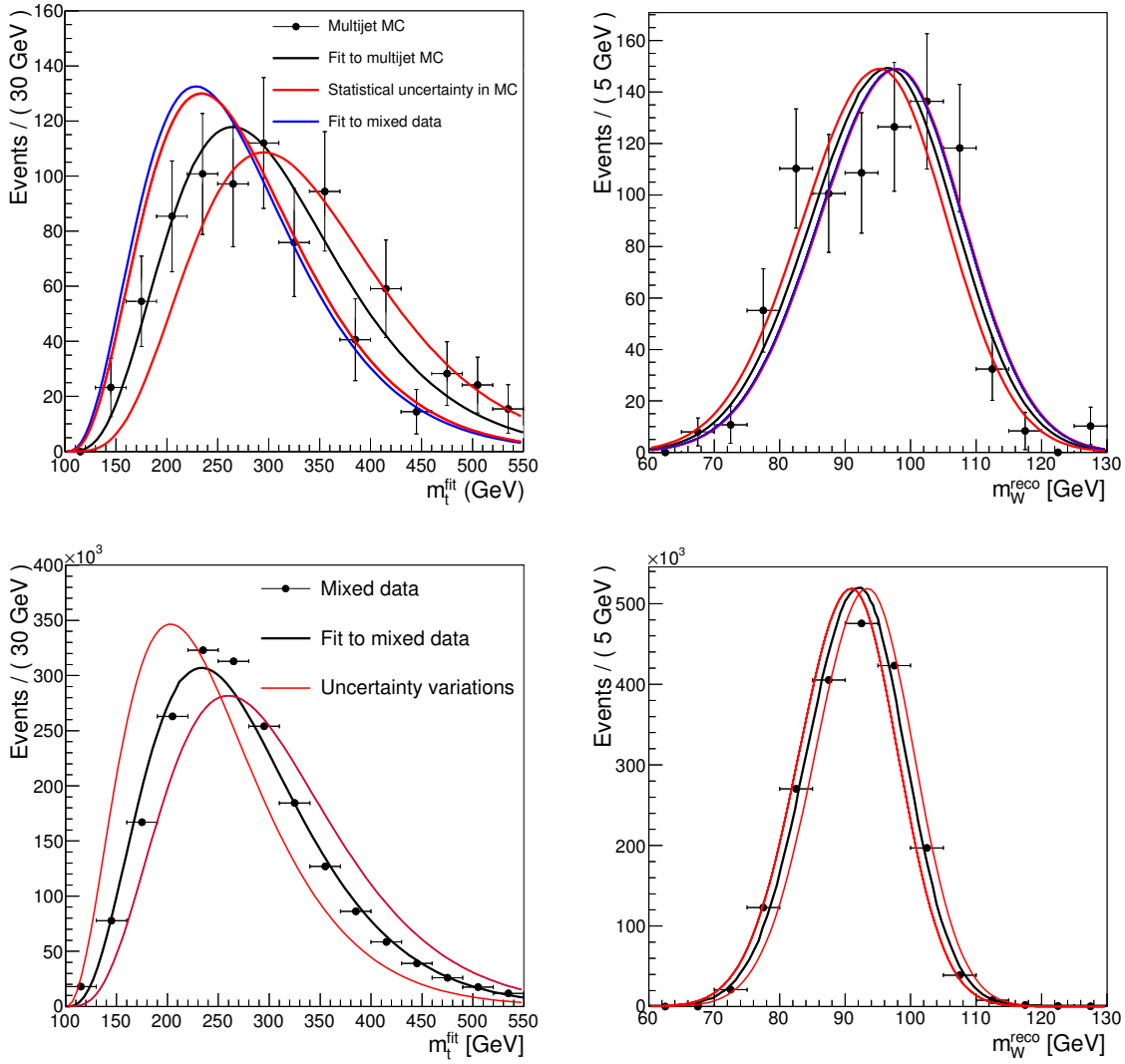

Figure 6.19: On the left, the top-quark mass distribution from the kinematic fit and, on the right, the reconstructed average W-boson mass are shown. In the top row, the fit to the simulated multijet events with the loose selection is coloured black. The templates for the relative uncertainties are shown as red lines and the fit to the data-driven background as blue line, respectively. In the bottom row, the fit to the data-driven background in the signal region is coloured black. The templates with the full uncertainty on the main parameters (maximum of the statistical uncertainty on the fit in the simulated multijet sample and the difference between data-driven background and simulated multijet sample with the loose selection) are shown as red lines.

6.8.7 Multijet Background

The uncertainty on the multijet background is split into two parts. The first part is the limited knowledge of the yield. As the background is scaled such that it gives the difference in number of events expected from the simulated top-quark pair sample and data, the uncertainty here stems from the limited knowledge of the number of events from top-quark pairs. The combination of the uncertainty on the NNLO production

cross section and the luminosity measurement give ±15% variations of the fraction of background events. Thus, the fraction of background events is varied around its central value of 22% to 19% and 25%.

The second effect is the uncertainty on the shape of the background distributions. In section 6.3, it is shown that the background estimate works well yielding only some small deviations as can be seen in Figure 6.4. Simulated multijet samples are used to get an estimate for the precision on the knowledge of the shape. To get a reasonable amount of events in the signal region for the simulated multijet sample, the selection criteria are loosened to $P\left(\chi^2\right) > 0.01$ and $p_{\mathrm{T}}(4^{\mathrm{th}}\ \mathrm{Jet}) > 50\,\mathrm{GeV}$. With this loose selection, the simulated multijet sample is compared to the data-driven background using the same selection. The maximum of the statistical uncertainty on the main template parameters from the simulated multijet sample and the difference of these parameters between the simulated multijet sample and the data-driven background are used as relative uncertainty. The resulting distributions can be found in Figure 6.19 (top). Corresponding shifts of the parameters are then applied to the templates in the signal region, as shown in Figure 6.19 (bottom). For the top-quark mass distribution, these variations are visualised in Figure 6.20 in comparison with the small deviations from Figure 6.4. Comparing the reconstructed average W-boson mass, a statistical uncertainty on the mean value of 1.34% is observed. The difference to the background from event mixing in data is 1.19%, whereas the small deviation in Figure 6.4 is only 0.63%.

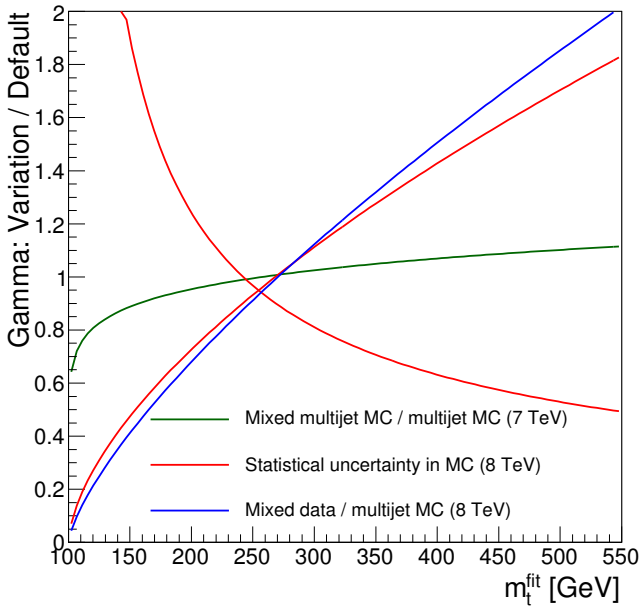

Figure 6.20: Relative differences of the top-quark mass distribution from the kinematic fit comparing the mixed data with the loose selection applied to the corresponding simulated multijet sample (blue line), the variations within the statistical uncertainty of the simulated multijet sample (red lines), and the small deviations observed in Figure 6.4 (green line).

6.8.8 Flavour Jet Energy Response

The uncertainty on the modelling of hadronisation is taken into account by varying the jet energies according to the response difference observed between PYTHIA and HERWIG++ with respect to a Z+jets flavour mixture for transverse momenta of jets of 200 GeV. This is done individually for jets originating from bottom quarks, light quarks, and gluons. These uncertainties are added in quadrature.

In addition, a comparison of simulated samples generated with POWHEG +PYTHIA and MC@NLO +HERWIG is done. This difference is smaller than the flavour response uncertainties as described above. The alternative comparison is done using POWHEG and MC@NLO, as both generators feature NLO calculations leaving the main difference in the hadronisation models of PYTHIA and HERWIG. Thus, this difference is assumed to be covered already.

6.8.9 Bottom Jet Energy Scale

Two effects modifying the jet energy scale of bottom quark induced jets are taken into account. Firstly, the fragmentation function of the B hadrons in the simulated samples is tuned to reproduce the measurements by ALEPH [100] and DELPHI [101] of the fraction of the B-hadron energy from the beam energy. The difference between the tuned and the default PYTHIA Z2* tune is taken as uncertainty as it is well above the uncertainty on the tuning itself.

The second effect taken into account is the semi-leptonic branching fraction of B hadrons. To include the measured uncertainties on both B^0 and B^+ [15], this fraction is varied by -0.45% and $+0.77\%$.

6.8.10 Parton Distribution Functions

The CTEQ 6.6L parton distribution functions (PDFs) [54] are used for generating the simulated events. The PDF4LHC prescription [102] is used for the calculation of the uncertainty associated to the choice of the PDF. An envelope of CT10 [103], MSTW2008 [104], and NNPDF 2.3 [105], including their PDF and α_S uncertainties, is created and the maximum difference between CTEQ 6.6L and the lower or upper edge of the envelope is taken as uncertainty.

6.8.11 Q^2 Scale

The hard scattering and parton showering scales chosen for the calculation of the strong coupling in the simulated sample are varied by factors of 0.5 and 2.0. This includes the uncertainty on initial- and final-state radiation.

6.8.12 ME-PS Matching Thresholds

The matching threshold for interfacing the matrix element from MadGraph to the parton shower from pythia is varied to 10 GeV and 40 GeV, respectively, around the default value of 20 GeV.

6.8.13 ME Generator

In order to take into account the effect of using a different generator for the matrix element, powheg is used to generate signal events. It is interfaced to pythia with the same Z2* tune as for the MadGraph sample. The powheg matrix element generator does a next-to-leading order calculation opposed to the leading order calculation of MadGraph and so includes one further final state parton in addition to the top-quark pair.

CMS measurements [92–95] show differences in the modelling of the transverse momentum spectrum of top quarks in pair production. In order to account for a possible systematic effect, the simulated sample is weighted to match top-quark transverse momentum distribution observed in data.

6.8.14 Underlying Event

The effect of multiple parton interactions is evaluated by changing the tuning of pythia. Two tunes with increased and decreased underlying event activity are compared to a central one, which is tuned to measurements [58]. The compared tunes are the Perugia 2011 tune as central point, the Perugia 2011 mpiHi tune with increased activity, and the Perugia 2011 Tevatron tune with decreased activity [106].

6.8.15 Colour Reconnection

For the evaluation of the effect of colour reconnection [107], two pythia tunes, one with and one without colour reconnection, are compared. The two tunes are the Perugia 2011 tune having colour reconnection enabled and the Perugia 2011 NoCR tune with colour reconnection being disabled [106].

			$\delta^{\text{2D}}_{m_\text{t}}$ (GeV)	δ_JSF	$\delta^{\text{1D}}_{m_\text{t}}$ (GeV)
Experimental uncertainties					
Calibration			0.06	< 0.001	0.06
JES	Flavour		0.11	0.002	0.59
	InterCalibration		< 0.01	< 0.001	0.02
	MPFInSitu		0.01	0.001	0.28
	Uncorrelated		0.11	0.002	0.55
	p_T-dependent residual		0.23	0.005	0.11
Jet energy resolution			0.10	0.001	0.01
b-tagging	rate		0.02	< 0.001	0.01
	mistag rate		0.01	< 0.001	0.01
Pileup	pp cross section		0.09	0.001	0.01
	JES		0.30	0.001	0.30
Trigger			0.18	0.003	0.07
Multijet background	f_sig		0.02	< 0.001	0.01
	shape		0.22	0.002	0.08
Modelling of hadronisation					
Jet energy response		bottom	0.29	< 0.001	0.30
		gluon	0.16	0.003	0.04
		udsc	0.14	0.002	0.01
bJES	Semi-leptonic B hadron decays		0.12	< 0.001	0.12
	b fragmentation		0.07	0.001	0.03
Modelling of the hard scattering process					
PDF			0.02	< 0.001	0.01
Q^2 scale			0.19±0.19	0.004±0.002	0.18±0.14
ME-PS matching threshold			0.20±0.19	0.002±0.002	0.09±0.14
ME generator	MadGraph vs. powheg		0.05±0.21	0.003±0.002	0.16±0.15
	top-p_T modelling		0.08	< 0.001	0.06
Modelling of the non-perturbative QCD					
Underlying event			0.13±0.28	0.000±0.002	0.11±0.20
Colour reconnection			0.00±0.25	0.000±0.002	0.03±0.18
Total			0.83	0.011	1.05

Table 6.5: Overview of systematic uncertainties. For some uncertainties in the categories of modelling of the hard scattering process and modelling of the non-perturbative QCD, the size of the simulated samples is statistically limiting the extraction of the systematic shift, thus, the statistical precision on the systematic shift is given for these uncertainties. The total is defined by adding in quadrature the contributions from all sources, choosing for each item the larger of its estimated shift and its statistical uncertainty.

6.9 Results

The top-quark mass (m_t) and the jet energy scale factor (JSF) are measured using 4 356 events selected from collision data corresponding to $18.2\,\text{fb}^{-1}$ of data:

$$\begin{aligned} m_t &= 172.08 \pm 0.36\,(\text{stat.+JSF}) \pm 0.83\,(\text{syst.})\,\text{GeV} = 172.08 \pm 0.90\,\text{GeV} \\ \text{JSF} &= 1.007 \pm 0.003\,(\text{stat.}) \pm 0.011\,(\text{syst.}) \qquad\qquad = 1.007 \pm 0.011 \end{aligned}$$

With a total precision of 0.90 GeV, this constitutes the most precise measurement of the top-quark mass in all-jets decays to date. The resulting likelihood is shown in Figure 6.21 with statistical uncertainty contours. Within the measurement uncertainties, the jet energy scale factor is compatible with the default CMS JES confirming it. The faction of signal events and the fraction of correct permutations are found to be 78% and 31%, respectively. The extracted signal fraction is in good agreement with the expectation of 78% meaning that the measured cross section from all-jets events is close to the NNLO cross section calculation. A rough estimate of the systematic uncertainties yields 22%, which would directly translate into the uncertainty on a possible cross section measurement. This implies that a measurement of the top-quark pair production cross section from all-jets events is still not competitive with measurements from lepton+jets or dilepton events. The extracted fraction of correct permutations is lower than the expectation of 45%, but this is safely covered by the roughly estimated systematic uncertainty of 17%. One possibility that might explain the difference is a worse jet energy resolution in data compared to the simulated sample. A broadened jet energy resolution would not affect the position of the top-quark mass peak, but the width would increase. As there is a Gaussian part for the other permutations with a peak at the same value as the correct permutations, but with a larger width, a shifted jet energy resolution results in a shifted fraction of correct permutations with only minor influences on the extracted top-quark mass. This result is published as [108] and was presented at the ICHEP 2014 [109].

Fixing the jet energy scale factor to unity, i.e. using the default JES from CMS, one gets a top-quark mass of:

$$m_t = 172.59 \pm 0.27\,(\text{stat.}) \pm 1.05\,(\text{syst.})\,\text{GeV} = 172.59 \pm 1.08\,\text{GeV}$$

It is clearly visible that the 2D analysis reduces the uncertainty from the JES while slightly increasing the statistical uncertainty on the measurement as expected. In turn, the 1D approach reduces the uncertainties from changes in the jet energy resolution, triggering, and multijet background shape. The origin for this effect is associated to the W-boson mass distribution. Uncertainties mainly influencing this distribution and, thus, the extraction of JSF are reduced as the 1D analysis is insensitive to them. Even with these benefits in the 1D analysis, its total uncertainty is completely dominated by the much increased uncertainty from JES. The differences between the 2D and 1D analyses for all other uncertainty sources are negligible. The extracted fractions of signal events and correct permutations are 78% and 31%, like for the 2D analysis and the roughly estimated systematic uncertainties do not change, as well. Thus, the implications are the same as explained for the 2D case in the last paragraph.

Compared with all single measurements of the top-quark mass conducted so far, this measurement in all-jets final states at a centre-of-mass energy of 8 TeV with the CMS experiment is the third most precise one. An overview of the results is given in Figure 9.1. A very similar measurement at a centre-of-mass energy of 7 TeV is carried out within this thesis and is described in the next chapter.

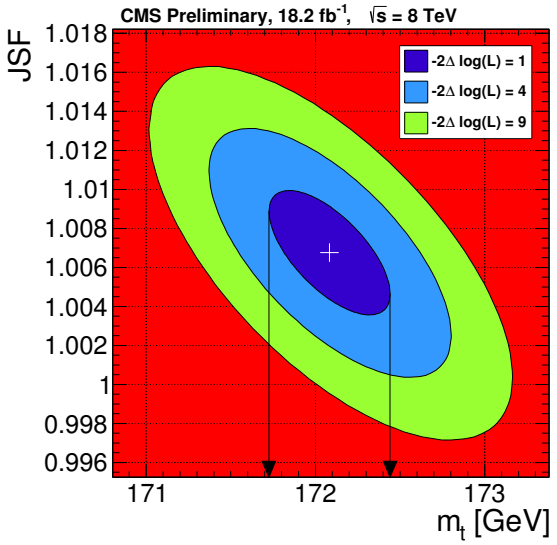

Figure 6.21: The 2D likelihood measured on 18.2 fb^{-1} of 2012 data. The ellipses correspond to statistical uncertainty contours of $-2\Delta\log(\mathcal{L}) = 1$, 4, and 9 enabling the extraction of one, two, and three σ intervals as visualised by the black arrows for one σ interval for the top-quark mass.

Chapter 7

Measurement of the Top-Quark Mass at 7 TeV

Similarly to the measurement at $\sqrt{s} = 8$ TeV, the top-quark mass is measured at 7 TeV [110, 111] within the presented thesis project. The analysis was conducted and published earlier than the 8 TeV analysis and is summarised here for completeness only. This measurement follows a very similar strategy with some slight differences outlined in this chapter.

Two triggers are used at 7 TeV. The first one (QuadJet50_Jet40) requires the presence of at least four calorimeter jets at trigger level with $p_{\mathrm{T}} > 50\,\mathrm{GeV}$ and a fifth one with $p_{\mathrm{T}} > 40\,\mathrm{GeV}$. The second trigger (QuadJet50_Jet40_Jet30), introduced due to higher instantaneous luminosities in later running periods, requires an additional sixth jet with $p_{\mathrm{T}} > 30\,\mathrm{GeV}$. As a consequence, the jet selection at reconstruction level using particle flow jets with charged hadron subtraction requires the presence of at least four jets with $p_{\mathrm{T}} > 60\,\mathrm{GeV}$, a fifth one with $p_{\mathrm{T}} > 50\,\mathrm{GeV}$, and an additional sixth jet with $p_{\mathrm{T}} > 40\,\mathrm{GeV}$. There is no requirement on calorimeter-based jets at reconstruction level. Afterwards, at least two b-tagged jets are required to be found using the combined secondary vertex algorithm at the tight working point.

The kinematic fit uses all jets instead of only the leading six jets. This increases the signal yield, but worsens the top-quark mass resolution and increases the background fraction. The selection of events is loosened to $P\left(\chi^2\right) > 0.09$ and $\Delta R_{\mathrm{b\bar{b}}} > 1.5$. This is needed to get a reasonable amount of selected events due to the lower integrated luminosity and top-quark pair production cross section at 7 TeV.

Simulated samples with generated top-quark masses of 161.5, 163.5, 166.5, 169.5, 172.5, 175.5, 178.5, 181.5, and 184.5 GeV are used. The jet energies in all these samples are scaled by factors of 0.96, 1.00, 1.04 to observe the effects of a shifted jet energy scale. In addition, the signal fraction and the fraction of correct permutations are fixed parameters for the top-quark mass extraction.

The overview of the systematic uncertainties in shown in Table 7.1. In the case of the 7 TeV analysis, the precision of the 1D analysis exceeds the one of the 2D analysis. There are two main effects responsible for this difference. Firstly, the statistical precision

	$\delta_{m_t}^{1D}$ (GeV)	$\delta_{m_t}^{2D}$ (GeV)	δ_{JSF}
Experimental uncertainties			
Calibration	**0.13**	**0.14**	**0.001**
JES	**0.97** $\pm$ 0.06	0.09 $\pm$ **0.10**	**0.002** $\pm$ 0.001
Jet energy resolution	**0.15** $\pm$ 0.06	**0.13** $\pm$ 0.10	**0.003** $\pm$ 0.001
b tagging	0.05 $\pm$ **0.06**	0.04 $\pm$ **0.10**	**0.001** $\pm$ 0.001
Pileup	0.05 $\pm$ **0.06**	0.09 $\pm$ **0.10**	**0.001** $\pm$ 0.001
Trigger	**0.24** $\pm$ 0.06	**0.26** $\pm$ 0.10	**0.006** $\pm$ 0.001
Multijet background	**0.13** $\pm$ 0.06	**0.60** $\pm$ 0.10	**0.006** $\pm$ 0.001
Modelling of hadronisation			
bJES	**0.49** $\pm$ 0.06	**0.52** $\pm$ 0.10	**0.001** $\pm$ 0.001
Modelling of the hard scattering process			
PDF	0.03 $\pm$ **0.06**	0.07 $\pm$ **0.10**	**0.001** $\pm$ 0.001
Q^2 scale	0.08 $\pm$ **0.22**	0.31 $\pm$ **0.34**	**0.005** $\pm$ 0.003
ME-PS matching threshold	**0.24** $\pm$ 0.22	0.29 $\pm$ **0.34**	0.001 $\pm$ **0.003**
Modelling of the non-perturbative QCD			
Underlying event	**0.20** $\pm$ 0.12	**0.42** $\pm$ 0.20	**0.004** $\pm$ 0.002
Colour reconnection	0.04 $\pm$ **0.15**	**0.58** $\pm$ 0.25	**0.006** $\pm$ 0.002
Total	1.21	1.23	0.013

Table 7.1: Overview of systematic uncertainties. The total is defined by adding in quadrature the contributions from all sources, choosing for each the larger of either its estimated shift or its statistical uncertainty as indicated by the bold script.

is worse at 7 TeV for both data and simulated samples. Secondly, the extraction of the top-quark mass is done with a fixed fraction of signal events and correct permutations. In the 8 TeV analysis, this is newly introduced to reduce the systematic uncertainties. Thus, the 1D result is taken as final result:

$$m_t = 173.49 \pm 0.69\,(\text{stat.}) \pm 1.21\,(\text{syst.})\,\text{GeV}$$

The overall uncertainty of the 1D analysis sums up to 1.39 GeV. The 2D result is consistent with the 1D result and gives a JSF consistent with the JES measured by CMS:

$$\begin{aligned} m_t &= 174.28 \pm 1.00\,(\text{stat.+JSF}) \pm 1.23\,(\text{syst.})\,\text{GeV} \\ \text{JSF} &= 0.991 \pm 0.008\,(\text{stat.}) \pm 0.013\,(\text{syst.}) \end{aligned}$$

The overall uncertainty on the top-quark mass in the 2D analysis is 1.58 GeV.

The differences of the resulting top-quark masses extracted at 7 and 8 TeV is discussed in section 9.3. The result is published in [110] and was presented at the Top2012 conference [111]. This measurement is part of the combination [11] of eleven results using data from four experiments at LHC and the Tevatron and part of the latest combination of CMS results [7], which is the most precise determination of

the top-quark mass to date. This measurement constitutes the second most precise determination of the top-quark mass from all-jets events and is only outperformed by the subsequent measurement, which is presented in this thesis as the main result in the previous chapter. An overview of the results is given in Figure 9.1.

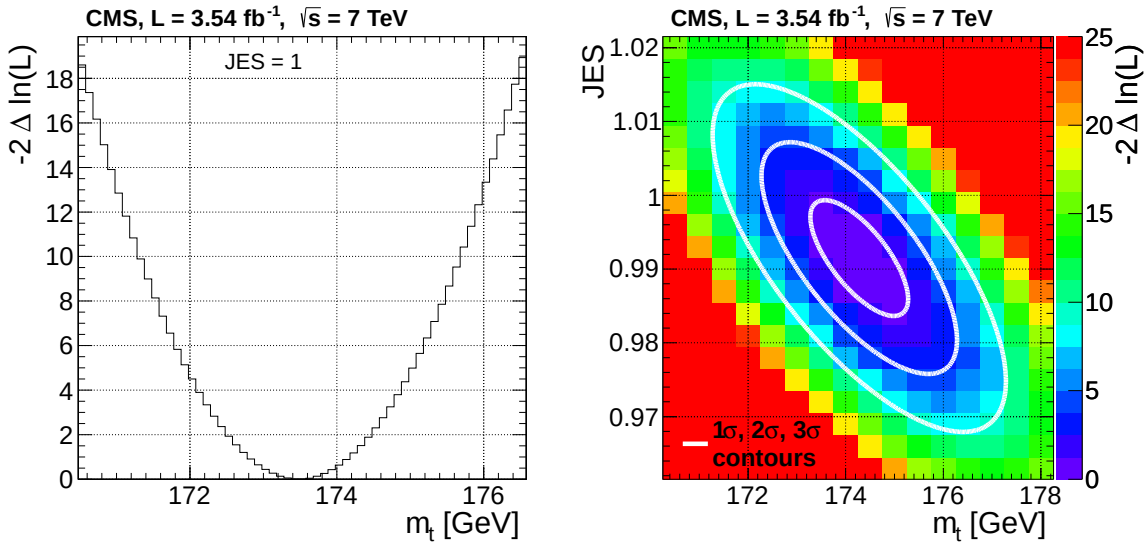

Figure 7.1: The 1D likelihood profile (left) with the JSF fixed to unity and the 2D likelihood (right) measured on 3.54 fb^{-1} of 2011 data. In this figure, the JSF is labelled as JES, but has exactly the same meaning as in the previous chapter for the 8 TeV analysis. The contours correspond to 1σ, 2σ, and 3σ statistical uncertainty.

Chapter 8

Measurement of the Top-Quark-Pair Production Cross Section

The top-quark pair production cross section is measured at 7 TeV using all-jets events [112], similarly to the measurement of the top-quark mass, within this thesis project. The slight differences are outlined here.

As this measurement was carried out quite early compared to the top-quark mass measurement, a different b-tagging algorithm, the simple secondary vertex high purity algorithm [77], is used, as the more advanced combined secondary vertex algorithm is not yet fully commissioned. In addition, the requirement on $\Delta R_{\mathrm{b\bar{b}}}$ is not done.

The background is determined by weighting events from a background dominated side-band region. This region is depleted of signal by requiring the absence of b-tagged jets. For taking into account the different kinematic properties of bottom-quark induced jets compared to jets originating from lighter quarks, the events from the side-band region are weighted such that the bottom-quark candidates match the transverse momentum and pseudorapidity distributions of b-tagged jets.

The top-quark pair production cross section is extracted from the distribution of top-quark masses from the kinematic fit. Templates for the background derived from data and signal derived from simulated samples are fitted to data with a free ratio. The extracted fraction of signal events is translated into the number of top-quark pair events. This number of events is extrapolated to the full phase space in order to yield the top-quark pair production cross section.

The overview of all uncertainties in shown in Table 8.1. The resulting top-quark pair production cross section is:

$$\sigma_{\mathrm{t\bar{t}}} = 139 \pm 10\,(\mathrm{stat.}) \pm 26\,(\mathrm{syst.}) \pm 3\,(\mathrm{lumi.})\,\mathrm{pb}$$

This result is published in [112].

Source	Relative uncertainty (%)
JES	10.1
Multijet background	9.0
b tagging	6.0
Q^2 scale	5.8
Underlying event	5.5
Trigger	5.0
Jet energy resolution	4.0
ME-PS matching threshold	4.0
Top-quark mass	2.1
Pileup	0.8
Systematic	18.6
Statistical	7.0
Luminosity	2.2
Total	20.0

Table 8.1: Overview of all uncertainties. The total is defined by adding in quadrature the contributions from all sources.

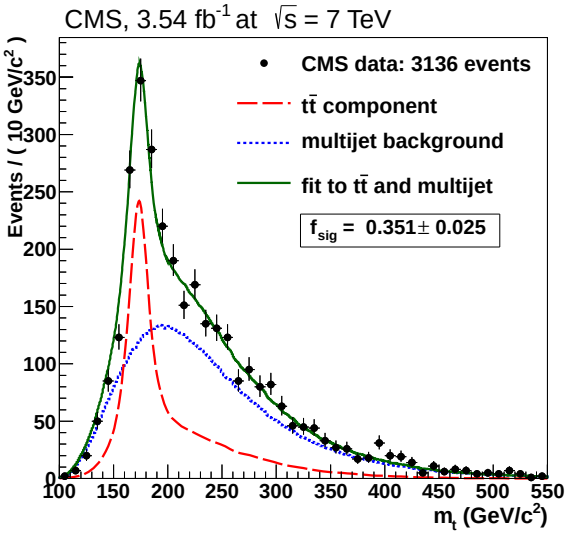

Figure 8.1: The top-quark mass from the kinematic fit is shown. The top-quark pair production cross section is extracted by fitting templates for background and signal with a free signal fraction parameter.

Chapter 9

Conclusions

In this chapter, concluding remarks and an outlook are presented. Firstly, a short overview of the results in this thesis is given and the results are interpreted. Then, the compatibility of the top-quark mass measurements at 7 and 8 TeV is evaluated. Afterwards, the compatibility of the Standard Model using the measured top-quark mass is examined. Finally, an outlook and prospects for the future are pointed out.

9.1 Overview of the Results

The main result in the presented thesis is the measurement of the top-quark mass from all-jets events with the CMS experiment at the LHC using data collected at a centre-of-mass energy of 8 TeV. This result is presented in detail in chapter 6. This constitutes the most precise measurement of the top-quark mass using all-jets events and the third most precise single measurement of the top-quark mass to date. This result is published as [108] and was presented at the ICHEP 2014 [109]:

$$m_{\mathrm{t}} = 172.08 \pm 0.36\,(\text{stat.+JSF}) \pm 0.83\,(\text{syst.})\,\text{GeV} = 172.08 \pm 0.90\,\text{GeV}$$

An earlier result is derived using similar techniques at a centre-of-mass energy of 7 TeV, as outlined in chapter 7. It yields a slightly lower precision, still representing the second most precise measurement of the top-quark mass in all-jets events. The result is published in [110] and was presented at the Top2012 conference [111]:

$$m_{\mathrm{t}} = 173.49 \pm 0.69\,(\text{stat.}) \pm 1.21\,(\text{syst.})\,\text{GeV} = 173.49 \pm 1.39\,\text{GeV}$$

This result is part of the latest combination of CMS top-quark mass results [7], which is the most precise determination of the top-quark mass to date. A comparison of these results with other measurements is given in Figure 9.1 and is discussed in the next section.

The earliest result for this final state is covered briefly in chapter 8 of this thesis. It is the measurement of the top-quark pair production cross section at a centre-of-mass energy of 7 TeV. This result is published in [112]:

$$\sigma_{\mathrm{t\bar{t}}} = 139 \pm 10\,(\text{stat.}) \pm 26\,(\text{syst.}) \pm 3\,(\text{lumi.})\,\text{pb} = 139 \pm 28\,\text{pb}$$

9.2 Interpretation of the Results

In this thesis, it is shown that it is possible to do precision measurements at hadron colliders in purely hadronic final states. The main problem for high precision measurements in such final states stems from proper estimation of the rate of events for the final state of interest itself and for background processes. This is the reason for the comparably poor performance of the cross section measurement.

As soon as the measurement is mainly sensitive to the shape of a distribution, as it is the case for the top-quark mass analyses, the precision of the measurements may increase significantly. This leads to a very competitive measurement for the top-quark mass compared to analyses using the lepton+jets final state. Due to the enormous background, more stringent selection requirements are needed in the all-jets channel. This results in a lower number of selected events leading to slightly worse precision compared to the lepton+jets decay mode. This affects not only the statistical uncertainty, but the systematic uncertainty, as well, as several sources are limited by the size of the simulated data set. In Figure 9.1, the comparison of the top-quark mass measurements presented in this thesis and the corresponding CMS analyses in the lepton+jets decay mode are shown. This visualises the compatibility and competitiveness of these measurements. In addition, the top-quark mass result from 7 TeV is included in two important top-quark mass combinations:

- world combination [11] with eleven results from ATLAS, CDF, CMS, and D0
- CMS combination [7], which includes the latest, most precise CMS measurement

These combinations are highlighted in Figure 9.1, as well. The CMS combination is the most precise determination of the top-quark mass to date. In addition, the two top-quark mass measurements presented in this thesis constitute the two most precise top-quark mass determinations from all-jets events. In Figure 9.1, the two latest all-jets top-quark mass measurements from ATLAS [88] and CDF [10] are shown for comparison. In addition, the most precise single measurement by D0 in the lepton+jets decay mode [8] is shown.

9.3 Compatibility of the Measurements of the Top-Quark Mass at 7 and 8 TeV

The compatibility of the two presented top-quark mass measurements at 7 and 8 TeV is checked as the main results yield top-quark masses differing by 1.41 GeV. The assumptions, under which the compatibility is tested, are a full correlation of the theoretical uncertainties. The experimental uncertainties are assumed to be uncorrelated as they are derived from data itself in each running period individually. This gives a difference for the main results at 7 and 8 TeV of 1.02 standard deviations. Even under the assumption that most of the experimental uncertainties are correlated, except for the uncertainties due to triggering, background, and pileup modelling, all being determined from data, the deviation of the two main results does not exceed 1.57 standard deviations. When looking at the 2D result from 7 TeV the difference of the

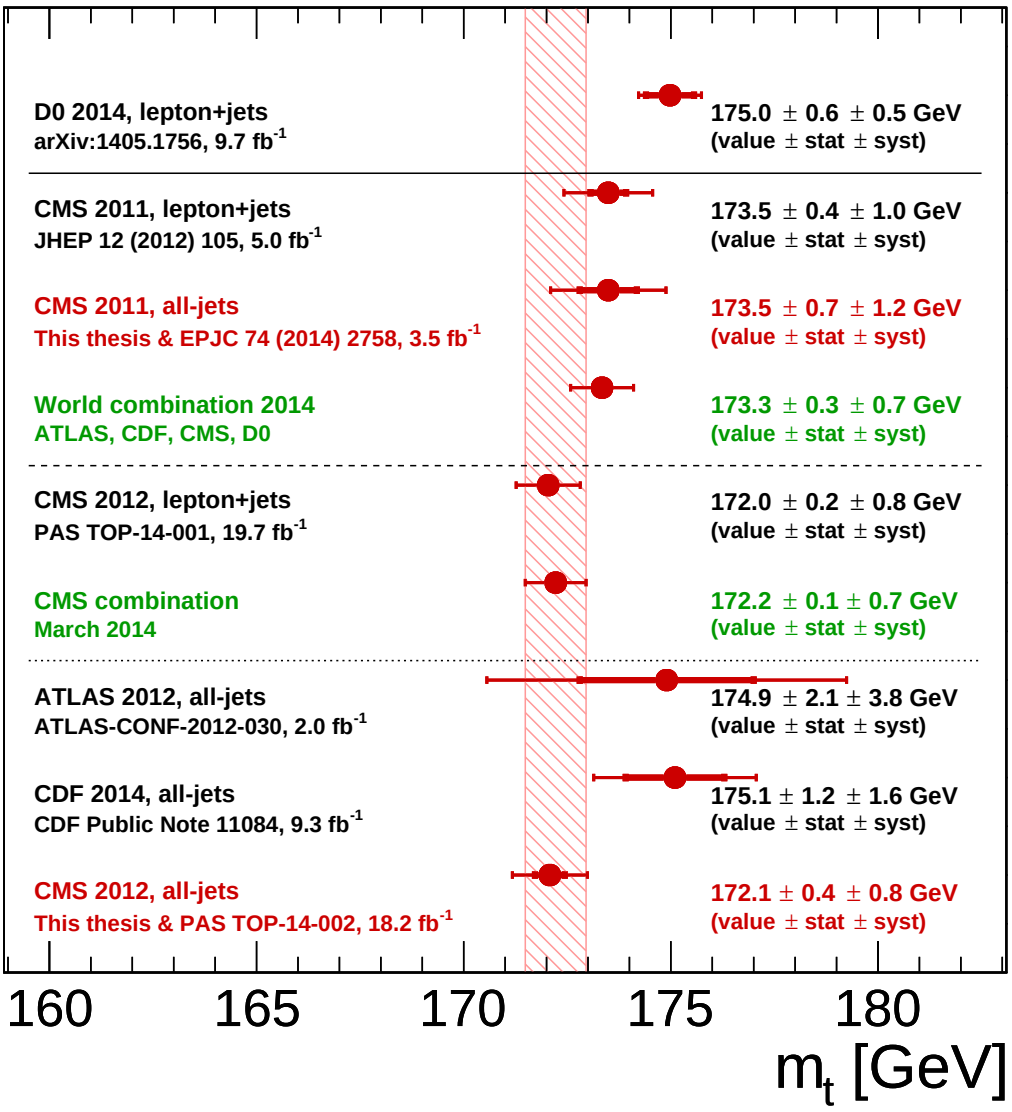

Figure 9.1: Overview of top-quark mass results. The results highlighted in red are the results presented in this thesis. They constitute the two most precise measurements of the top-quark mass from all-jets events to date. The top-quark mass result from this thesis at 7 TeV is included in the latest world and CMS combinations highlighted in green. The result shown on the top is the most precise single measurement of the top-quark mass. The individual results in the second (and third) block are part of the latest world (CMS) combination. The CMS combination is the most precise determination of the top-quark mass to date, thus, it is highlighted as vertical band. For comparison, the two latest all-jets results from ATLAS and CDF are compared with the latest result from the presented thesis in the last block.

top-quark masses rises to 2.20 GeV. The deviation of this measurement with the most precise result from 8 TeV is 1.63 and 1.81 standard deviations for the two different correlation scenarios, respectively.

9.4 Standard Model Compatibility with the Measured Top-Quark Mass

The top quark plays a crucial role in the context of the Standard Model of particle physics, as outlined in chapter 2. Especially, its mass can be used to check the self-consistency of the SM, as already shown in section 2.2.4. In the following, the consistency of the SM assuming the top-quark mass measured in this thesis is evaluated with the help of Gfitter [41, 42].

When the resulting top-quark mass from this thesis is used with its uncertainty for the fit of the SM using Gfitter, a p-value of 0.15 is reached. This is a slightly lower p-value compared to the SM fit using the world combination [11], which gives a p-value of 0.21. In Figure 9.2, the result of this fit of the SM assuming the top-quark mass measured in this thesis is visualised. Hence, the top-quark mass measured in this thesis puts a slightly higher tension on the SM compared to the world combination, but still the SM can be regarded as a completely consistent theory.

When looking at the stability of the electroweak vacuum, the top-quark mass

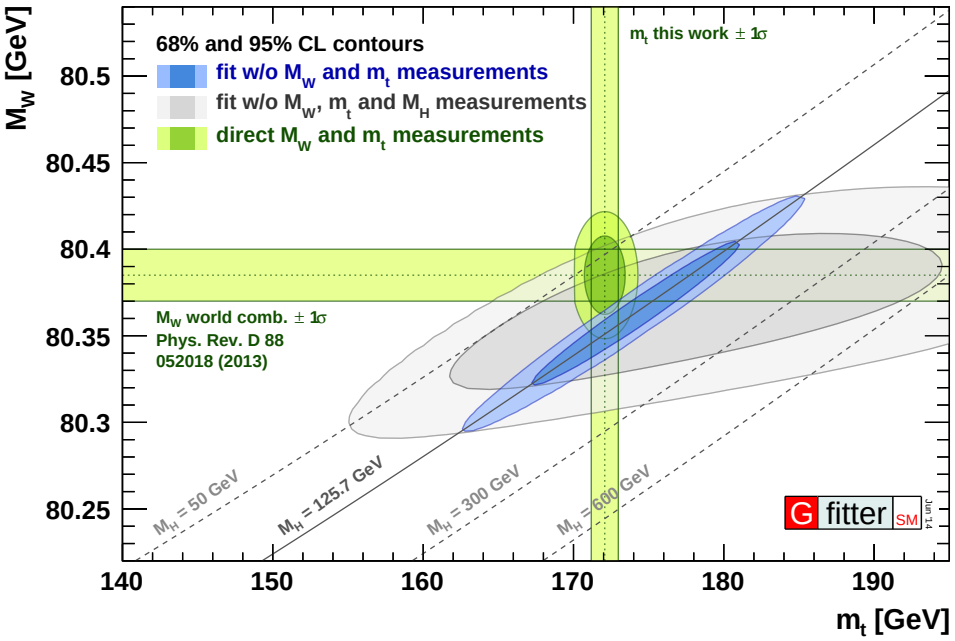

Figure 9.2: The result from Gfitter using the most precise top-quark mass measured in this thesis. Figure kindly provided by [113].

measured in this thesis leads to a more stable electroweak vacuum lying on the edge between metastability and stability. Within the uncertainty of the measurement the stable region is reached leading to the conclusion that the SM could be valid until gravity starts to play an important role close to the Planck scale.

Comparing these two predictions, one can see a little contradiction as the result from Gfitter implies that a higher top-quark mass is needed for a fully consistent SM, whereas the vacuum stability would require a lower value of the top-quark mass for the SM being valid up to the Planck scale. This could be interpreted as another little hint, in addition to the implication from sections 2.1.5 and 2.2.4, that some new physics is needed to give a fully consistent theory at all energy scales below the Planck scale.

9.5 Outlook

In particular, the two top-quark mass measurements show that high precision physics is possible even at hadron colliders in purely hadronic final states. Future prospects are measurements with an even higher precision than reached so far in this final state. When the LHC will be restarted with a much higher centre-of-mass energy of 13-14 TeV for proton-proton collisions, the production cross section for top-quark pairs will rise by a factor of three to four [36]. A better focusing of the beams may be achieved due to the higher beam energies. These effects then lead to a higher production rate for top-quark pairs by more than a factor of five. This will give the possibility for even more detailed studies of the top quark.

The biggest challenge for analyses in all-jets final states will be the triggering of the events. The parking of data sets is no option for the next running period of the LHC, as the storage and computing resources are limited. Thus, the rates of the triggers have to be brought to a reasonable amount of a few hundred events per second. Latest studies give hope for a much improved trigger [114]. The particle flow concept may already be used at trigger level for all jets in combination with proper pileup corrections. With the help of these techniques, the trigger rate for possible four jet triggers, as the ones used for the 8 TeV analysis presented here, or triggers requiring at least five or six jets, seems reasonable. In addition, the possibility to employ b tagging already for triggering is an option to further reduce the rate, if needed.

Comparing the measurement of the top-quark mass using all-jets events to measurements from final states with one charged lepton, one can already see that the systematic precision reached the same level. Only the statistical precision is lower for measurements from all-jets events as much harder selection criteria are needed to reduce the background from multijet production. The difference in precision will become less pronounced for future measurements as the statistical component of the uncertainty will play a less important role in a much bigger data set. For both measurements of the top-quark mass from all-jets events presented in this thesis, it is observed that some systematic uncertainties are dominated by the statistical precision of the simulated samples. This leads to the need of larger simulated samples for future analyses, which is very demanding from the point of view of computing resources.

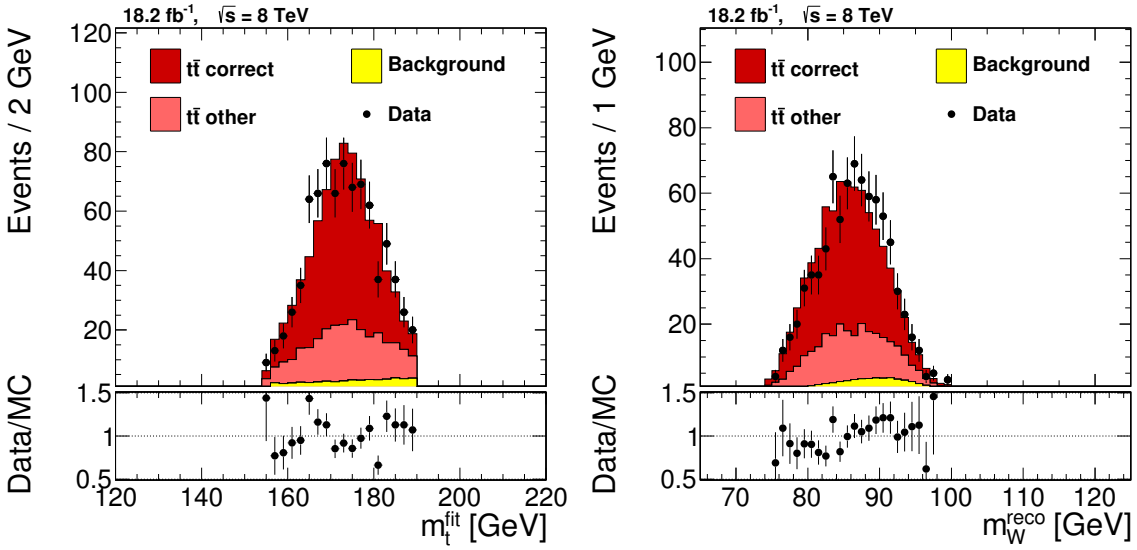

Figure 9.3: On the left, the top-quark mass from the kinematic fit and, on the right, the reconstructed average W-boson mass are shown, respectively. The additional selection criteria to arrive at these distributions are: $P\left(\chi^2\right) > 0.4$, $\Delta R_{\mathrm{b\bar{b}}} > 2.5$, and $155\,\mathrm{GeV} < m_{\mathrm{t}}^{\mathrm{fit}} < 190\,\mathrm{GeV}$.

The improved reconstruction of the top-quark pair events using the kinematic fit comparing the measurements of the top-quark mass from 7 TeV and 8 TeV leads to an enhanced precision. For a data sample with even more events, one could tighten the selection criteria and, thus, use only well reconstructed top-quark pair events and further reduce the background. First studies show that signal purities of 94% are in reach, illustrated in Figure 9.3. This is achieved by tightening the selection criteria to $P\left(\chi^2\right) > 0.4$ and $\Delta R_{\mathrm{b\bar{b}}} > 2.5$ and in addition imposing the criterion that $155\,\mathrm{GeV} < m_{\mathrm{t}}^{\mathrm{fit}} < 190\,\mathrm{GeV}$. As the windows around the top-quark mass from the kinematic fit is quite large, this should not bias a top-quark mass measurement. This would, for the first time, give the possibility to study a very pure sample of top-quark pair events in the all-jets final state.

All this leads to the final conclusion that the top quark is still one of the most interesting subjects of future studies. This statement is even strengthened with the recent discovery of the Higgs boson. Thus, the measurement of the top-quark mass has become one of the most essential cornerstones of the Standard Model and has higher significance than ever before.

Appendix A

List Data Samples

/MultiJet1Parked/Run2012B-05Nov2012-v2/AOD
/MultiJet1Parked/Run2012C-part1_05Nov2012-v2/AOD
/MultiJet1Parked/Run2012C-part2_05Nov2012-v2/AOD
/MultiJet1Parked/Run2012D-part1_10Dec2012-v1/AOD
/MultiJet1Parked/Run2012D-part2_17Jan2013-v1/AOD
/MultiJet1Parked/Run2012D-part2_PixelRecover_17Jan2013-v1/AOD

Table A.1: List of data samples used for the 8 TeV top-quark mass analysis.

/TTJets_MSDecays_mass166_5_TuneZ2star_8TeV-madgraph-tauola/Summer12_DR53X-PU_S10_START53_V19-v1/AODSIM
/TTJets_MSDecays_mass169_5_TuneZ2star_8TeV-madgraph-tauola/Summer12_DR53X-PU_S10_START53_V19-v1/AODSIM
/TTJets_MSDecays_mass171_5_TuneZ2star_8TeV-madgraph-tauola/Summer12_DR53X-PU_S10_START53_V19-v1/AODSIM
/TTJets_MSDecays_central_TuneZ2star_8TeV-madgraph-tauola/Summer12_DR53X-PU_S10_START53_V19-v1/AODSIM
/TTJets_MSDecays_mass173_5_TuneZ2star_8TeV-madgraph-tauola/Summer12_DR53X-PU_S10_START53_V19-v1/AODSIM
/TTJets_MSDecays_mass175_5_TuneZ2star_8TeV-madgraph-tauola/Summer12_DR53X-PU_S10_START53_V19-v1/AODSIM
/TTJets_MSDecays_mass178_5_TuneZ2star_8TeV-madgraph-tauola/Summer12_DR53X-PU_S10_START53_V19-v1/AODSIM
/TTJets_MSDecays_matchingup_TuneZ2star_8TeV-madgraph-tauola/Summer12_DR53X-PU_S10_START53_V19-v2/AODSIM
/TTJets_MSDecays_matchingdown_TuneZ2star_8TeV-madgraph-tauola/Summer12_DR53X-PU_S10_START53_V19-v1/AODSIM
/TTJets_MSDecays_matchingdown_TuneZ2star_8TeV-madgraph-tauola/Summer12_DR53X-PU_S10_START53_V19-v2/AODSIM
/TTJets_MSDecays_scaleup_TuneZ2star_8TeV-madgraph-tauola/Summer12_DR53X-PU_S10_START53_V19-v1/AODSIM
/TTJets_MSDecays_scaledown_TuneZ2star_8TeV-madgraph-tauola/Summer12_DR53X-PU_S10_START53_V19-v1/AODSIM
/TT_CT10_TuneZ2star_8TeV-powheg-tauola/Summer12_DR53X-PU_S10_START53_V7A-v2/AODSIM
/TT_CT10_AUET2_8TeV-powheg-herwig/Summer12_DR53X-PU_S10_START53_V19-v1/AODSIM
/TT_8TeV-mcatnlo/Summer12_DR53X-PU_S10_START53_V7A-v1/AODSIM
/TTJets_HadronicMGDecays_8TeV-madgraph/Summer12_DR53X-PU_S10_START53_V7A-v1/AODSIM
/TTJets_HadronicMGDecays_8TeV-madgraph/Summer12_DR53X-PU_S10_START53_V7A_ext-v1/AODSIM
/TTJets_SemiLeptMGDecays_8TeV-madgraph-tauola/Summer12_DR53X-PU_S10_START53_V7C-v1/AODSIM
/TTJets_FullLeptMGDecays_8TeV-madgraph-tauola/Summer12_DR53X-PU_S10_START53_V7C-v2/AODSIM
/TTJets_HadronicMGDecays_TuneP11_8TeV-madgraph-tauola/Summer12_DR53X-PU_S10_START53_V19-v1/AODSIM
/TTJets_SemiLeptMGDecays_TuneP11_8TeV-madgraph-tauola/Summer12_DR53X-PU_S10_START53_V19-v1/AODSIM
/TTJets_FullLeptMGDecays_TuneP11_8TeV-madgraph-tauola/Summer12_DR53X-PU_S10_START53_V19-v1/AODSIM
/TTJets_HadronicMGDecays_TuneP11mpiHi_8TeV-madgraph-tauola/Summer12_DR53X-PU_S10_START53_V19-v1/AODSIM
/TTJets_SemiLeptMGDecays_TuneP11mpiHi_8TeV-madgraph-tauola/Summer12_DR53X-PU_S10_START53_V19-v1/AODSIM
/TTJets_FullLeptMGDecays_TuneP11mpiHi_8TeV-madgraph-tauola/Summer12_DR53X-PU_S10_START53_V19-v1/AODSIM
/TTJets_HadronicMGDecays_TuneP11TeV_8TeV-madgraph-tauola/Summer12_DR53X-PU_S10_START53_V19-v1/AODSIM
/TTJets_SemiLeptMGDecays_TuneP11TeV_8TeV-madgraph-tauola/Summer12_DR53X-PU_S10_START53_V19-v1/AODSIM
/TTJets_FullLeptMGDecays_TuneP11TeV_8TeV-madgraph-tauola/Summer12_DR53X-PU_S10_START53_V19-v1/AODSIM
/TTJets_HadronicMGDecays_TuneP11noCR_8TeV-madgraph-tauola/Summer12_DR53X-PU_S10_START53_V19-v1/AODSIM
/TTJets_SemiLeptMGDecays_TuneP11noCR_8TeV-madgraph-tauola/Summer12_DR53X-PU_S10_START53_V19-v1/AODSIM
/TTJets_FullLeptMGDecays_TuneP11noCR_8TeV-madgraph-tauola/Summer12_DR53X-PU_S10_START53_V19-v1/AODSIM
/TTJets_HadronicMGDecays_8TeV-madgraph/Summer12_DR53X-PU_RD1_START53_V7N-v1/AODSIM
/TTJets_SemiLeptMGDecays_8TeV-madgraph/Summer12_DR53X-PU_RD1_START53_V7N-v1/AODSIM
/TTJets_FullLeptMGDecays_8TeV-madgraph/Summer12_DR53X-PU_RD1_START53_V7N-v1/AODSIM
/QCD_HT-100To250_TuneZ2star_8TeV-madgraph-pythia/Summer12_DR53X-PU_S10_START53_V7A-v1/AODSIM
/QCD_HT-250To500_TuneZ2star_8TeV-madgraph-pythia6/Summer12_DR53X-PU_S10_START53_V7A-v1/AODSIM
/QCD_HT-500To1000_TuneZ2star_8TeV-madgraph-pythia6/Summer12_DR53X-PU_S10_START53_V7A-v1/AODSIM
/QCD_HT-1000ToInf_TuneZ2star_8TeV-madgraph-pythia6/Summer12_DR53X-PU_S10_START53_V7A-v1/AODSIM

Table A.2: List of simulated samples used for the 8 TeV top-quark mass analysis.

List of Figures

List of Tables

Bibliography

[1] LHC Study Group, "The Large Hadron Collider: conceptual design", Technical Report CERN-AC-95-05 LHC, CERN, Geneva, (Oct, 1995).

[2] "Design report Tevatron 1 Project", Technical Report FERMILAB-DESIGN-1982-01, Fermi National Accelerator Laboratory, Batavia, Illinois, (1982).

[3] "Design Report Tevatron 1 Project", Technical Report FERMILAB-DESIGN-1984-01, Fermi National Accelerator Laboratory, Batavia, Illinois, (1984).

[4] CMS Collaboration, "CMS Physics: Technical Design Report Volume 1: Detector Performance and Software", Technical Design Report CERN-LHCC-2006-001, CMS-TDR-008-1, Geneva, (2006).

[5] CMS Collaboration, "CMS technical design report, volume II: Physics performance", *J.Phys.* **G34** (2007) 995–1579. doi:10.1088/0954-3899/34/6/S01.

[6] D0 Collaboration, "Design Report", Technical Report FERMILAB-DESIGN-1984-02, Fermi National Accelerator Laboratory, Batavia, Illinois, (1984).

[7] CMS Collaboration, "Measurement of the top-quark mass in $t\bar{t}$ events with lepton+jets final states in pp collisions at $\sqrt{s} = 8\,\text{TeV}$", CMS Physics Analysis Summary CMS-PAS-TOP-14-001, CERN, Geneva, (March, 2014).

[8] D0 Collaboration, "Precision measurement of the top-quark mass in lepton+jets final states", arXiv:1405.1756.

[9] CDF Collaboration, "Design Report of the Fermilab Collider Detector Facility (CDF)", Technical Report FERMILAB-DESIGN-1981-02, Fermi National Accelerator Laboratory, Batavia, Illinois, (August, 1981).

[10] CDF Collaboration, "Measurement of m_t in the all-hadronic channel using $9.3\,\text{fb}^{-1}$", CDF Public Note 11084, Fermilab, (March, 2014).

[11] ATLAS, CDF, CMS, and D0 Collaborations, "First combination of Tevatron and LHC measurements of the top-quark mass", arXiv:1403.4427.

[12] "Standard Model of Elementary Particles", (Feb, 2014). http://commons.wikimedia.org/wiki/File:Standard_Model_of_Elementary_Particles.svg.

[13] F. Halzen and A. Martin, "Quarks & Leptons: An Introductory Course in Modern Particle Physics". John Wiley & Sons, Inc., 1984. 396p.

[14] CMS Collaboration, "Observation of a new boson at a mass of 125 GeV with the CMS experiment at the LHC", *Phys.Lett.* **B716** (2012) 30–61, arXiv:1207.7235. doi:10.1016/j.physletb.2012.08.021.

[15] Particle Data Group, "Review of Particle Physics (RPP)", *Phys.Rev.* **D86** (Jul, 2012) 010001. 2013 partial update for the 2014 edition. doi:10.1103/PhysRevD.86.010001.

[16] F. Capozzi, G. Fogli, E. Lisi et al., "Status of three-neutrino oscillation parameters, circa 2013", *Phys.Rev.* **D89** (2014) 093018, arXiv:1312.2878. doi:10.1103/PhysRevD.89.093018.

[17] P. W. Higgs, "Broken Symmetries and the Masses of Gauge Bosons", *Phys. Rev. Lett.* **13** (1964) 508 – 509. doi:10.1103/PhysRevLett.13.508.

[18] F. Englert and R. Brout, "Broken Symmetry and the Mass of Gauge Vector Mesons", *Phys. Rev. Lett.* **13** (1964) 321 – 323. doi:10.1103/PhysRevLett.13.321.

[19] G. S. Guralnik, C. R. Hagen, and T. W. B. Kibble, "Global Conservation Laws and Massless Particles", *Phys. Rev. Lett.* **13** (1964) 585 – 587. doi:10.1103/PhysRevLett.13.585.

[20] T. Aoyama, M. Hayakawa, T. Kinoshita et al., "Quantum electrodynamics calculation of lepton anomalous magnetic moments: Numerical approach to the perturbation theory of QED", *PTEP* **2012** (2012) 01A107. doi:10.1093/ptep/pts030.

[21] M. Kobayashi and T. Maskawa, "CP Violation in the Renormalizable Theory of Weak Interaction", *Prog.Theor.Phys.* **49** (1973) 652–657. doi:10.1143/PTP.49.652.

[22] CDF Collaboration, "Observation of top quark production in $\bar{p}p$ collisions", *Phys.Rev.Lett.* **74** (1995) 2626–2631, arXiv:hep-ex/9503002. doi:10.1103/PhysRevLett.74.2626.

[23] D0 Collaboration, "Search for high mass top quark production in $p\bar{p}$ collisions at $\sqrt{s} = 1.8$ TeV", *Phys.Rev.Lett.* **74** (1995) 2422–2426, arXiv:hep-ex/9411001. doi:10.1103/PhysRevLett.74.2422.

[24] R. Feynman, F. Morinigo, W. Wagner et al., "Feynman lectures on gravitation",.

[25] A. Diaferio, S. Schindler, and K. Dolag, "Clusters of Galaxies: Setting the Stage", *Space Science Reviews* **134** (2008) 7–24, arXiv:0801.0968. doi:10.1007/s11214-008-9324-5.

[26] Supernova Search Team, "Observational Evidence from Supernovae for an Accelerating Universe and a Cosmological Constant", *The Astronomical Journal* **116** (1998) 1009, arXiv:9805201. doi:10.1086/300499.

[27] The Supernova Cosmology Project, "Measurements of Ω and Λ from 42 High-Redshift Supernovae", *The Astrophysical Journal* **517** (1999) 565, arXiv:9812133. doi:10.1086/307221.

[28] P. Peebles and B. Ratra, "The Cosmological constant and dark energy", *Rev.Mod.Phys.* **75** (2003) 559–606, arXiv:astro-ph/0207347. doi:10.1103/RevModPhys.75.559.

[29] J.-M. Lamarre, J. Puget, F. Bouchet et al., "The planck high frequency instrument, a 3rd generation cmb experiment, and a full sky submillimeter survey", *New Astron.Rev.* (2003) arXiv:astro-ph/0308075.

[30] Planck Collaboration, "The Scientific programme of Planck", arXiv:astro-ph/0604069.

[31] Planck Collaboration, "Planck 2013 results. XVI. Cosmological parameters", arXiv:1303.5076.

[32] H1 and ZEUS Collaborations, "Proton structure measurements and PDFs at HERA", *Nucl.Phys.Proc.Suppl.* **222-224** (2012) 24–34. doi:10.1016/j.nuclphysbps.2012.03.004.

[33] V. Gribov and L. Lipatov, "Deep inelastic e p scattering in perturbation theory", *Sov.J.Nucl.Phys.* **15** (1972) 438–450.

[34] G. Altarelli and G. Parisi, "Asymptotic Freedom in Parton Language", *Nucl.Phys.* **B126** (1977) 298. doi:10.1016/0550-3213(77)90384-4.

[35] Y. L. Dokshitzer, "Calculation of the Structure Functions for Deep Inelastic Scattering and e+ e- Annihilation by Perturbation Theory in Quantum Chromodynamics.", *Sov.Phys.JETP* **46** (1977) 641–653.

[36] M. Czakon, P. Fiedler, and A. Mitov, "Total Top-Quark Pair-Production Cross Section at Hadron Colliders Through $O(\alpha_S^4)$", *Phys.Rev.Lett.* **110** (2013) 252004, arXiv:1303.6254. doi:10.1103/PhysRevLett.110.252004.

[37] A. Buckley, J. Butterworth, S. Gieseke et al., "General-purpose event generators for LHC physics", *Phys.Rept.* **504** (2011) 145–233, arXiv:1101.2599. doi:10.1016/j.physrep.2011.03.005.

[38] CMS Collaboration, "Determination of the top-quark pole mass and strong coupling constant from the $t\bar{t}$ production cross section in pp collisions at $\sqrt{s} = 7$ TeV", *Phys.Lett.* **B728** (2014) 496–517, arXiv:1307.1907. doi:10.1016/j.physletb.2013.12.009.

[39] M. Mangano, "Interpreting the top quark mass: theoretical and MC aspects". https://indico.desy.de/contributionDisplay.py?sessionId=9&contribId=30&confId=7095.

[40] W. J. Marciano, "Precision electroweak measurements and the Higgs mass", *eConf* **C040802** (2004) L009, arXiv:hep-ph/0411179.

[41] M. Baak, M. Goebel, J. Haller et al., "The Electroweak Fit of the Standard Model after the Discovery of a New Boson at the LHC", *Eur.Phys.J.* **C72** (2012) 2205, arXiv:1209.2716. doi:10.1140/epjc/s10052-012-2205-9.

[42] M. Baak, J. Cuth, J. Haller et al., "The global electroweak fit at NNLO and prospects for the LHC and ILC", arXiv:1407.3792.

[43] S. P. Martin, "A Supersymmetry primer", arXiv:hep-ph/9709356. Version 6 (Sep 2011) contains a new chapter on superspace and superfields, and many other updates.

[44] G. Degrassi, S. Di Vita, J. Elias-Miro et al., "Higgs mass and vacuum stability in the Standard Model at NNLO", *JHEP* **1208** (2012) 098, arXiv:1205.6497. doi:10.1007/JHEP08(2012)098.

[45] ALICE Collaboration, "Heavy ion collisions at the LHC: The Alice experiment", arXiv:hep-ph/9612221.

[46] ALICE Collaboration, "ALICE technical design report: Detector for high momentum PID", CERN-LHCC-98-19, (1998).

[47] ATLAS Collaboration, "ATLAS: Detector and physics performance technical design report. Volume 1", CERN-LHCC-99-14, ATLAS-TDR-14, (1999).

[48] ATLAS Collaboration, "ATLAS: Detector and physics performance technical design report. Volume 2", CERN-LHCC-99-15, ATLAS-TDR-15, (1999).

[49] LHCb Collaboration, "LHCb technical design report: Reoptimized detector design and performance", CERN-LHCC-2003-030, (2003).

[50] C. Lefvre, "The CERN accelerator complex - Complexe des accélérateurs du CERN", (Dec, 2008). http://cdsweb.cern.ch/record/1260465.

[51] M. Lamont, "Status of the LHC", *J.Phys.Conf.Ser.* **455** (2013) 012001. doi:10.1088/1742-6596/455/1/012001.

[52] CMS Collaboration, "CMS 3D Image for Inclusion in Presentations". https://cms-docdb.cern.ch/cgi-bin/DocDB/ShowDocument?docid=2716.

[53] CMS Collaboration, "Alignment of the CMS Silicon Tracker during Commissioning with Cosmic Rays", *JINST* **5** (2010) T03009, arXiv:0910.2505. doi:10.1088/1748-0221/5/03/T03009.

[54] P. M. Nadolsky, H.-L. Lai, Q.-H. Cao et al., "Implications of CTEQ global analysis for collider observables", *Phys. Rev. D* **78** (2008) 013004, arXiv:0802.0007. doi:10.1103/PhysRevD.78.013004.

[55] J. Alwall, M. Herquet, F. Maltoni et al., "MadGraph 5: going beyond", *JHEP* **06** (2011) 128, arXiv:1106.0522. doi:10.1007/JHEP06(2011)128.

[56] P. Artoisenet, R. Frederix, O. Mattelaer et al., "Automatic spin-entangled decays of heavy resonances in Monte Carlo simulations", *JHEP* **03** (2013) 015, arXiv:1212.3460. doi:10.1007/JHEP03(2013)015.

[57] T. Sjöstrand, S. Mrenna, and P. Z. Skands, "PYTHIA 6.4 Physics and Manual", *JHEP* **05** (2006) 026, arXiv:hep-ph/0603175. doi:10.1088/1126-6708/2006/05/026.

[58] CMS Collaboration, "Measurement of the Underlying Event Activity at the LHC with $\sqrt{s} = 7$ TeV and Comparison with $\sqrt{s} = 0.9$ TeV", *JHEP* **1109** (2011) 109, arXiv:1107.0330. doi:10.1007/JHEP09(2011)109.

[59] GEANT4 Collaboration, "GEANT4—a simulation toolkit", *Nucl. Instrum. Meth. A* **506** (2003) 250. doi:10.1016/S0168-9002(03)01368-8.

[60] P. Nason, "A New method for combining NLO QCD with shower Monte Carlo algorithms", *JHEP* **0411** (2004) 040, arXiv:hep-ph/0409146. doi:10.1088/1126-6708/2004/11/040.

[61] S. Frixione, P. Nason, and C. Oleari, "Matching NLO QCD computations with Parton Shower simulations: the POWHEG method", *JHEP* **0711** (2007) 070, arXiv:0709.2092. doi:10.1088/1126-6708/2007/11/070.

[62] S. Alioli, P. Nason, C. Oleari et al., "A general framework for implementing NLO calculations in shower Monte Carlo programs: the POWHEG BOX", *JHEP* **1006** (2010) 043, arXiv:1002.2581. doi:10.1007/JHEP06(2010)043.

[63] S. Frixione, P. Nason, and G. Ridolfi, "A Positive-weight next-to-leading-order Monte Carlo for heavy flavour hadroproduction", *JHEP* **0709** (2007) 126, arXiv:0707.3088. doi:10.1088/1126-6708/2007/09/126.

[64] S. Frixione and B. R. Webber, "Matching NLO QCD computations and parton shower simulations", *JHEP* **0206** (2002) 029, arXiv:hep-ph/0204244. doi:10.1088/1126-6708/2002/06/029.

[65] S. Frixione, P. Nason, and B. R. Webber, "Matching NLO QCD and parton showers in heavy flavor production", *JHEP* **0308** (2003) 007, arXiv:hep-ph/0305252. doi:10.1088/1126-6708/2003/08/007.

[66] M. L. Mangano, M. Moretti, F. Piccinini et al., "Matching matrix elements and shower evolution for top-quark production in hadronic collisions", *JHEP* **01** (2007) 013, arXiv:hep-ph/0611129. doi:10.1088/1126-6708/2007/01/013.

[67] G. Marchesini, B. Webber, G. Abbiendi et al., "HERWIG: A Monte Carlo event generator for simulating hadron emission reactions with interfering gluons. Version 5.1 - April 1991", *Comput.Phys.Commun.* **67** (1992) 465–508. doi:10.1016/0010-4655(92)90055-4.

[68] G. Corcella, I. Knowles, G. Marchesini et al., "HERWIG 6: An Event generator for hadron emission reactions with interfering gluons (including supersymmetric processes)", *JHEP* **0101** (2001) 010, arXiv:hep-ph/0011363. doi:10.1088/1126-6708/2001/01/010.

[69] CMS Collaboration, "CMSSW Reference Manual". https://cmssdt.cern.ch/SDT/doxygen/CMSSW_5_3_14/doc/html/.

[70] CMS Collaboration, "Particle-Flow Event Reconstruction in CMS and Performance for Jets, Taus and E_T^{miss}", CMS Physics Analysis Summary CMS-PAS-PFT-09-001, CERN, Geneva, (April, 2009).

[71] CMS Collaboration, "CMS slice". https://cms-docdb.cern.ch/cgi-bin/PublicDocDB/ShowDocument?docid=5581.

[72] M. Cacciari, G. P. Salam, and G. Soyez, "The anti-k_t Jet Clustering Algorithm", *JHEP* **04** (2008) 063, arXiv:0802.1189. doi:10.1088/1126-6708/2008/04/063.

[73] Private communication with Henning Kirschenmann.

[74] CMS Collaboration, "Determination of Jet Energy Calibration and Transverse Momentum Resolution in CMS", *JINST* **6** (2011) P11002, arXiv:1107.4277. doi:10.1088/1748-0221/6/11/P11002.

[75] CMS Collaboration, "8 TeV Jet Energy Corrections and Uncertainties based on 19.8 fb^{-1} of data in CMS", CMS Detector Performance Note CMS-DP-2013-033, CERN, Geneva, (2013).

[76] Private communication with Holger Enderle.

[77] CMS Collaboration, "Identification of b-quark jets with the CMS experiment", *JINST* **8** (2013) P04013, arXiv:1211.4462. doi:10.1088/1748-0221/8/04/P04013.

[78] CMS Collaboration, "Performance of b tagging at $\sqrt{s} = 8$ TeV in multijet, $\text{t}\bar{\text{t}}$ and boosted topology events", CMS Physics Analysis Summary CMS-PAS-BTV-13-001, CERN, Geneva, (2013).

[79] V. Blobel and E. Lohrmann, "Statistische und numerische Methoden der Datenanalyse". Teubner Studienbcher, B.G. Teubner, 1998. 355p.

[80] CMS Collaboration, "Fitting of Event Topologies with External Kinematic Constraints in CMS", CMS Note 2006/023, Geneva, (2006).

[81] E. Schlieckau, "First Candidates of Top Quark Events in the Fully Hadronic Decay Channel at the LHC". Diplomarbeit, Universität Hamburg, Germany, 2010.

[82] M. Seidel, "Top-Quark Mass Measurement in Lepton+Jets final states, PHD thesis in preparation". Doktorarbeit, Universität Hamburg, Germany, 2014/2015.

[83] R. Brun and F. Rademakers, "ROOT: An object oriented data analysis framework", *Nucl.Instrum.Meth.* **A389** (1997) 81–86. doi:10.1016/S0168-9002(97)00048-X.

[84] "TTree". http://root.cern.ch/root/html/TTree.html.

[85] M. Seidel, "Measurement of Top Quark Mass and Jet Energy Scale at the CMS Experiment using the Ideogram Method". Diplomarbeit, Universität Hamburg, Germany, 2011.

[86] CMS Collaboration, "Measurement of the top-quark mass in $t\bar{t}$ events with lepton+jets final states in pp collisions at $\sqrt{s} = 7$ TeV", *JHEP* **1212** (2012) 105, arXiv:1209.2319. doi:10.1007/JHEP12(2012)105.

[87] B. Dutta, T. Kamon, N. Kolev et al., "Bi-Event Subtraction Technique at Hadron Colliders", *Phys.Lett.* **B703** (2011) 475–478, arXiv:1104.2508. doi:10.1016/j.physletb.2011.08.029.

[88] ATLAS Collaboration, "Determination of the Top Quark Mass with a Template Method in the All Hadronic Decay Channel using 2.04/fb of ATLAS Data", ATLAS Conference Note 2012-030, CERN, Geneva, (March, 2012).

[89] CMS Collaboration, "edm::VectorInputSource". https://cmssdt.cern.ch/SDT/doxygen/CMSSW_5_3_14/doc/html/de/db1/classedm_1_1VectorInputSource.html.

[90] CMS Collaboration, "edm::Event". https://cmssdt.cern.ch/SDT/doxygen/CMSSW_5_3_14/doc/html/d9/db1/classedm_1_1Event.html.

[91] CMS Collaboration, "edm::EmptySource". https://cmssdt.cern.ch/SDT/doxygen/CMSSW_5_3_14/doc/html/da/ddd/classedm_1_1EmptySource.html.

[92] M. Görner, "Differential Cross Sections for Top-Quark-Pair Production in the e/μ+Jets Final State at $\sqrt{s} = 8\,\text{TeV}$ in CMS". Doktorarbeit, Universität Hamburg, Germany, 2014.

[93] CMS Collaboration, "Measurement of differential top-quark pair production cross sections in pp colisions at $\sqrt{s} = 7$ TeV", *Eur. Phys. J. C* **73** (2013) 2339, arXiv:1211.2220. doi:10.1140/epjc/s10052-013-2339-4.

[94] CMS Collaboration, "Measurement of differential top-quark pair production cross sections in the lepton+jets channel in pp collisions at 8 TeV", CMS Physics Analysis Summary CMS-PAS-TOP-12-027, CERN, Geneva, (2013).

[95] CMS Collaboration, "Measurement of the differential ttbar cross section in the dilepton channel at 8 TeV", CMS Physics Analysis Summary CMS-PAS-TOP-12-028, CERN, Geneva, (2013).

[96] N. Kidonakis, "NNLL threshold resummation for top-pair and single-top production", arXiv:1210.7813.

[97] "TTreeFormula". http://root.cern.ch/root/html/TTreeFormula.html.

[98] "ROOT::Math::Minimizer". http://root.cern.ch/root/html/ROOT__Math__Minimizer.html.

[99] CMS Collaboration, "Estimating Systematic Errors Due to Pileup Modeling". https://twiki.cern.ch/twiki/bin/viewauth/CMS/PileupSystematicErrors. [Online, accessed 8 July 2014, CMS internal].

[100] ALEPH Collaboration, "Study of the fragmentation of b quarks into B mesons at the Z peak", *Phys. Lett. B* **512** (2001) 30–48, arXiv:hep-ex/0106051. doi:10.1016/S0370-2693(01)00690-6.

[101] DELPHI Collaboration, "A study of the b-quark fragmentation function with the DELPHI detector at LEP I and an averaged distribution obtained at the Z Pole", *Eur. Phys. J. C* **71** (2011) 1557, arXiv:1102.4748. doi:10.1140/epjc/s10052-011-1557-x.

[102] M. Botje, J. Butterworth, A. Cooper-Sarkar et al., "The PDF4LHC Working Group Interim Recommendations", arXiv:1101.0538.

[103] H.-L. Lai, M. Guzzi, J. Huston et al., "New parton distributions for collider physics", *Phys. Rev. D* **82** (2010) 074024, arXiv:1007.2241. doi:10.1103/PhysRevD.82.074024.

[104] A. Martin, W. Stirling, R. Thorne et al., "Parton distributions for the LHC", *Eur. Phys. J. C* **63** (2009) 189–285, arXiv:0901.0002. doi:10.1140/epjc/s10052-009-1072-5.

[105] R. D. Ball, V. Bertone, S. Carrazza et al., "Parton distributions with LHC data", *Nucl. Phys. B* **867** (2013) 244–289, arXiv:1207.1303. doi:10.1016/j.nuclphysb.2012.10.003.

[106] P. Z. Skands, "Tuning Monte Carlo Generators: The Perugia Tunes", *Phys.Rev.* **D82** (2010) 074018, arXiv:1005.3457. doi:10.1103/PhysRevD.82.074018.

[107] P. Z. Skands and D. Wicke, "Non-perturbative QCD effects and the top mass at the Tevatron", *Eur. Phys. J. C* **52** (2007) 133, arXiv:hep-ph/0703081. doi:10.1140/epjc/s10052-007-0352-1.

[108] CMS Collaboration, "Measurement of the top-quark mass in $t\bar{t}$ events with all-jets final states in pp collisions at $\sqrt{s} = 8$ TeV", CMS Physics Analysis Summary CMS-PAS-TOP-14-002, CERN, Geneva, (July, 2014).

[109] R. Wallny, "CMS Measurements of the top quark mass".

[110] CMS Collaboration, "Measurement of the top-quark mass in all-jets $t\bar{t}$ events in pp collisions at $\sqrt{s} = 7$ TeV", *Eur. Phys. J. C* **74** (2014) 2758, arXiv:1307.4617v2. doi:10.1140/epjc/s10052-014-2758-x.

[111] E. Schlieckau, "Measurement of the top-quark mass with all-jets final states in pp collisions at 7 TeV", *J.Phys.Conf.Ser.* **452** (2013) 012022. doi:10.1088/1742-6596/452/1/012022.

[112] CMS Collaboration, "Measurement of the $t\bar{t}$ production cross section in the all-jet final state in pp collisions at $\sqrt{s} = 7$ TeV", *JHEP* **1305** (2013) 065, arXiv:1302.0508. doi:10.1007/JHEP05(2013)065.

[113] Private communication with Roman Kogler for the Gfitter group.

[114] B. Stieger, "Trigger (Report from TSG workshop)". https://indico.cern.ch/event/312433/. [Online, accessed 8 July 2014, CMS internal].

Acknowledgements

First of all, I want to thank my parents for their support during my whole life. I always was encouraged to work on a topic that I enjoy and that is what I found in physics. Thanks for your overwhelming and never-ending support under all circumstances.

I am specially grateful to Prof. Peter Schleper for providing me the opportunity to do this interesting and exciting research, for the friendly supervision, the endless amount of new ideas, and the inspiring enthusiasm. Additionally, I want to thank Dr. Andreas Meyer and Jun.-Prof. Christian Sander for acting as referees together with Prof. Peter Schleper for my Dissertation and Disputation.

A special thank goes to Hartmut for his pragmatic solutions to many problems, the time for endless discussions (on- and off-topic), and the friendly, open, and direct collaboration.

I am very happy for having shared my office with Martin. We had an extremely funny and productive time of collaborative work and nothing could darken our bright mood! Also thanks to the whole working group, all of you, the long-term members, as well as, all the new faces and the alumni, made the working time here fun and help me a lot. Especially, I have to name Markus, Holger, Henning, Roger, Martijn, Thomas, Sebastian, and Jörn.

All of this work would not have been possible without the support, the discussions, the games, the sports, or to summarise this in one word the fun from and with my dearest friends. Thanks to all the uFs: Yasar, Julia, Andrey, Flo, Fanzi, Jonas, Almut, Nadja, Markus, Max, Aila, Vici, and again Martin!